EUROPEAN COMMISSION

Community Research

MATISSE

Materials' Innovations for Safe and Sustainable nuclear in Europe

Support to the development of joint research actions between national programmes on advanced nuclear materials

FP7-Fission-2013
Combination of Collaborative project (CP) and Coordination and Support Actions (CSA)

Grant agreement no: 604862
Start date: 01/11/2013 Duration: 48 Months

D.4.13

Effect of thermal ageing treatments and ion irradiation on the microstructure and mechanical behaviour of ODS steel bars and plates

MatISSE – Contract Number: 604862

Document title	Effect of thermal ageing treatments and ion irradiation on the microstructure and mechanical behaviour of ODS steel bars and plates
Author(s)	F. Bergner (responsible author), J. Aktaa, E. Altstadt, A. Chauhan, R. Coppola, Y. de Carlan, B. Duan, A. Etienne, C. Heintze, M. Hernández-Mayoral, J. Hoffmann, M. Houska, D. Litvinov, E. Oñorbe, D. Plaza, B. Radiguet, M. Serrano, A. Ulbricht
Number of pages	80
Document type	Deliverable
Work Package	4
Document number	D4.13
Issued by	HZDR
Date of completion	18/12/2017
Dissemination level	Confidential, only for consortium members (including the Commission Services)

Summary

A comprehensive and consistent description of the microstructures and mechanical properties of the ODS Fe9Cr and Fe14Cr alloys selected for the purposes of Task 4.1 of the MatISSE project was achieved by applying a combination of microstructure characterization techniques and mechanical testing. The collaborative study covered the assessment of the initial microstructures and properties of the ODS alloys as well as the effects of different kinds of thermal treatments and ion irradiations. The microstructure-based prediction of the room temperature yield stress is discussed. Supplementary results obtained within Task 4.1 on the high-temperature low cycle fatigue (LCF) behavior of a tempered martensitic 9Cr-ODS steel bar and on mechanical properties derived from small punch tests are presented in Annexes.

Approval

Rev.	Date	First author	WP leader	Project Coordinator
0	Dec. 2017	F. Bergner, HZDR	M. Serrano, CIEMAT	P.F. Giroux, CEA

Distribution list

Name	Organisation	Comments
All beneficiaries	MatISSE	

Table of contents

1 Introduction

This deliverable D4.13 is related to the task 4.1 “Role of the microstructure on the mechanical behavior of ODS alloys for LFR and SFR cladding“ of the project MatISSE. The objectives of task 4.1 according to the description of work are to characterize the ODS steels microstructure and its evolution after thermal treatments or ion irradiation and to have a better understanding on the deformation behaviour and anisotropy of ODS alloys. The results on the temperature-dependent deformation mechanisms were already exhaustively reported in deliverable D4.12. Moreover, the detailed work plan and testing matrices relevant for the present deliverable were provided in deliverable D4.11 released in the beginning of the project.

Before major issues related to the application of ODS steels and new insight gained within task 4.1 will be addressed below, it is useful to recall a number of basic features of the Fe-Cr system and ODS steels. Starting point is the binary Fe-Cr equilibrium phase diagram [1]. The γ-loop, γ being the fcc phase of Fe, extends to a Cr content of 11.9 at%. That means that Cr steels containing 9% Cr are transformable steels and their microstructure may be ferritic or martensitic depending on the cooling rate from austenitization temperature. Instead, Cr steels containing 14% Cr are always ferritic. In the present context, the delivered ODS Fe9Cr alloy was ferritic. The contributing laboratories performed own heat treatments based on austenitization and sufficiently high cooling rates to obtain martensitic microstructures more representative of cladding tubes. Another basic feature of the binary Fe-Cr system is the wide miscibility gap at and below operation-relevant temperatures. An approximation of the latest low-temperature part of the phase diagram is shown in Figure 1.1.

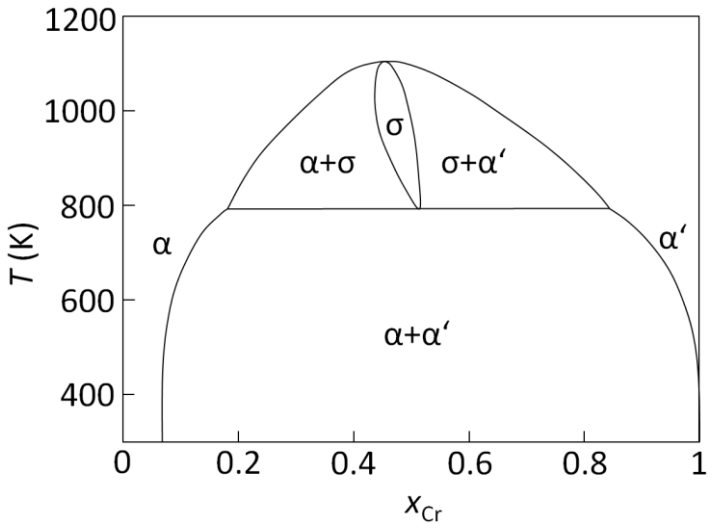

Figure 1.1: Low-temperature part of the equilibrium Fe-Cr binary phase diagram [1].

While Cr is in solution after typical heat treatments in the production stage of ODS steels, irradiation or long-term thermal treatments below 500 °C may give rise to hardening and embrittlement (475 °C embrittlement) due to the formation and evolution of α’ phase particles. These issues had to be addressed in task 4.1 and results are reported below.

Oxide-dispersion strengthening of Fe-Cr alloys and steels plays a triple role. Indeed, ODS nanoparticles:

- strengthen the material,
- contribute to a high density of sinks/traps for irradiation-induced point defects or He atoms,
- give rise to grain refinement (which also contributes to both the initial hardness and the sink strength).

A number of questions of cross-cutting scientific interest can be derived from the basic features of ODS Cr steels introduced above. The issues/questions addressed in the present deliverable are summarized in Table 1.1. This table also serves as a roadmap for reading the deliverable.

Table 1.1: Summary of issues/questions addressed in the deliverable.

Issue / question	Sections
Description of the microstructure of the as-received (ferritic) or quenched and tempered ODS steels based on the application of complementary micro- and nanostructural characterization methods	5, 8.1
Microstructure-property relationships for the ODS alloys in terms of yield stress	8.2
Microstructure stability for ODS alloys exposed to different kinds of thermal treatments including low-temperature short-term, medium-temperature long-term, and high-temperature short-term	6, 8.3
Effect of the initial microstructure in terms of sink strength on ion-irradiation-induced hardening and identification of irradiation-induced nanofeatures	7, 8.4
Microstructure evolution of ODS Fe9Cr exposed to high-temperature low-cycle fatigue (HT-LCF)	10.1

2 Materials

As part of the European 7th framework program project MatISSE, two oxide dispersion strengthened (ODS) alloys, namely a Fe-9%Cr-based transformable alloy and a Fe-14%Cr-based ferritic alloy, both in the product form of extruded bar, were distributed among partners in order to undergo a comprehensive and coordinated microstructural and mechanical examination. These ODS alloys were developed and produced under the supervision of CEA, France. The materials are introduced in the following subsections.

2.1 ODS Fe9Cr steel

The pre-alloyed powder was produced by Aubert & Duval, France, by gas atomization. Mechanical alloying of the pre-alloyed powder with Y_2O_3 particles was performed at Plansee, Austria, under hydrogen atmosphere using a vertical attritor ball mill. The milled powder was then sealed in soft steel cans followed by degassing and subsequently hot extruded into bars. The extrusion temperature for the ODS Fe9Cr bar was 1100°C.

The transformable ODS Fe9Cr steel extruded bar of diameter 20 mm (SRMA code L22-M1) was distributed among the partners in the ferritic state. The distribution scheme is shown in Deliverable D4.11 of MaTISSE. Heat treatments aimed to mimic the tempered martensitic (TM) microstructure of tube material were performed in the responsibility of the partners. The details of the heat treatments performed at HZDR and KIT are shown in Table 2.1. The composition of the studied ODS Fe9Cr steel extruded bar is shown in Table 2.2.

Table 2.1: Heat treatments performed on ODS Fe9Cr steel for specific techniques.

Heat treatment	1	2
Sample size	Cylindrical (d = 20.5 mm; l = 60 mm)	Cylindrical (d = 4.2 mm; l = 30 mm)
Heat treatments:		
Austenizing	At 1050 °C for 30 min	At 1050 °C for 10 min
Quenching	In oil at cooling rate of >20 K/s in the core of the sample	With He gas, cooling rate of 6–7 K/s
Tempering	At 750 °C for 1 h, air cooling	At 750 °C for 20 min, air cooling
Techniques	SANS	TEM/ EBSD/ Mechanical testing

Table 2.2: Composition (in mass %) of the investigated ODS steels.

Material	Cr	W	Ti	Si	Mn	Ni	C	Y_2O_3	Fe
ODS Fe9Cr	9.1	1.1	0.3	0.3	0.3	0.2	0.1	0.25	Balance
ODS Fe14Cr	13.5	0.9	0.4	0.32	0.27	0.17	-	0.22	Balance

2.2 ODS Fe14Cr steel

The ferritic ODS Fe14Cr extruded bar of diameter 36 mm (SRMA code J27-M2) was produced in the same way as described above for the ODS Fe9Cr extruded bar. It was distributed among partners within the EU-FP7 project GETMAT and remaining pieces were distributed again to partners within MatISSE. The consolidation was carried out by hot extrusion at 1100ºC at CEFIVAL France. The extruded bars were

annealed at 1050 ºC for 1.5h. The composition of the studied ODS Fe14Cr steel extruded bar is also shown in Table 2.2.

2.3 Other investigated ODS materials

KIT additionally tested the ODS Fe13Cr alloys MAT-1 and MAT-2 (ODS Fe13Cr HIP/HE in-house produced by hot isostatic pressing (HIP) and hot extrusion (HE), respectively, see Sections 3.1.3. and 6.2.

3 Thermal ageing and ion irradiations

3.1 Thermal ageing treatments

Three sets of thermal ageing treatments aimed at different aspects of thermal stability of the micro-structure were foreseen according to the work plan. These are:

- low-temperature (400 – 600 °C) short-term (approximately 1000 h) treatments in order to study hardening caused by the thermal formation of Cr-rich α´-phase particles (CIEMAT),
- intermediate-temperature (650 – 800 °C) long-term (up to 20.000 h) treatments in order to investigate the possibility of softening under conditions relevant for operation conditions due to particle and/or grain coarsening (CIEMAT, EDF), and
- high-temperature (900 ºC, 1100 ºC) short-term (up to 2500 h) treatments in order to investigate microstructure stability under conditions more relevant for ODS steel fabrication/optimization and to provoke recrystallization (KIT).

3.1.1 Low-temperature short-term treatments

Low-temperature short-term treatments were performed for two ODS extruded bars:

- 9Cr ODS bar (SRMA code L22-M1) in the ferritic and martensitic state
- 14Cr ODS bar (SRMA code J27-M2)

Chemical composition and basic characterization is included in Section 2 of the present document and MATISSE Deliverable 4.11.

Heat treatments were conducted according to the following specification:

- TT1: 475 °C/1000 h in order to investigate hardening/embrittlement caused by the formation of α'-phase particles.

The treatments were performed in tubular furnaces in air.

The specimens were mechanised in the longitudinal (L) orientation (load is applied parallel to the extrusion direction) and in the transverse (T) orientation (load is applied perpendicular to the extrusion direction), see Figure 3.1.

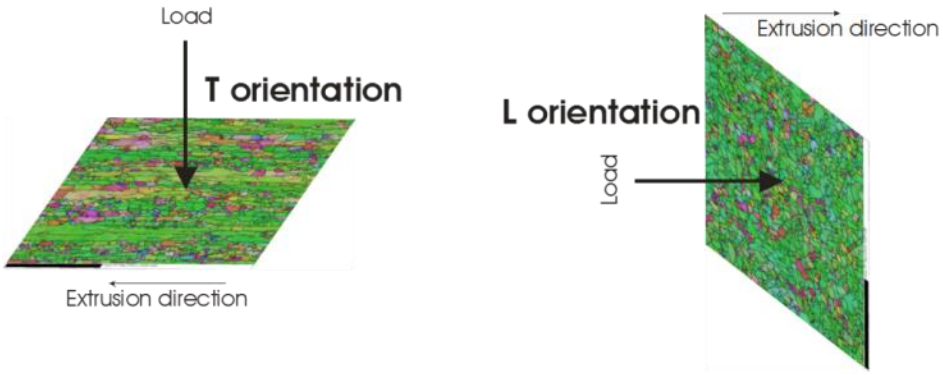

Figure 3.1: Orientation of the small punch specimens.

The overall test matrix also including intermediate-temperature long-term heat treatments is shown in Table 3.1.

Table 3.1: Overall test matrix including low-temperature short-term treatments and intermediate-temperature long-term treatments.

Material	Condition	L Orientation	T orientation
14 Cr ODS bar	As received	L1_RT, L2_RT L3_300, L4_300, L7_300, L8_300 L5_500, L6_500	T1_RT, T2_RT, T7_RT T8_RT T3_300, T4_300, T9_300, T10_300 T11_500, T12_500
	475ºC/1.000 h	L1_RT, L2_RT L3_300, L4_300 L5_500, L6_500	T1_RT, T2_RT T3_300, T4_300 T5_500, T6_500
	700ºC/10.000 h	L1_RT, L7_RT L3_300, L4_300 L5_500	T1_RT, T2_RT T3_300, T4_300 T5_500, T6_500
	800ºC/10.000 h	L1_RT, L2_RT L3_300, L4_300 L5_500, L6_500	T1_RT, T2_RT T3_300, T4_300 T5_500, T6_500
9 Cr ODS Bar	As received	L1_RT, L2_RT L3_300, L4_300 L5_500, L6_500	T1_RT, T2_RT T3_300, T4_300 T5_500, T6_500
	Tempered	L1_RT, L2_RT L3_300, L4_300 L5_500, L6_500	T1_RT, T2_RT T3_300, T4_300 T5_500, T6_500
	Tempered + 475ºC/1.000 h	L1_RT, L2_RT L3_300, L4_300 L5_500, L6_500	T1_RT, T2_RT T3_300, T4_300 T5_500, T6_500
	Tempered + 700ºC/10.000 h	L1_RT, L2_RT L3_300, L4_300 L5_500, L6_500	T1_RT, T2_RT T3_300, T4_300 T5_500, T6_500
	Tempered + 700ºC/10.000 h	L1_RT, L2_RT L3_300, L4_300 L5_500, L6_500	T1_RT, T2_RT T3_300, T4_300 T5_500, T6_500

3.1.2 Intermediate-temperature long-term treatments

Intermediate-temperature long-term heat treatments were conducted according to the following specification:

- TT2: 700ºC/10.000 h to asses thermal stability,
- TT3: 800ºC/10.000 h to asses thermal stability.

The treatments were performed in tubular furnaces in air. The specimens were mechanised in the longitudinal (L) orientation (load is applied parallel to the extrusion direction) and in the transverse (T) orientation (load is applied perpendicular to the extrusion direction), see Figure 3.1. The intermediate-temperature long-term heat treatments are included in Table 3.1.

3.1.3 High-temperature short-term treatments

The materials were cut into cubes and cylinders with a thickness of 10 mm, wrapped in stainless steel foil and vacuum-sealed in quartz glass tubes. These tubes were annealed at 900 °C or 1100 °C for times of 500, 2500 and 5000 h (only 900°C) in a conventional annealing furnace. An overview of the materials aged is given in Table 3.2. Figure 3.2 shows some of the samples before and after ageing at 1100 °C. We could only see minimal changes in the surface layer of the materials. We concluded that the vacuum conditions were good and prevented massive oxidation of the materials during the treatments. The materials after 900 °C ageing looked similar. In addition to the materials provided by the project partners, two other ODS materials produced in-house at KIT were also aged. The chemical composition and fabrication route of the selected materials are given in Table 3.2.

Table 3.2: Material fabrication details for the thermal ageing study performed at KIT.

Material	Cr	W	Ti	Y_2O_3	Fe	Compaction	TMT	Lab
MAT-1	13.1	1.13	0.151	0.217	bal.	Hot-isostatic-pressing 1100°C / 100 MPa	Rolling 1100°C	KIT
MAT-2	13.1	1.13	0.151	0.217	bal.	Hot extrusion 1100 °C	-	KIT
MAT-3	ODS Fe14Cr, see **Erreur ! Source du renvoi introuvable.**					Hot extrusion 1100 °C	annealed 1050 °C / 1.5 h	CEA
MAT-4	ODS Fe9Cr, see **Erreur ! Source du renvoi introuvable.**					Hot extrusion 1100 °C	as received	CEA

Figure 3.2: Samples before (left) and after 2500 h ageing (right) at 1100 °C.

3.2 Ion irradiations

The Fe-ion irradiations were performed at the 3 MV-Tandetron accelerator at the Ion Beam Center (IBC) at HZDR. A multi-step approach using different ion energies was applied to achieve an approximately rectangular dpa profile with an average displacement damage of 10 dpa over a depth of about 1.5 µm. The irradiation experiment was designed using the Kinchin-Pease option of the SRIM-2008.4 binary collision code assuming a displacement threshold of 40 eV. The irradiation parameters applied during the three steps are summarized in Table 3.3 in terms of energy and ion fluence. The calculated cross-section dpa profile of the three-step irradiation is shown in Figure 3.3. Figure 3.4 also shows the profile of the injected interstitial atoms. Irradiation experiments were performed at 300 ºC and 500 ºC. To this end, the samples were fixed on a heating target. The temperature was controlled by means of a thermocouple at the back of the samples. All samples exposed to the same irradiation condition were irradiated in the same irradiation experiment in order

to guarantee comparability. The ion beam was scanned over the whole surface to achieve a homogeneous irradiation. It is important to note that the samples were prepared prior to the irradiation experiment up to a surface quality required for nanoindentation and/or depth-resolved positron annihilation spectroscopy be performed.

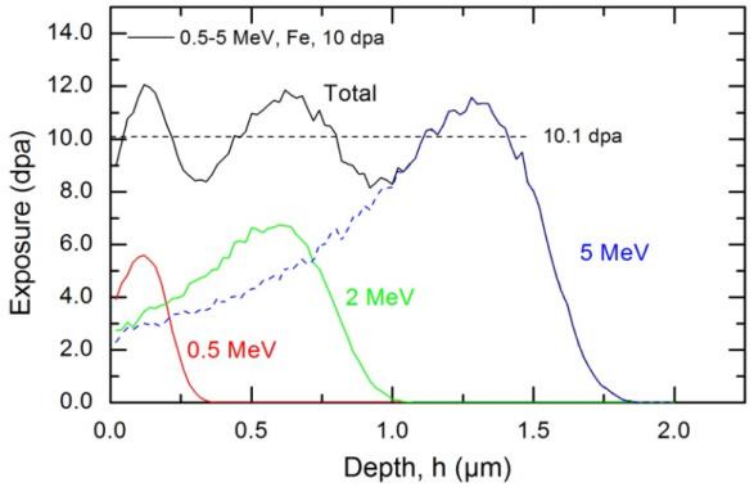

Figure 3.3: dpa distribution of the three-step irradiation calculated by SRIM.

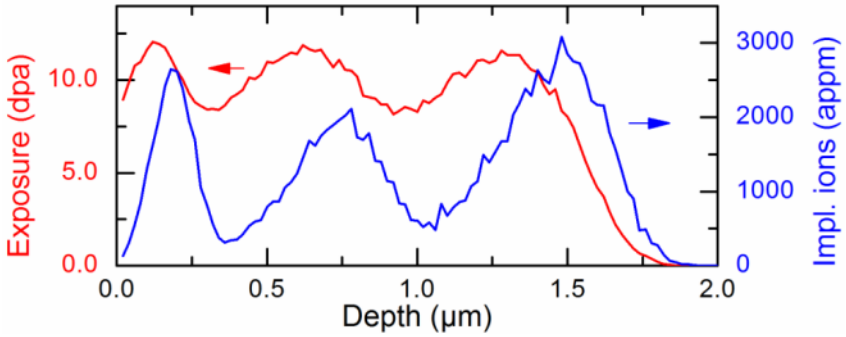

Figure 3.4: Depth profiles of the ion dose in dpa and the injected interstitials for the three-step irradiation calculated by SRIM.

Table 3.3: Parameters of the three-step irradiation.

Step	Ion	Energy (MeV)	Ion fluence (1/cm^2)
1	Fe^+	0.5	3.7 x 10^{15}
2	Fe^+	2	6.1 x 10^{15}
3	Fe^{2+}	5	1.15 x 10^{16}

4 Microstructural and mechanical characterization techniques

4.1 Electron backscatter diffraction (EBSD)

The EBSD measurements were performed on a Zeiss Merlin field-emission-gun scanning electron microscope equipped with a high-speed Hikari EBSD camera by EDAX. The EBSD data treatment was done using OIM Analysis 7.2 software. Apart from discarding points with a confidence index (CI) of less than 0.1 and subsequent CI neighbor correlation, no cleanups were performed. If grains are plotted into maps, a misorientation angle between 15° and 65° was considered a grain boundary. A valid grain consists of at least 50 measured points. These parameters were also used for the grain size distribution histograms. Edge grains not fully immersed in the maps were neglected for the statistics.

Different versions of EBSD were applied in the contributing labs for the purpose of specifying the type of microstructure (ferritic versus martensitic), the degree of anisotropy/texture and grain size. The EBSD patterns were acquired at KIT (Ankur) with a Zeiss EVO MA 10 scanning electron microscope (SEM) and at Helmholtz-Zentrum Dresden-Rossendorf (HZDR), Germany, with a Zeiss NVision 40 cross beam SEM both equipped with a Bruker e-Flash detector and analyzed with the QUANTAX ESPRIT software. Whereas, at CIEMAT a Hitachi SU6600 field emission gun (FEG) SEM equipped with an Oxford Instruments HKL NordlysF detector was used to obtain the EBSD patterns. The grain size distributions were measured with grain boundaries defined by a misorientation angle higher or equal to 5°. The meaning of the data will be specified in the results section.

4.2 Neutron diffraction texture measurement

Neutron diffraction provides a valuable technique allowing the non-destructive study of crystallo-graphic texture in massive samples. General information on texture determination by neutron diffraction can be found for instance in [2], [3]. The principle of the technique is the same as for X-rays, but the sampling volume can be as large as 1 cm^3. Once a set of 3 reference axes is defined (usually related to the thermo-mechanical history of the sample), the texture is quantified by the Orientation Distribution Function (ODF), that is the differential volume fraction of crystallites ex-hibiting a given orientation with respect to such axes. To obtain the ODF, a given Bragg reflection has to be selected and its stereographic projection, or pole figure, measured when the sample is rotated with respect to the 3 reference axes. Usually, at least two pole figures, corresponding to two different Bragg reflections, are needed to obtain the ODF of the investigated sample, following a mathematical procedure based on a series expansion method, as discussed in [4].

The neutron diffraction measurements were carried out in the responsibility of ENEA at the STRESS-SPEC instrument [5], installed at the FRM II reactor, in Garching, and operated by the Helmholtz-Zentrum Geesthacht. The measurements were carried out at room temperature. A Ge (311) monochromator was utilized, providing a neutron wavelength of 1.602 Å. The investigated diffracting volume was approximately 0.63 cm^3.

4.3 Transmission electron microscopy (TEM)

Different versions of TEM were applied in the contributing labs in order to characterize the microstructure of the as-received ferritic or tempered-martensitic microstructures. The TEM studies were performed at KIT using a FEI TECNAI-20F microscope, at CIEMAT and at CEA both using a JEOL JEM-2010 microscope; all operating at 200 keV.

Special TEM techniques were applied in order to identify and characterize irradiation-induced nanofeatures such as dislocation loops and other microstructural changes (including stability of oxide nanoparticles) induced by either thermal treatments or ion irradiations or cyclic loading.

4.4 Small-angle neutron scattering (SANS)

SANS experiments in the responsibility of HZDR were performed at the Instrument V4 at Helmholtz-Zentrum Berlin (HZB) [6] using a neutron wavelength of 0.605 nm. The samples of dimensions 9 x 9 x 1 or 10 x 10 x 1 (mm) were placed in a saturation magnetic field of 1.57 Tesla in order to separate magnetic and nuclear scattering. Two sample-detector distances of 1.7 m and 8 m were used. The software package BerSANS [7]

was used for corrections, absolute calibration, data reduction and separation of magnetic and nuclear scattering contributions. The transformation from scattering curves into particle-size distributions was performed using a Monte Carlo (MC) code [8] developed in house at HZDR.

4.5 Atom probe tomography (APT)

APT analysis was performed at GPM, Université de Rouen, using a Cameca LEAP 4000X HR. Samples for APT were prepared in 2 steps, using standard electro polishing methods (1st step in 90% acetic acid plus 10% perchloric acid, 2nd step in 2% perchloric acid and 98% ethylenglycol). Experiments were conducted with electric pulses (pulse fraction equal to 20%, pulse repetition rate equal to 200 kHz) and a specimen temperature between 40 and 50K. 3D reconstruction was done with the IVAS 3.6.10 software. The reconstruction parameters were adjusted to get the good interplanar distances. The detailed analyses of the reconstructed volumes were performed with the GPM3D software v.6.1. Y and Ti oxides were identified using the isoposition method (IPM) developed by Da Costa [9]. This method is based on concentration criteria. The ions used to set the concentration threshold were Y^{3+}, YO^{2+}, TiO^{2+}, CrO^{2+} and O^{+}. As it was shown in [10], the APT analysis of nano-particles in ODS steels is subjected to strong bias. To correct this bias, Fe and Cr were removed from particle compositions and the size reported is the longest axis of the particles and not the Guinier radius.

4.6 Nanoindentation testing

A Universal Nanomechanical Tester UNAT (ASMEC/Zwick) equipped with a Berkovich indenter was utilized to measure the hardness of the ion irradiated samples and the unirradiated references. Calibrations of the indenter geometry and the instrument stiffness were based on measurements on two reference materials (fused silica, sapphire) with known elastic modulus. Quasi continuous stiffness measurement (QCSM) was applied with the load superimposed with a sinusoidal oscillation for 3 s at discrete loads while the average load is kept constant. This way, the contact stiffness can be calculated at discrete points along the loading curve using the force and displacement amplitude and taking into account the mass and the damping of the measuring head. With this information, the full loading curve can be exploited to calculate the indentation hardness (HIT) as a function of contact depth (hc). The tests were performed with a maximum load of 50 mN with corresponding contact depth of about 650 to 750 nm. More than 30 indents per sample were performed. Zero point and thermal drift correction were applied to each individual curve. Thereafter, an average curve was calculated and analyzed using the Oliver-Pharr method. The hardness value at a reference depth of 200 nm was chosen as the hardness representative of the irradiated layer and to calculate the irradiation-induced hardness change. This takes into account that the deformed zone in alloy is usually 5-10 times deeper than the contact depth, i.e. at 200 nm contact depth, the full plastically deformed zone is within the irradiated layer.

4.7 Small-punch test (SPT)

Small punch tests consist on deform a small disc under contact displacement rate, while load, punch displacement and disc deflection is measured. The specimen holder with the dimensions used by CIEMAT are seen in Figure 4.1. Small punch tests has been performed by testing 3 mm diameter discs with 0.25 mm thickness, at a displacement rate of v=0.3 mm/min at room temperature, 300 ºC and 500 ºC. During the tests the punch displacement, disc deflection and load were measured.

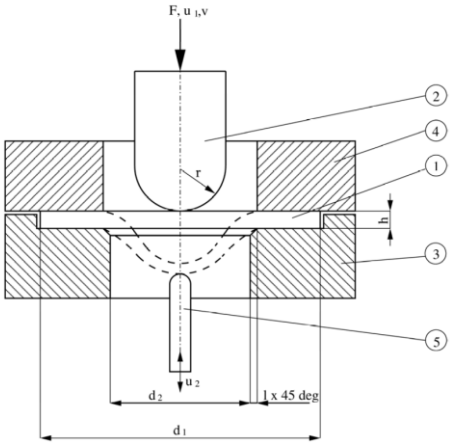

d_1 mm disc diameter = 3 mm
d_2 bore diameter of receiving die = 1.5 mm
r punch tip radius = 0.5 mm
h height of specimen = 0.25 mm
l length of receiving die edge chamfer=0.2 mm

1 – specimen
2 – punch
3 –receiving die
4 – clamping die
5 – deflection measurement rod

F (kN) punch force
u_1 (mm) displacement
u_2 (mm) deflection
v (m/s) punch velocity

Figure 4.1: Cross–sectional scheme of the testing apparatus according to standard CWA 15627:2006 (E) Part B: A Code of Practice for Small Punch Testing for Tensile and Fracture Behaviour.

The test result is a load.vs.deflection (displacement) curve as the one shows in Figure 4.2 a). The main parameters of the curve are:

- F_m [N] – maximum load recorded during SP test,
- F_e [N] – load characterizing the transition from linearity to the stage associated with the spread of the yield zone through the specimen thickness (plastic bending stage)
- d_m [mm] – displacement corresponding to maximum load F_m,
- E^{SP} [J] – SP fracture energy obtained from the area under the load punch displacement curve up to maximum load.

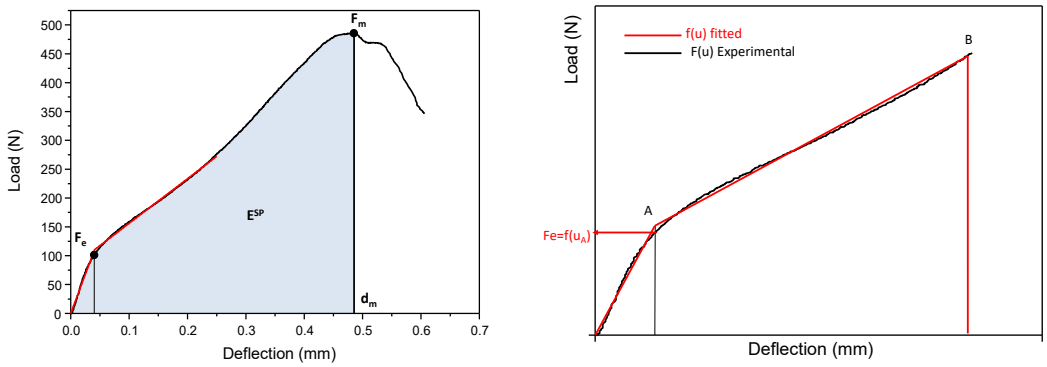

(a) (b)

Figure 4.2: a) Load-deflection curve with characteristic parameters and b) calculation of F_e according to standard CWA 15627:2006 (E) Part B: A Code of Practice for Small Punch Testing for Tensile and Fracture Behaviour.

Calculation of F_e is performed following the recommendations of CWA 15627: a bilinear function f(u) from the origin through the points A and B is defined as:

$$f(u) = \begin{cases} \dfrac{f_A}{u_A} u & for \;\; 0 \le u < u_A \\ \dfrac{f_B - f_A}{u_B - u_A}(u - u_A) + f_A & for \;\; u_A \le u < u_B \end{cases}$$

$$err = \int_0^{u_B} [F(u) - f(u)]^2 du$$

by varying f_A, u_A and f_B the error is minimized and leads to final values for the varied variables and therefore to a best fit of the function f(u) to the measured load punch displacement curve F(u). Then, the yield displacement $u_e = u_A$ and the load F_e can be obtained from the experimental load punch displacement curve as $F_e = F(u_A)$. The parameter u_B is chosen as 0.250, equal to the disc thickness.

4.8 Tensile test

Tensile tests on ODS Fe9Cr steel were performed using an Instron 4505 universal testing machine equipped with an extensometer. Regarding ODS Fe14Cr steel, the tests were performed on a servo hydraulic MTS testing machine. Owing to the material quantity limitations, small tensile test specimens were used. With respect to ODS Fe9Cr steel, specimens with a gauge length of 13 mm and a gauge diameter of 2 mm were used. In the case of ODS Fe14Cr steel, specimens with a dog-bone geometry and a gauge section of $15 \times 3 \times 2$ mm^3 were used. All specimens were machined parallel to the extrusion direction. For ODS Fe9Cr steel, tests were carried out under force control with a nominal strain rate of 10-3 s-1 and for ODS Fe14Cr steel, tests were performed under stroke control at a displacement rate equal to 0.1 mm/min (corresponding to a strain rate of 10^{-4} s^{-1}).

5 Results on as-received and quenched & tempered materials

The results presented in this section have partly been published by the contributing project partners in Ref. [11].

5.1 TEM investigations

TEM bright field micrographs of ODS Fe9Cr extruded bar in both as-received as well as heat-treated conditions are shown in Figure 5.1. In as-received state (Figure 5.1a), the steel exhibits equiaxed grains with a dislocation density $(0.46 \pm 0.1) \times 10^{14}$ m^{-2}. The dark contrast Cr carbides are present both at grain boundaries and within the grains.

Upon heat treatment (Figure 5.1b), the steel manifests tempered martensitic structure with laths and subgrains having high dislocation density ($3.4 \pm 1.0 \times 10^{14}$ m^{-2}). The typical laths were several µm in length and (0.25 ± 0.01) µm in width. Additionally, irregular shaped Cr-W enriched carbides and Ti-enriched particles are distributed at various boundaries. For more details see Ref. [12].

In both states, complex Y–Ti–O nanoparticles are inhomogeneously distributed within the matrix. Nevertheless, regions with homogeneous particle distribution were also observed, for example see Figure 5.2a. The density of the nanoparticles has been estimated using such micrographs, where the nano-oxides density was homogeneous. From these TEM investigations, it can be concluded that the heat treatment did not change the size and distribution of the nanoparticles. High resolution TEM (HRTEM) investigations reveal face centered cubic $Y_2Ti_2O_7$ crystal structure for the examined particles. One such particle lattice (encircled) along with its corresponding fast Fourier transform power spectrum diffraction pattern from heat-treated ODS Fe9Cr steel is shown in Figure 5.2b.

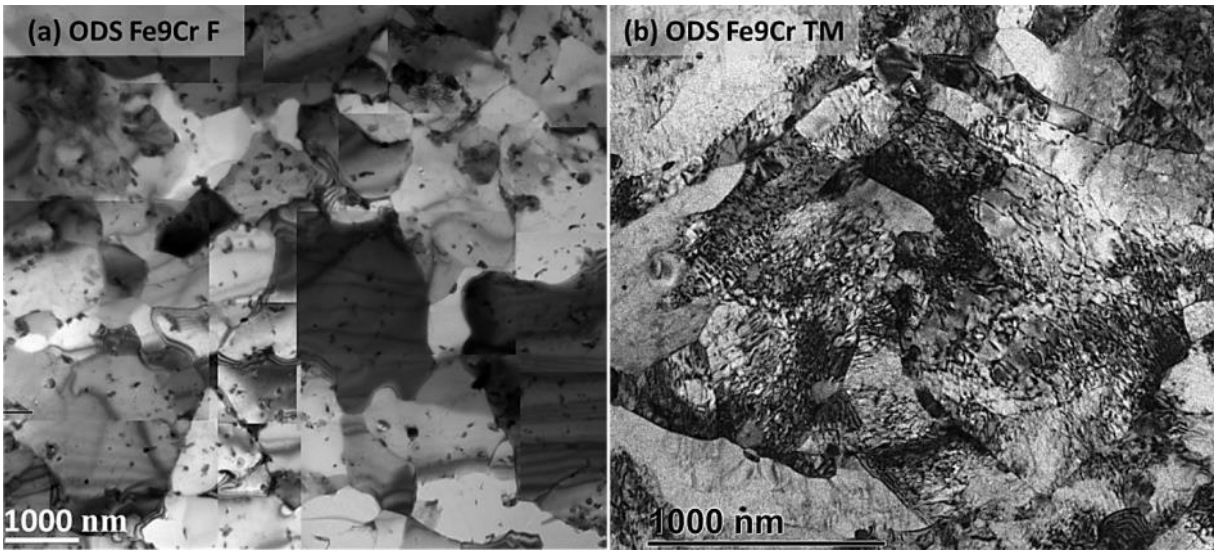

Figure 5.1: TEM bright field micrographs revealing ODS Fe9Cr steel in (a) as-received state (ferritic) having dark contrast Cr carbides with low dislocation density (the collage was formed using 16 separate micrographs) and (b) heat-treated state (quenched and tempered) having tempered martensitic structure with high dislocation density.

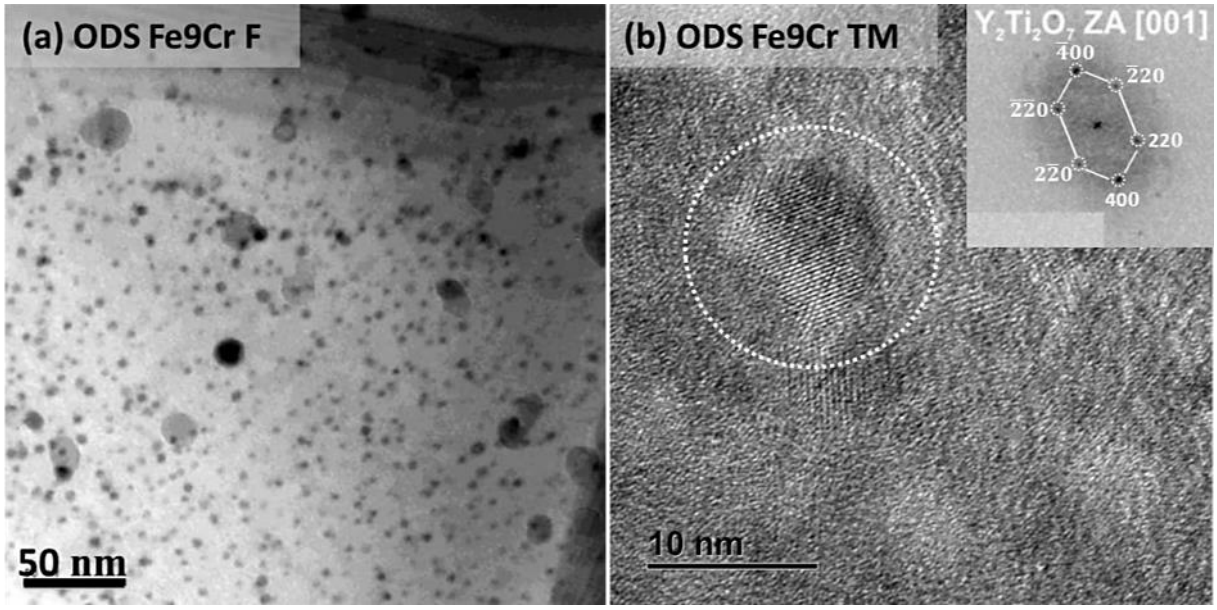

Figure 5.2: (a) TEM bright filed micrograph from as-received ODS Fe9Cr steel revealing region with homogenous particle distribution. (b) High resolution TEM micrograph from heat-treated ODS Fe9Cr steel shows an $Y_2Ti_2O_7$ particle lattice (encircled) with [001] zone axis having face centered cubic crystal structure and its corresponding fast Fourier transformation (FFT) power spectrum diffraction pattern in inset.

TEM bright field micrographs from as-received ODS Fe14Cr extruded bar are shown in Figure 5.3. In longitudinal direction (Figure 5.3a), the grain structure appears to be composed of large elongated grains, together with regions of small equiaxed grains. In transverse direction (Figure 5.3b), the grains are smaller and they do not exhibit elongated shape. Regarding dislocation structure, regions with different dislocation density are present. The average dislocation density is estimated to be about 5×10^{14} m^{-2}. The observed strengthening nanoparticles are inhomogeneously distributed and they can be found forming lines, sometimes parallel to grain boundaries, as well as channels free of particles. The size distribution of particles can be classified in two ranges, smaller than 20 nm and larger than 20 nm, with regions where one or the other predominates (Figure 5.4). The nanoparticles also show different morphologies, square or round, different composition and stoichiometry, implying different crystallography and interfacial structure. Careful examination of these particles, as reported separately (see Ref. [13]), reveals some of them enriched with Cr, Ti, Y, and W which decorate grain boundaries. Nevertheless, majority is of the Y-Ti-O nanoparticles which are observed within the grains along with the Al-rich and Ti-rich particles. For more details on TEM studies, we refer to Refs. [13,14].

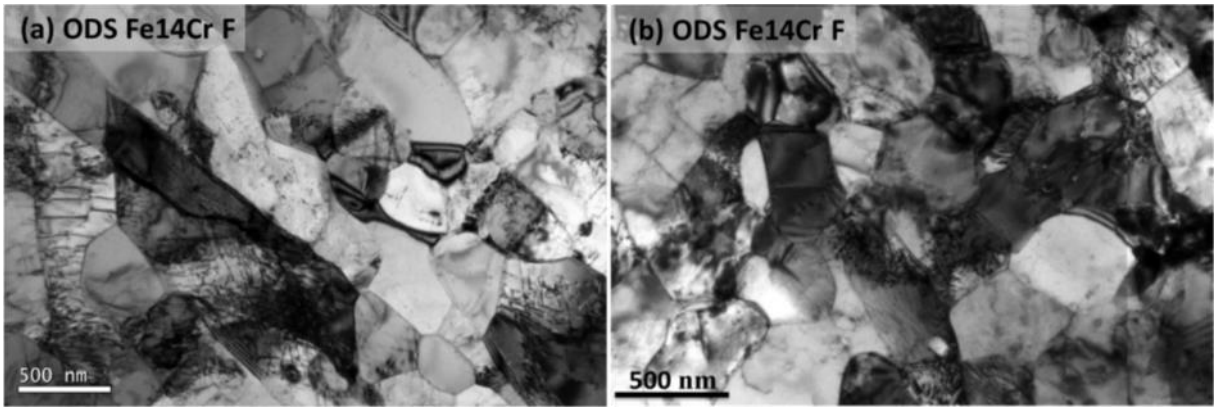

Figure 5.3: TEM bright field micrographs from as-received ODS Fe14Cr steel (ferritic). (a) Longitudinal direction revealing elongated as well as equiaxed grains. (b) Transverse direction revealing small equiaxed grains. In both directions, regions with different dislocation density are apparent.

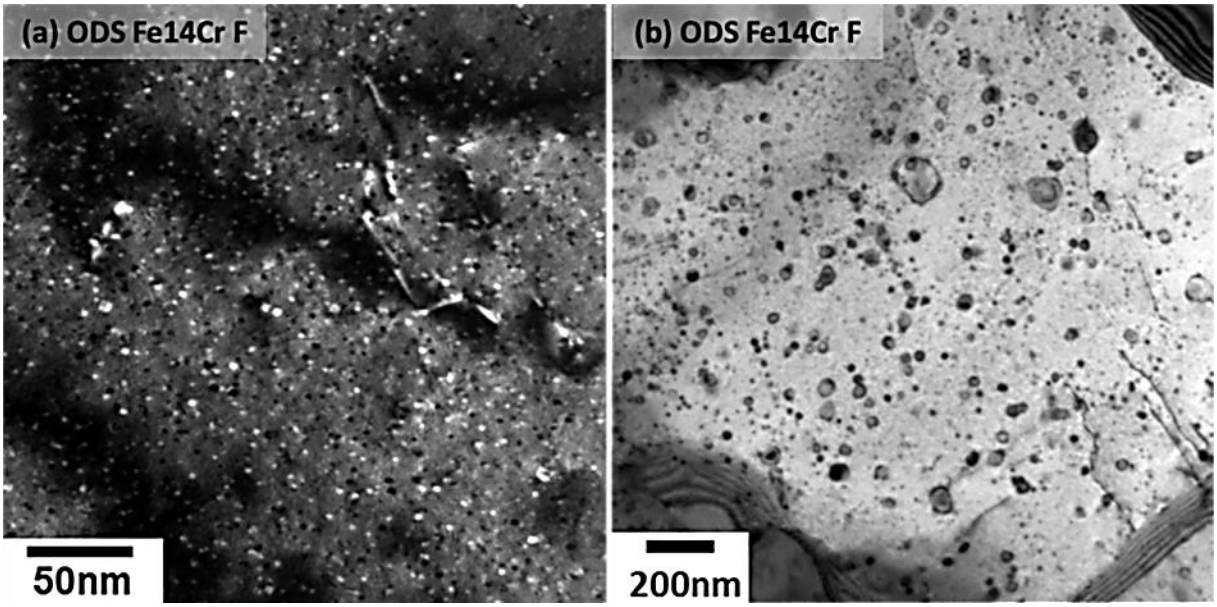

Figure 5.4: TEM micrographs revealing nanoparticles distribution in ODS Fe14Cr steel. (a) Dark field shows particles smaller than 20 nm and (b) bright field unveils particles larger than 20 nm [13].

5.2 EBSD investigations

Typical inverse pole figure (IPF) maps obtained by EBSD for the as-received as well as heat-treated ODS Fe9Cr steel are shown in Figure 5.5. The dissimilar colors of the grains in the IPF maps reveal the large difference in the orientation of the neighbor grains. Moreover, no texture was identified in the stereographic projections (not shown here). In both states, high- and low-angle grain boundaries are present. The misorientation analysis revealed that the fractions of high-angle grain boundaries (HAGB, >15°) and low-angle grain boundaries (LAGB, 2-15°) in as-received state are 97% and 3%, respectively; whereas, in heat-treated state are 78% and 22%, respectively. The average grain sizes measured via EBSD for as-received and heat-treated states are (1.19 ± 0.03) µm and (0.46 ± 0.02) µm, respectively.

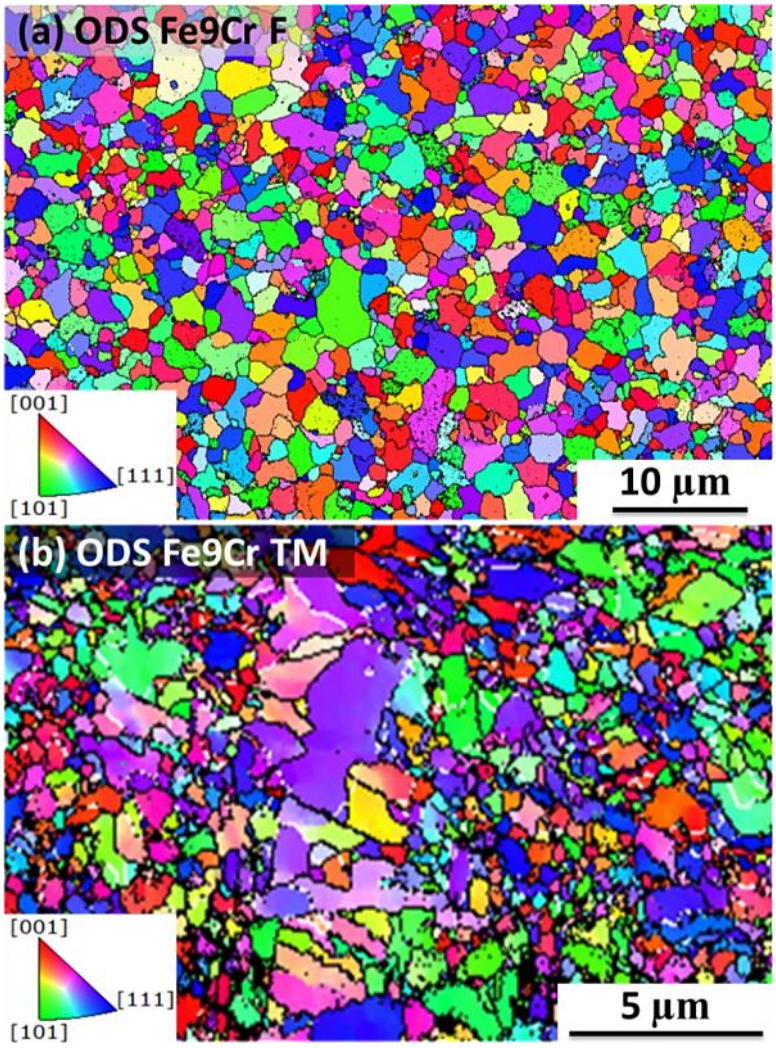

Figure 5.5: Inverse pole figure maps obtained via EBSD for (a) as-received (step size: 72 nm) and (b) heat-treated (step size: 68 nm) ODS Fe9Cr steel (color keys for the crystallographic orientation are also shown); high-angle grain boundaries (HAGB, >15°) are marked by black lines while low-angle grain boundaries (LAGB, 2–15°) are marked by white lines.

EBSD studies on as-received ODS Fe14Cr steel have been reported several times, see Refs. [13–15]. Briefly, the steel in longitudinal direction manifests bimodal grain size distribution, in which the smallest grains have distribution ranging from 0.1 to 3.0 µm, representing a volume fraction of 80%, whereas the largest and more elongated grains have sizes between 3.0 and 9.0 µm with a volume fraction of 20%. On the contrary, in the transverse plane, a more uniform distribution of grain size is observed, with a mean grain size of (0.46 ± 0.04) µm. With respect to the texture, a preferential crystallographic orientation of the grains along <110> parallel to the extrusion direction is observed (for example see Fig. 6). The misorientation analysis revealed that the fractions of HAGB and LAGB are 89% and 11%, respectively. The mean grain sizes obtained by EBSD are summarized in Section 5.7.

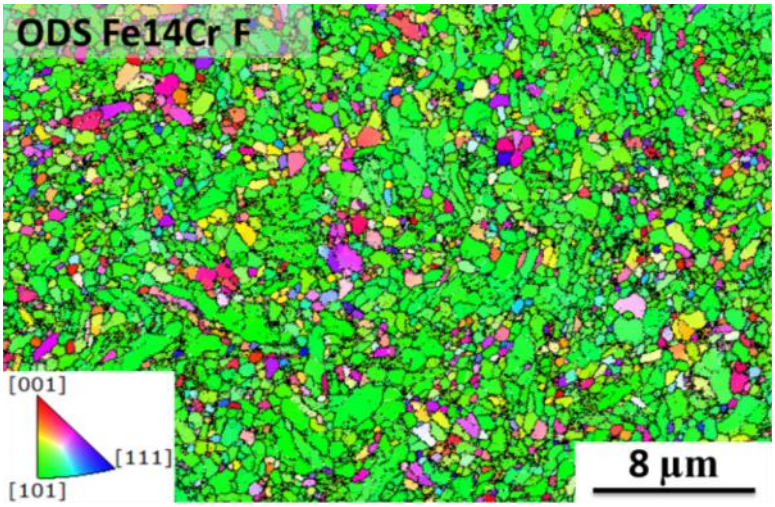

Figure 5.6: Inverse pole figure map obtained via EBSD for as-received ODS Fe14Cr steel (step size: 48 nm) in transverse direction (color key for the crystallographic orientation is also shown).

5.3 SANS investigations

The measured magnetic scattering curves for ODS Fe9Cr extruded bar in the as-received and heat-treated conditions are plotted in Figure 5.7a. The scattering curves for both conditions were found to agree in the Q-range from 0.3 to 3 nm-1, which governs the size distribution of ODS particles. It can be concluded that the austenitization and subsequent quenching did not change the size distribution of scatterers. The MC fit of the difference between cross sections measured for the as-received condition and the background consisting of an adjusted part proportional to Q-4 and a constant incoherent scattering part derived from the Porod plot is shown in Figure 5.7b.

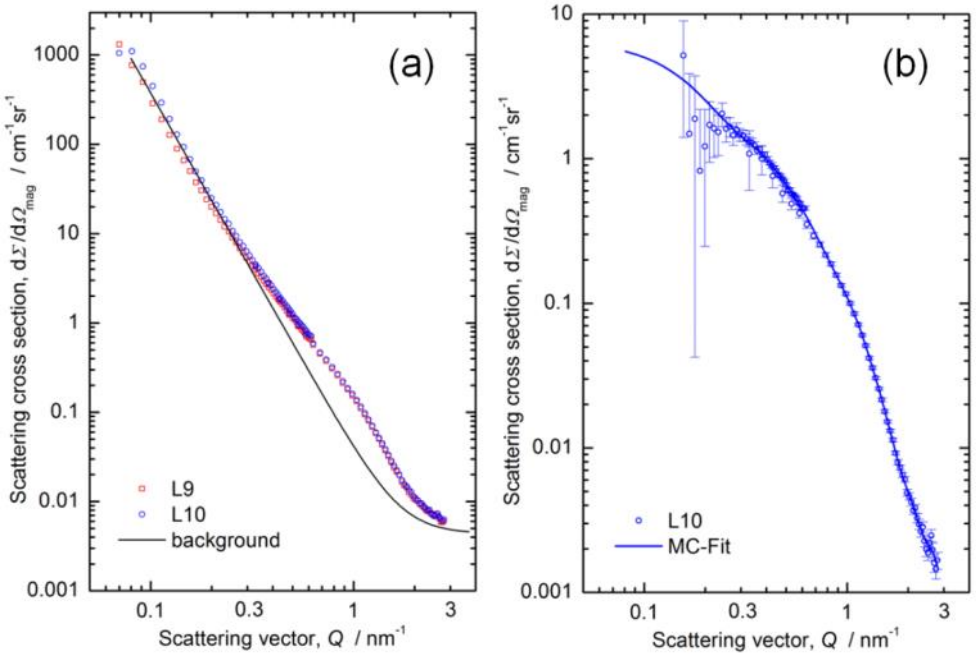

Figure 5.7: (a) Scattering curves measured for the as-received condition (L10) and the heat-treated condition (L9) of ODS Fe9Cr and background consisting of an adjusted part proportional to Q^{-4} and constant incoherent scattering derived from the Porod plot, (b) measured difference scattering curve for the as-received condition (L10) and MC fit.

The size distribution of oxide nanoparticles corresponding to the MC fit of the difference scattering curve for the as-received condition of ODS Fe9Cr extruded bar is shown in Figure 5.8a. Scaling in absolute units was achieved by assuming non-magnetic scatterers dispersed in the ferromagnetic matrix. The size distribution for the ODS Fe14Cr extruded bar (sample L12) plotted in Figure 5.8b was obtained according to the same procedure. The error ranges resulting from the MC fit are indicated as colored bands. It is interesting to note that the number density of nanoparticles in a yttria-free 14Cr reference (sample L11) is almost as high as the number density of nanoparticles in the ODS sample. This may be attributed to the formation of Cr- enriched oxide particles in the yttria-free sample due to the powder metallurgy fabrication steps under uncontrolled (or not perfectly controlled) oxygen partial pressures. The average A-ratios, A = 1 + M/N, where M and N are the magnetic and nuclear scattering contributions, respectively, are (2.5 ± 0.2) for ODS Fe9Cr, (2.3 ± 0.1) for yttria-free Fe14Cr and (3.25 ± 0.2) for ODS Fe14Cr. This indicates differences or similarities in the nanoparticle composition. For ODS Fe9Cr, the A-ratio is consistent with $Y_2Ti_2O_7$- and Y_2TiO_5-type particles [16]. For Fe14Cr, the A-ratio does not give a straightforward indication on the type of nanoparticles.

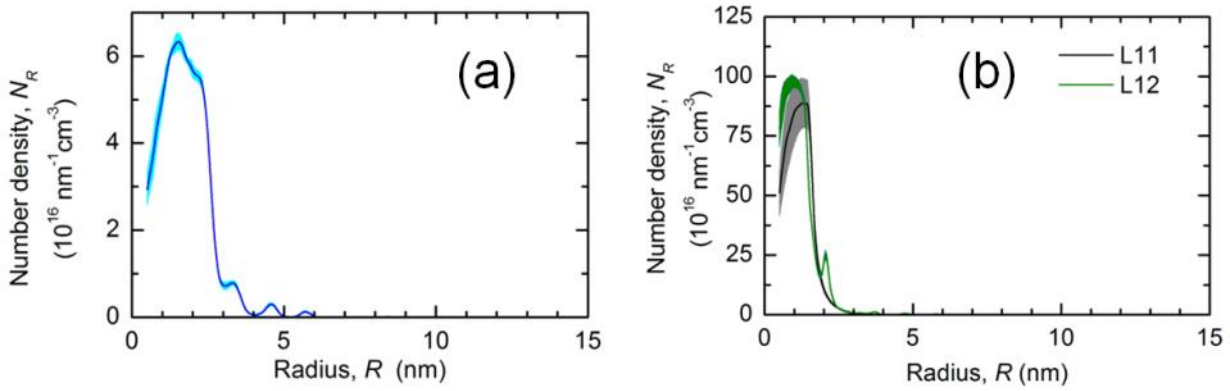

Figure 5.8: Size distribution in terms of particle number density per radius increment for (a) the as-received condition of ODS Fe9Cr (L10) and (b) the as-received condition of ODS Fe14Cr (L12) and the yttria-free 14Cr reference (L11).

5.4 APT investigations

Both ODS Fe9Cr and Fe14Cr extruded bars were characterized by APT. In each case, the global chemical composition and the characteristics of the nano-oxides were measured.

5.4.1 ODS Fe9Cr (as-received) extruded bar

The average chemical composition of the ODS Fe9Cr measured by APT is reported in Table 5.1 (including all features intercepted during APT analysis). The average composition is calculated from 3 APT dataset. Minimum and maximum concentrations of solutes from the different data set are also reported to give an estimation of the dispersion of the results. It appears that the distribution of elements from one volume to another is relatively homogeneous. A high concentration of C is measured in one of the volumes because a carbide enriched in Cr, W and Mn is partly intercepted. In comparison with the nominal (bulk) composition, the concentrations of Si, Mn, Ni, Cr and W are in good agreement with the expected ones. The levels of C, Ti, Y and O are very low compared to nominal ones, suggesting the presence of carbides and oxides with low number density (so not intercepted by APT analysis). Unexpectedly, low concentrations of Mo (~0.2 at.%) and traces of P, N, Al, V and Co (below 0.01%) are measured.

Table 5.1: APT (minimum, maximum and average values) and bulk (chemical analysis) compositions of ODS Fe-9%Cr (at%, balance Fe). In addition to elements reported in the table, traces (< 0.01%) of N, Co, P, Al and V were also detected.

	C	Si	Mn	Ni	O	Cr	Y	Ti	W	Mo
APT minimum	0.011	0.58	0.25	0.22	0.039	7.91	0.004	0.023	0.23	
APT maximum	0.46	0.59	0.28	0.23	0.067	9.90	0.010	0.032	0.31	
APT average	0.042	0.58	0.27	0.23	0.058	9.67	0.01	0.026	0.30	0.023
Bulk	0.46	0.59	0.30	0.19	0.18	9.74	0.12	0.35	0.33	-

Two examples of volumes analyzed by APT are shown on Figure 5.9. Small Y and Ti oxides are detected in all volumes. Their spatial distribution is heterogeneous. Indeed, the local number density varies from less than 0.2×10^{22} m^{-3} in particles free zones to about 6×10^{22} m^{-3}. On average the number density is $(2.7 \pm 0.5) \times 10^{22}$ m^{-3}. Such distribution could be explained by the interaction of migrating grain boundary (GB) and Y and Ti oxides during ODS elaboration [17]. Most of the observed particles are located in matrix and only two are located at GB. There average sizes are 5.1 and 5.6 nm respectively. In average, the particle size is about (5.1 ± 0.8) nm since a large majority is located in the matrix.

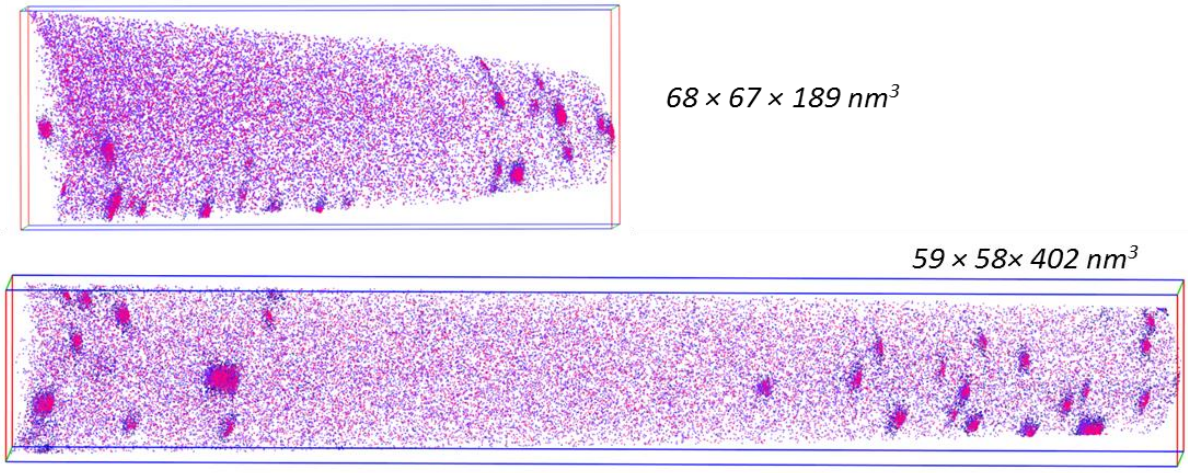

Figure 5.9: Two examples of 3D reconstructions of the ODS Fe9Cr extruded bar. Y is in red, TiO molecular ions are in purple and O is in blue.

As far as the chemical composition of oxides is concerned, a high level of Fe and Cr is detected inside the particle. However, the presence of these elements in particles is attributed to field evaporation artefacts. The chemical composition of the oxides located in the matrix (considering only Y, Ti and O) is (22.4 ± 0.9)%Y-(22.3 ± 0.9)%Ti-(55.3 ± 0.9)%O.

5.4.2 ODS Fe14Cr extruded bar

The average chemical composition of the ODS Fe14Cr calculated from 4 APT dataset is reported in Table 5.2. Minimum and maximum concentrations of each solute (depending of the dataset) are also reported. In comparison with the expected bulk composition, several impurities are detected (C, N, Co, P, Al, V), the level of Ni is too high and there is a lack of Y, Ti and O, suggesting the presence of a low number density of large oxides not intercepted by APT volumes. It also has to be noticed that the distribution of several solutes within the material is heterogeneous at a larger scale than typical APT volumes.

Table 5.2: APT (minimum, maximum and average values) and bulk (chemical analysis) compositions of ODS Fe-14%Cr (at%, balance is Fe). In addition to elements reported in the table, traces (~0.01%) of N, Co, P, Al and V were also detected.

	C	Si	Mn	Ni	O	Cr	Y	Ti	W
APT minimum	0.002	0.57	0.31	0.21	0.043	12.7	0.004	0.016	0.14
APT maximum	0.082	0.95	0.33	0.25	0.40	15.5	0.071	0.15	0.29
APT average	0.026	0.67	0.32	0.24	0.13	13.35	0.017	0.05	0.20
Bulk	-	0.63	0.29	0.16	0.22	14.90	0.15	0.45	0.33

In the case of Y, Ti and O these strong fluctuations can be explained by an heterogeneous distribution of nano-oxides in the material. Two examples of the observed microstructures are shown on the Figure 5.10. As it can be seen, nm-sized particles rich in Ti, Y and O are systematically observed. The largest ones are located at GB. In addition to largest Y and Ti oxides, the GBs are enriched in Cr. The average sizes of the particles located at GB and in the matrix are 3.7 and 2.5 nm respectively. The number density of particles at GB is about 4×10^{24} m^{-3}. In the matrix, the particle distribution is strongly heterogeneous. Some volumes are almost free of particles whereas some others contain a high number density (from 1.2 to 53×10^{22} m^{-3}). All in all, the average sizes and number density, considering particles at GB and inside grains, are (2.8 ± 1.5) nm and $(16.1 \pm 1.8) \times 10^{22}$ m^{-3}, respectively.

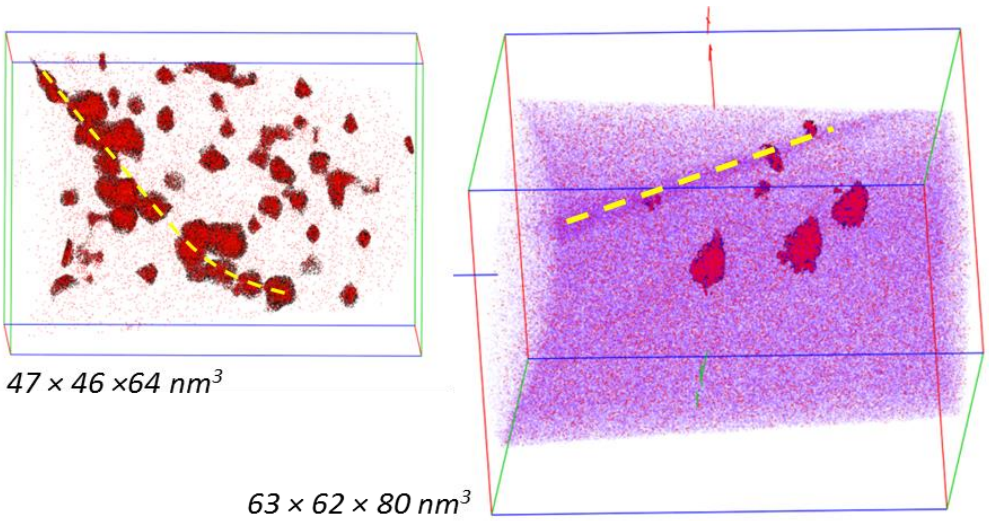

Figure 5.10: Two examples of 3D reconstructions of the ODS Fe14Cr extruded bar. Cr is in purple, Y, Ti and O are in red and Fe is in black. Y-Ti oxides are highlighted. Grain boundaries are materialized by yellow dashed lines.

Here again, a high level of Fe and Cr is observed in the particles and is attributed to field evaporation artefacts. The particle stoichiometry considering only Ti, Y and O is nearly (29.5 ± 0.8)%Ti, (15.5 ± 0.7)%Y and (55.0 ± 0.9)%O for particles inside matrix as well as particles at GB. The ratio Cr over Fe measured in the particles, as well as concentration profiles along particles long axis indicate that there are surrounded by Cr enriched shell.

5.5 Neutron diffraction texture measurements

The analysed sample of ODS Fe14Cr was provided by CIEMAT. Results of EBSD measurements obtained before for this material were reported in Ref. [15]. The sample position and orientation are shown in Figure 5.11. The complete diffraction pattern of ODS Fe14Cr is presented in Figure 5.12. The (110) and (200) reflections were selected to determine two independent pole figures, shown in Figure 5.13. A strong α-fiber

was observed, with the (110) direction parallel to the extrusion direction. The corresponding ODF was obtained by the method presented in [3], [18] and is shown in Figure 5.14. In addition to α-fiber, two more components can be identified, (001)[-1-10] and (111)[0-11]. There is therefore good qualitative agreement with the results obtained by EBSD and X-ray diffraction, as well as with previous neutron diffraction studies, such as [19], carried out to characterize the texture in similar ODS steels. Sampling a much larger volume, with higher statistics, and measuring the whole pole figure are the main advantages of the neutron technique with respect to EBSD and X-rays; they result in a more accurate determination of the ODF. A continuation of this study should primarily concern the evolution of the different texture components under annealing; *in-situ* heating is also possible, but with a linear size limitation of approximately 5 cm for this instrument. Finally, repeating with higher resolution the diffraction pattern shown in Figure 5.12 would allow to check the presence of minority phases, as it has already been done for a 9 Cr-ODS [20], and improve the crystallographic characterization of this sample.

ACKNOWLEDGEMENTS

The investigated sample of ODS Fe14Cr was kindly provided by CIEMAT. The neutron diffraction texture measurements and related data treatment were carried out in the frame of an agreement between the ENEA and the Helmholtz Zentrum Geesthacht (HZG). Dr. W. Gan, HZG responsible scientist for the STRESS-SPEC instrument at FRM II reactor, is gratefully acknowledged for invaluable help.

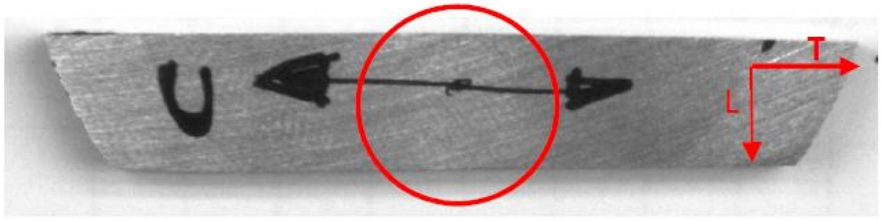

Figure 5.11: Investigated sample, cut from ODS Fe14Cr bar. The defined coordinate system for the neutron diffraction measurements is indicated, the extrusion direction is perpendicular to the plane of the figure; the diffracting volume (inside the red circle) is also shown.

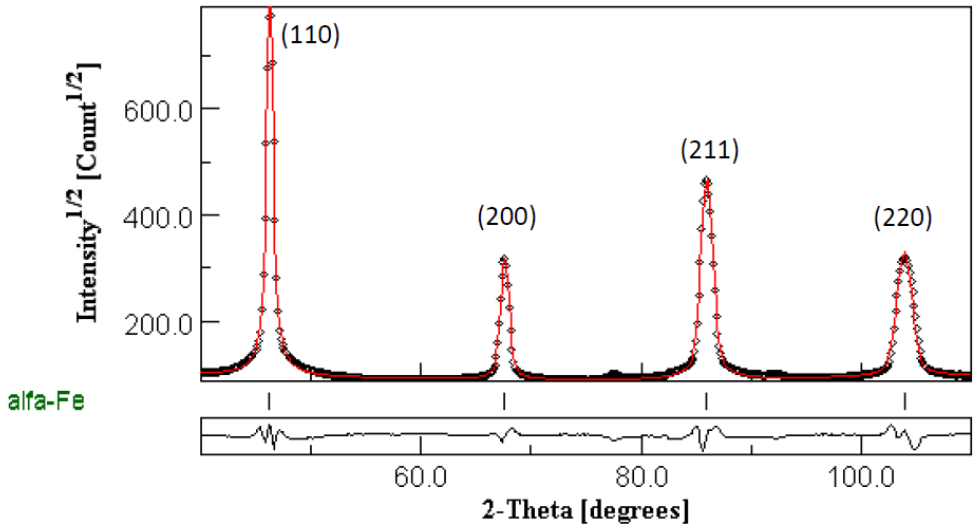

Figure 5.12: 2θ scan diffraction pattern of the 14 Cr-ODS sample.

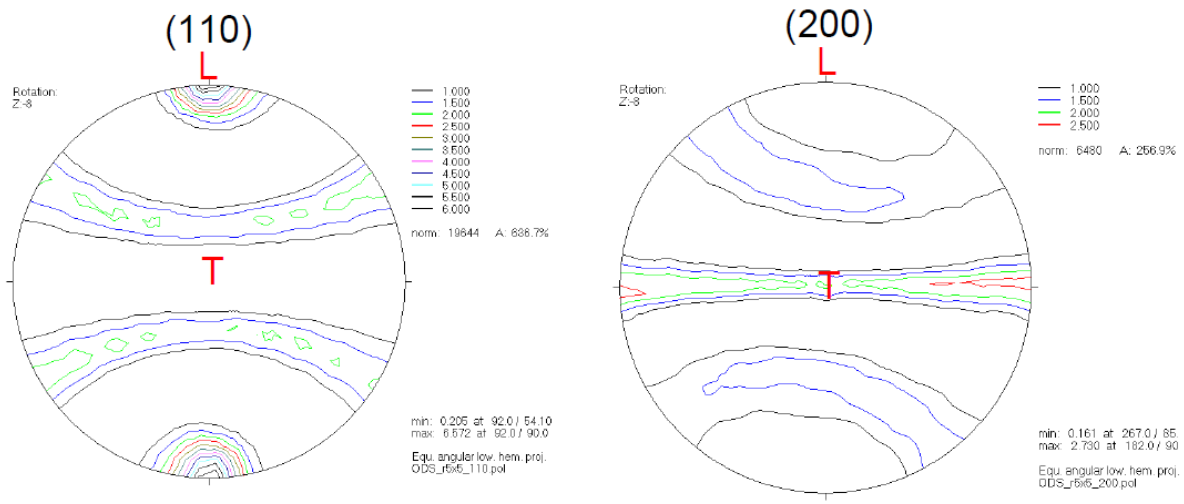

Figure 5.13: Measured (110) and (200) pole figures for the 14Cr- ODS sample.

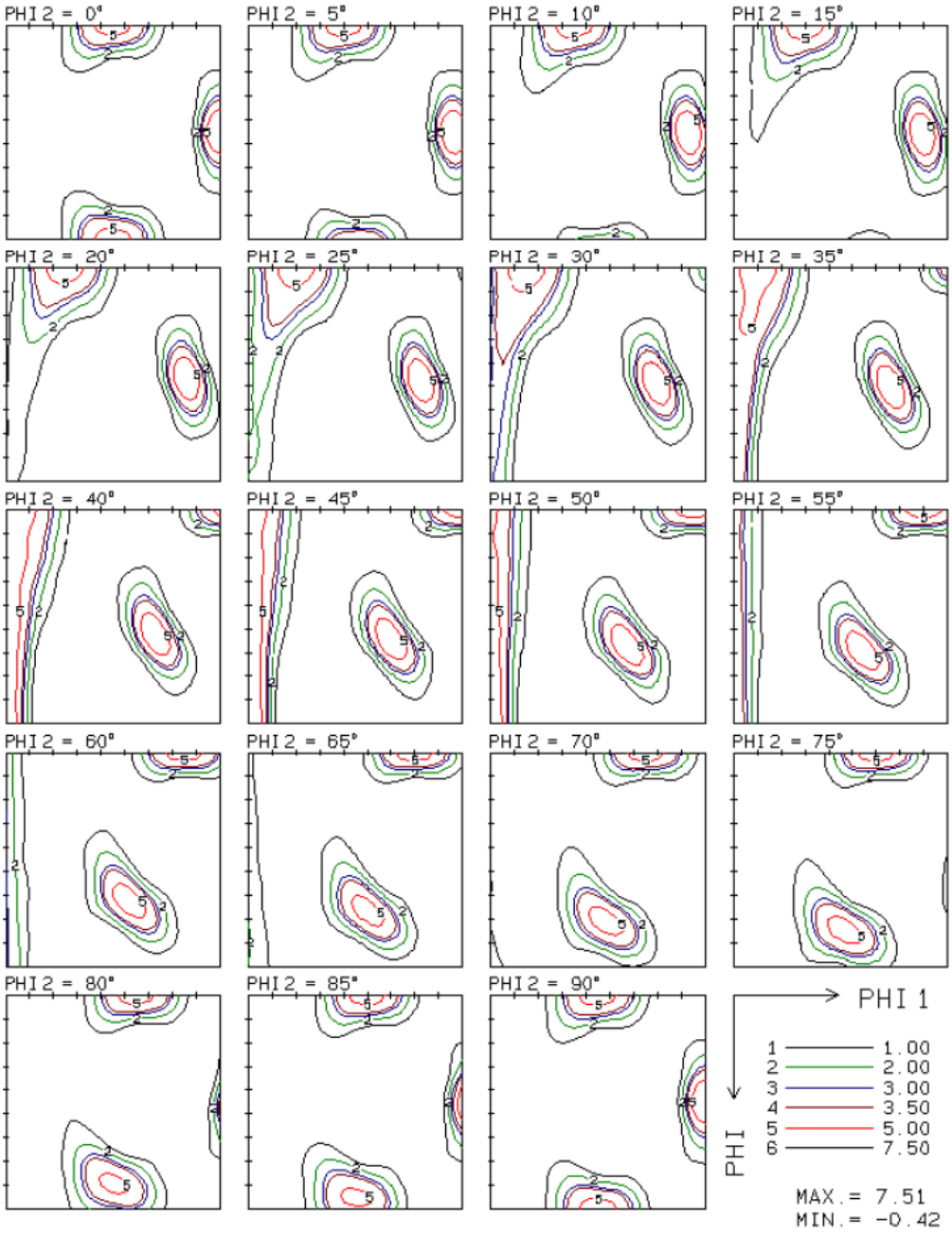

Figure 5.14: Even ODF of the 14Cr-ODS sample, obtained from the pole figures of Figure 5.13.

5.6 Tensile properties

The main tensile properties for the studied ODS steels at room temperature are summarized in Table 5.3. Clearly, ODS Fe14Cr steel exhibits highest strength of all tested materials. In addition, the advantage of heat treatment on ODS Fe9Cr steel is apparent from the improvement in strength. Nevertheless, reduction in total elongation/ductility is obvious. All steels manifest significant strain hardening with the highest for as-received ODS Fe9Cr F steel. Interestingly, under as-received condition ODS Fe9Cr steel exhibited a yield point phenomenon which indicates the presence of carbon in solid solution at interstitial sites [12], which is coherent with APT measurements. The influence of temperature on tensile properties with microstructural evolution and fracture characteristics are reported separately, see Refs. [12,13,21].

Table 5.3: Tensile data for the studied ODS steels at room temperature, for actual tensile curves and more see Refs. [12,13].

Alloy	Yield stress (MPa)	Ultimate strength (MPa)	Uniform elongation (%)	Total elongation (%)	Strain hardening (%)
ODS Fe9Cr F	740	903	10.3	20.9	18.1
ODS Fe9Cr TM	929	1052	2.7	7.6	11.7
ODS Fe14Cr F	1080	1126	9.1	20.9	4.1

5.7 Summary of results on as-received and quenched & tempered materials

The average characteristics of the microstructure and nanoparticle size distributions derived from different experimental techniques for the as-received ODS Fe9Cr, quenched and tempered ODS Fe9Cr and ODS Fe14Cr are listed in Table 5.4 to Table 5.6, respectively. The most probable estimates of the microstructure parameters needed for the yield stress prediction are printed in bolt. These estimates are summarized in Table 5.7 along with the measured values of the yield stress.

Table 5.4: Experimental results obtained for as-received ODS Fe9Cr extruded bar (lot L22-M1).

Technique	d_g (μm)	ρ (10^{14} m^{-2})	d_p (nm)	N_p (10^{22} m^{-3})	particle type (ratio Y-Ti-O)
Microstructure			Ferritic		
APT	-	-	5.1 ± 0.8	2.7 ± 0.5	close to 1-1-2
SANS	-	-	3.5 ± 0.2	12.3	consistent with 2-2-7 or 2-1-5
TEM		0.46 ± 0.1	(4.1± 0.9)	15 ± 4	
EBSD	1.19	-	-	-	-
Selected value	**1**	**0.5**	**4**	**10**	-

Table 5.5: Experimental results obtained for quenched and tempered ODS Fe9Cr extruded bar (lot L22-M1).

Technique	d_g (μm)	ρ (10^{14} m^{-2})	d_p (nm)	N_p (10^{22} m^{-3})	particle type (ratio Y-Ti-O)
Microstructure	tempered martensitic (cooling rate may differ from lab to lab)				
SANS*	-	-	3.5 ± 0.2	12.3	consistent with 2-2-7 or 2-1-5
TEM-1	0.25 **	-	(10 ± 5)	(0.1)	2-2-7
TEM-2		3.4 ± 1.0	4.7 ± 0.5	8 ± 2	
EBSD	0.46	-	-	-	-
Selected value	**0.5**	**3**	**4**	**10**	-

* SANS indicates equal size distributions for as-received and quenched + tempered ODS Fe9Cr
** Lath width

Table 5.6: Experimental results obtained for ODS Fe14Cr extruded bar (lot J27-M2).

Technique	d_g (µm)	ρ (10^{14} m^{-2})	d_p (nm)	N_p (10^{22} m^{-3})	particle type ratio Y-Ti-O
APT	-	-	2.8 ± 1.5	16.1 ± 1.7	close to 1-2-4
SANS*	-	-	2.3 ± 0.1	44 12	-
TEM-1	0.45	≈5	4	>2	-
TEM-2		**	2.2	32 ± 6	
EBSD	0.51	-	-	-	-
Selected value	**0.5**	**5**	**2.4**	**26**	-

* The second value is the difference between ODS 14Cr extruded bar and the yttria-free Fe14Cr reference.
** Large spatial variations

Table 5.7: Data sets for Fe-Cr model alloys, Eurofer 97 and ODS Eurofer reported in literature and average material parameters selected for ODS Fe9Cr and ODS Fe14Cr steels.

Alloy	Grain size, d_g (µm)	Dislocation density, ρ_d (10^{14} m^{-2})	Part. mean diameter, d_p (nm)	Number density, N_p (10^{22} m^{-3})	Yield stress, σ_y (MPa)
ODS Fe9Cr F	1	0.5	4	10	740
ODS Fe9Cr TM	0.5	3	4	10	929
ODS Fe14Cr F	0.5	5	2.4	26	1080

6 Results on thermally aged materials

6.1 SPT after low-temperature short-term and intermediate-temperature long-term treatments

The results are reported as the average value and the error bar calculated as the standard deviation of the tests performed in the same conditions. The load-deflection curves can be seen in Figure 6.1 to Figure 6.8 for the orientations L (left) and T (right).

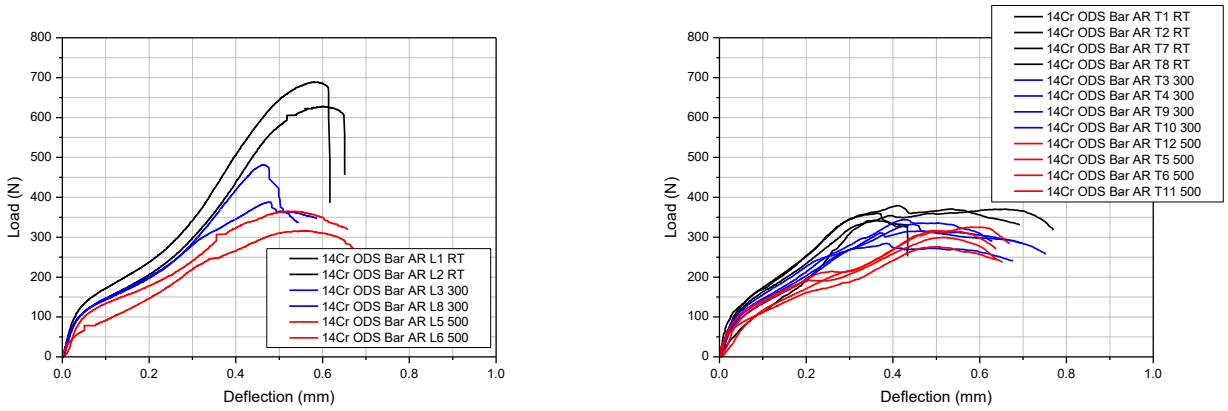

Figure 6.1: 14Cr ODS bar as received.

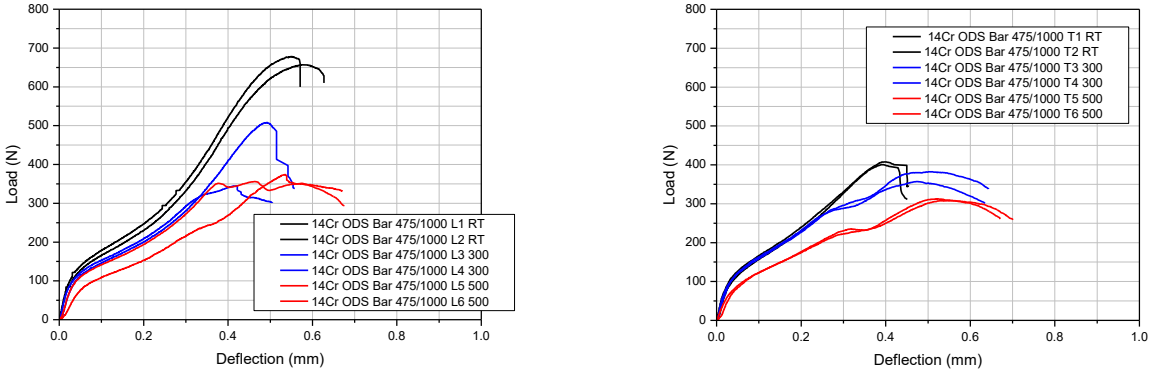

Figure 6.2: 14Cr ODS bar 475 ºC/1.000 h.

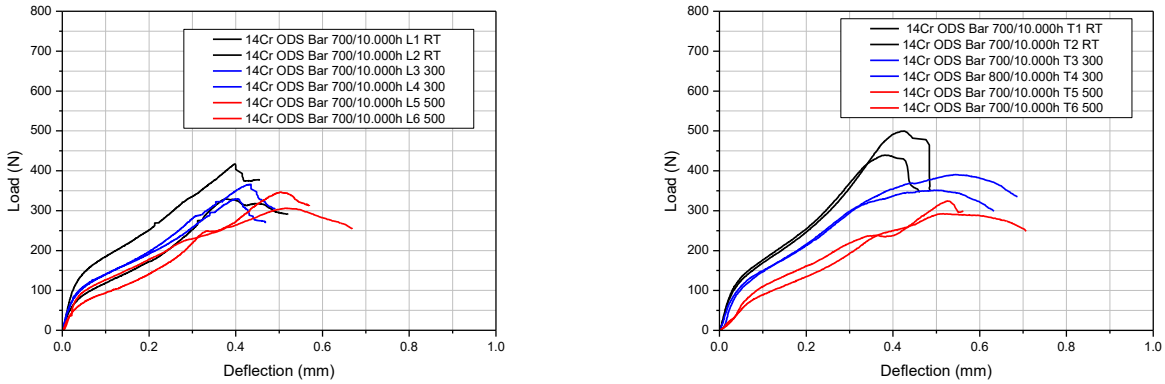

Figure 6.3: 14Cr ODS bar 700 ºC/10.000 h.

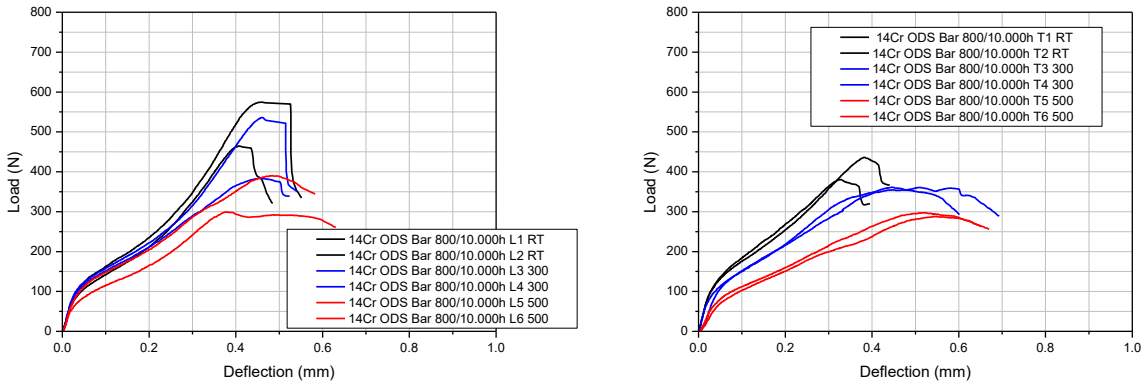

Figure 6.4: 14Cr ODS bar 800 ºC/10.000 h.

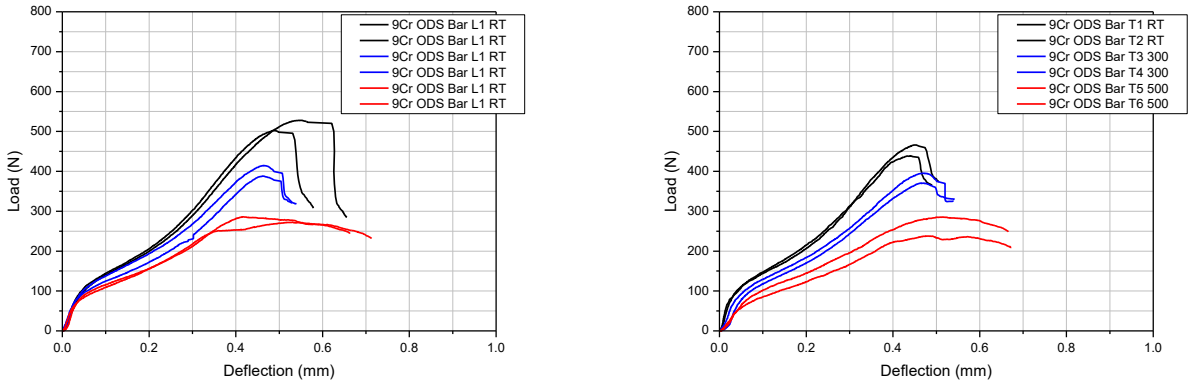

Figure 6.5: 9Cr ODS bar (tempered).

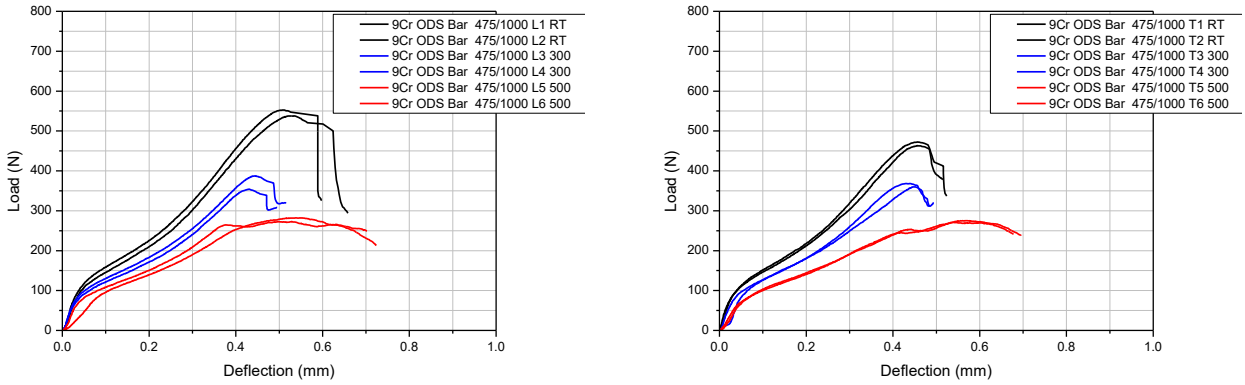

Figure 6.6: 9Cr ODS bar (tempered) 475 ºC/1.000 h.

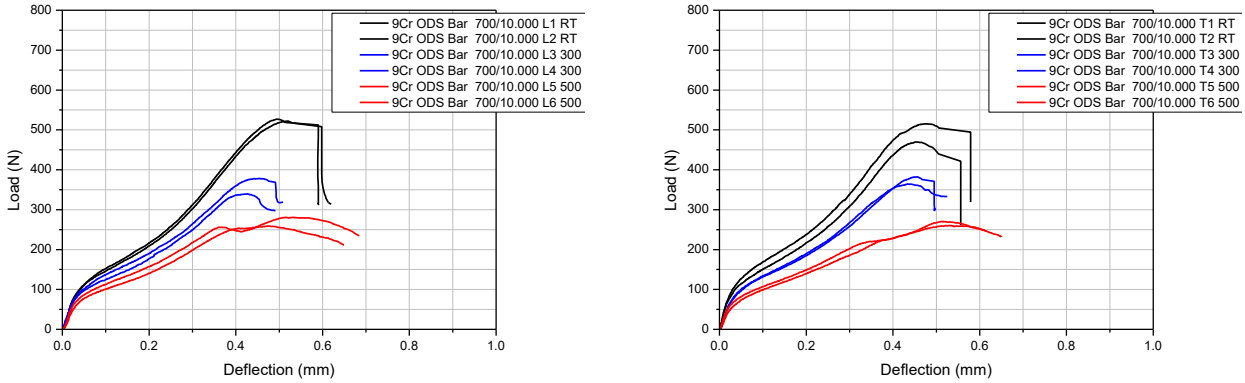

Figure 6.7: 9Cr ODS bar (tempered) 700 ºC/10.000 h.

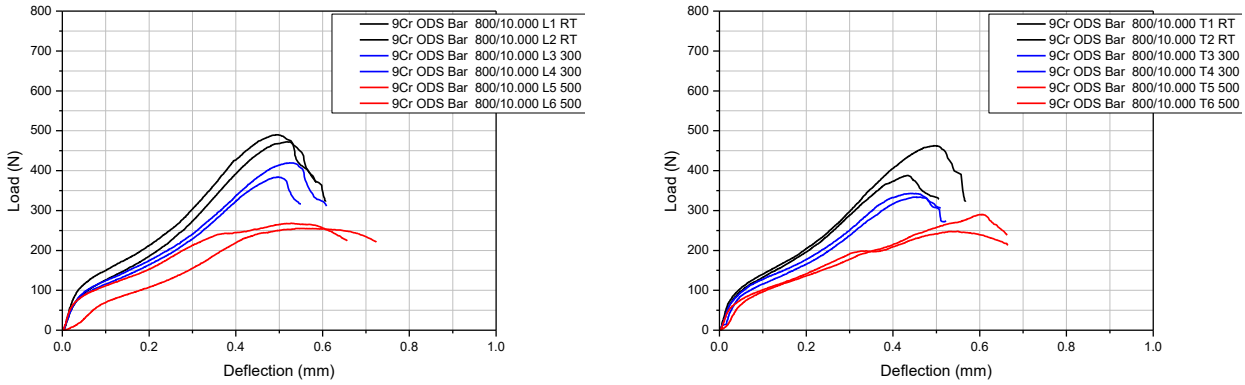

Figure 6.8: 9Cr ODS bar (tempered) 800 ºC/10.000 h.

A comparison of SPT parameters obtained for the as-received materials tested in the L- and T-direction provides insight into the anisotropy of the material. Significant anisotropy was observed for 14Cr ODS bar. This anisotropy is also shown on tensile and creep tests within GETMAT project and it is due a morphological and crystallographic texture showed by this material. These results confirm previous small punch tests performed with larger specimens (6 mm diameter, 0.500 mm thickness) on the same bar. As can be seen in Figure 6.9, the specimens with T orientation show a decrease in load (strength) and a decrease on small punch energy, that indicate a less ductile behaviour for the transverse oriented specimens.

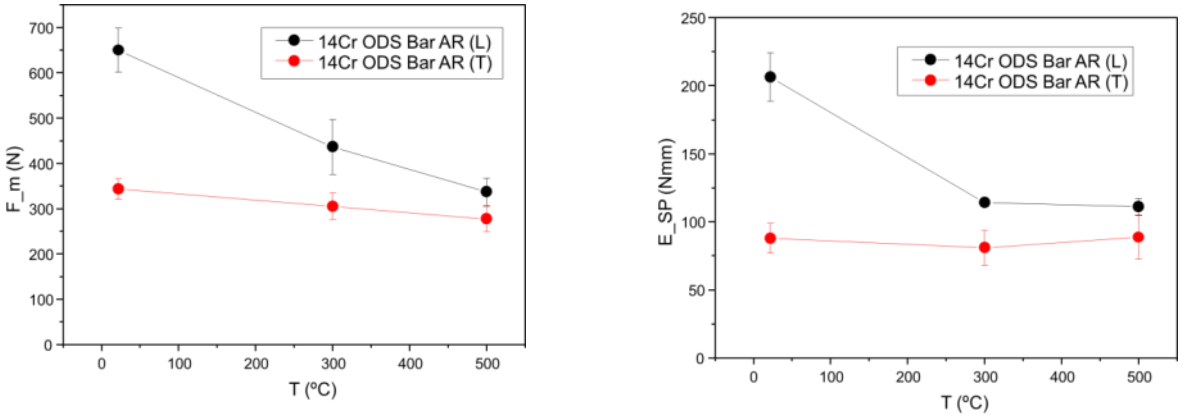

Figure 6.9: 14Cr ODS bar as received: Effect of specimen orientation on the maximum load and small punch energy.

This anisotropy can be also observed on the load-deflection curves as seen in Figure 6.10.

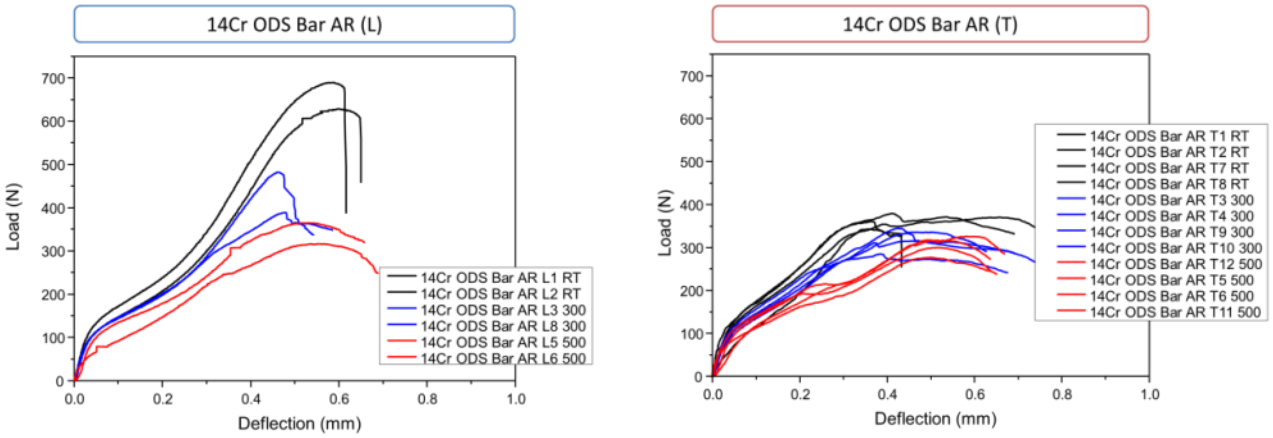

Figure 6.10: 14Cr ODS bar as received: Effect of specimen orientation on load-deflection curves.

This anisotropy is no so evident for the tests performed in the 9Cr ODS bar (after tempering), except for room temperature tests, see Figure 6.11. By comparing both bars, the 14Cr ODS bar show a better mechanical behaviour than the 9Cr ODS bar (tempered) in strength (higher load) and ductility (higher SP energy), see Figure 6.12.

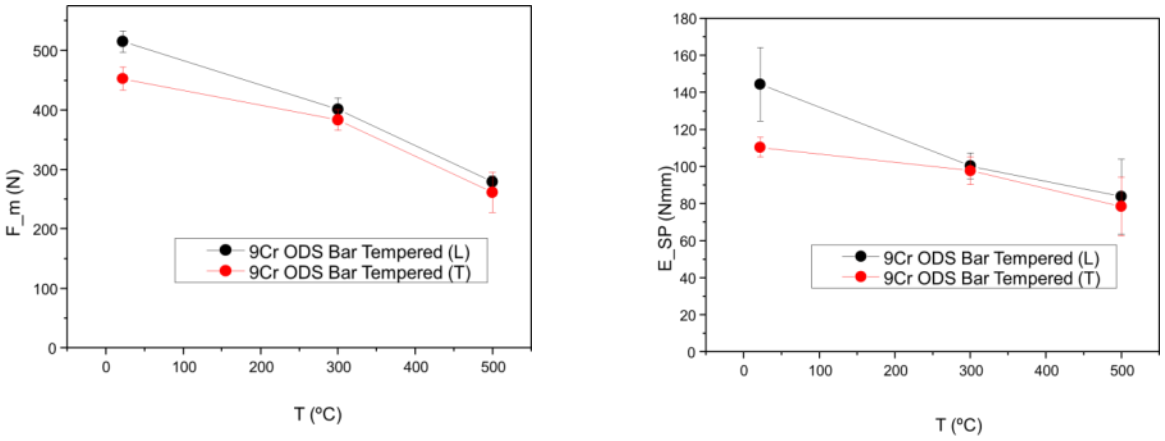

Figure 6.11: 9Cr ODS bar as received: Effect of specimen orientation on the maximum load and small punch energy.

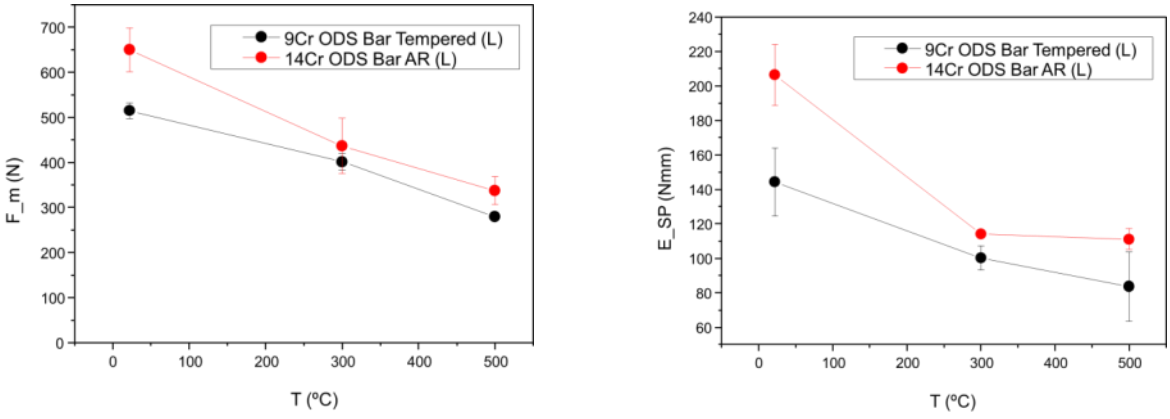

Figure 6.12: Comparison of the 14Cr ODS bar and 9Cr ODS bar in the as received condition: maximum load and small punch energy.

6.2 High-temperature short-term treatments

6.2.1 Hardness

The hardness of the materials was measured after aging and is plotted in Figure 6.13. The values for MAT-1 contain a large scatter and error-bars. This is due to the bi-modal microstructure which is also shown in the IPF maps (Figure 6.14). The hardness for MAT-1 drops steadily with increasing aging times and temperatures. It reaches its minimum at 2500 h/1100 °C. MAT-2 showed some variations in the hardness values, but retained at least the as-received values (when aged at 900 °C). The steady increase in hardness for MAT-3 at 900 °C could not be explained.

Ageing at 1100 °C for 2500 hours lowered the hardness significantly for all tested materials up to a maximum drop of 100 HV30 for MAT-1. MAT-4 was not plotted since it did not give reliable values, since ageing took place within the austenite regime and the final hardness was dependent on the transformation to ferrite/martensite while cooling.

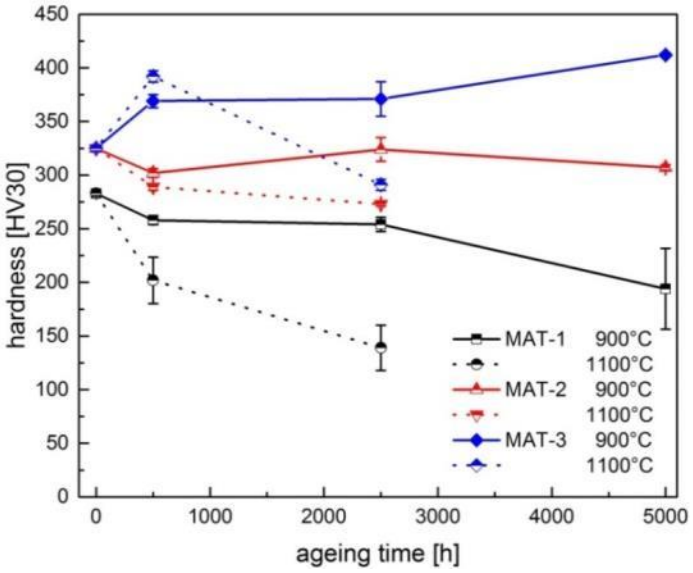

Figure 6.13: Hardness measurements of the materials after different aging conditions.

6.2.2 Microstructure

When aged at 900 °C for very long times (5000 h) the MAT-3 shows only minor changes in the microstructure and only beyond 500 h. Up to 500 h ageing, the microstructure is unaffected. This is shown in Figure 6.14.

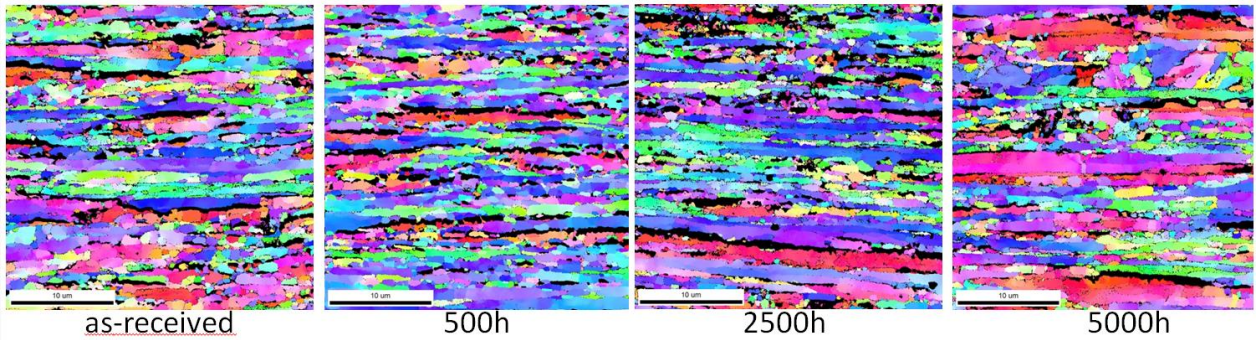

Figure 6.14: MAT-3 after ageing at 900 °C (EBSD inverse pole figure maps).

The grain orientation spread (GOS) can be used to measure the state of the microstructure. Large values for orientation spread indicate deformed microstructures. Very low values (<0.5) would correspond to recovered or recrystallized states. As expected from the IPF maps, the GOS does not change significantly over ageing time (Figure 6.15) for MAT-3. However, orientation gradients, which increase the GOS values are present in all of the materials conditions. The grains are not recrystallized after the ageing treatment.

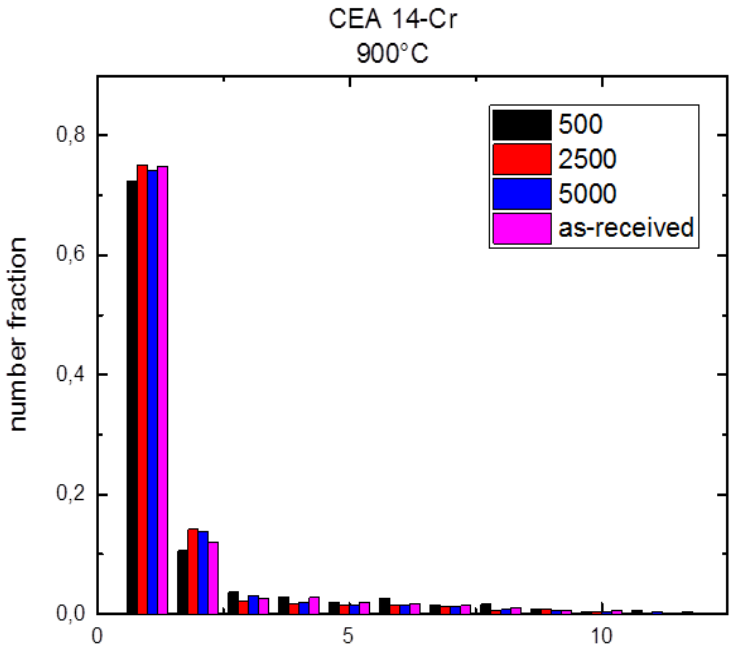

Figure 6.15: Grain orientation spread after different ageing conditions (MAT-3).

The grain sizes (GS) were calculated and plotted into histograms (Figure 6.16). The mean value of the GS increases by 21 nm. This effect can be neglected, since the variation can also be influenced by sampled area of the material. We conclude that the microstructure is stable at 900°C.

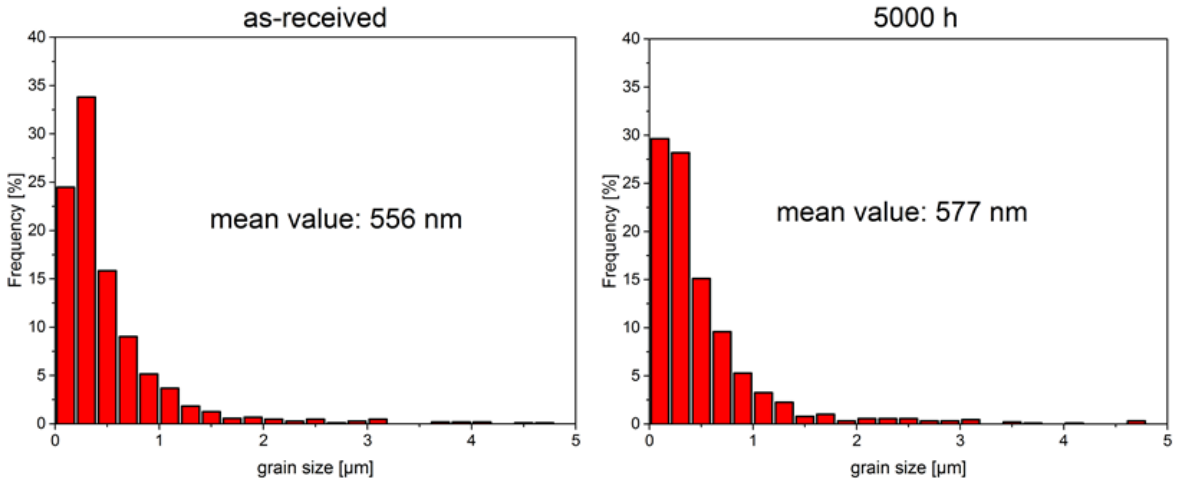

Figure 6.16: Grain size distribution before and after 5000 h at 900 °C (MAT-3).

Figure 6.17 shows an inverse pole figure map (IPF) of MAT-1 and MAT-3. The map was calculated using a grain definition of misorientations greater than 15°. The color can be linked to the state of the microstructure.

Color gradients within the grains indicate a deformed structure while as solid colors (low orientation gradients) would correspond to a recovered or recrystallized state. The pictures show, that the microstructure is not recovered in the as-received condition after hot-rolling (MAT-1) or hot-extrusion (MAT-3). Even ageing for 500 h does not produce significant changes in the microstructure. After 2500 h, this state changes for both materials. The gradients within the grains are mostly recovered. Massive grain growth can be observed in both materials. The grain size distributions calculated by EBSD are also displayed in Figure 6.18.

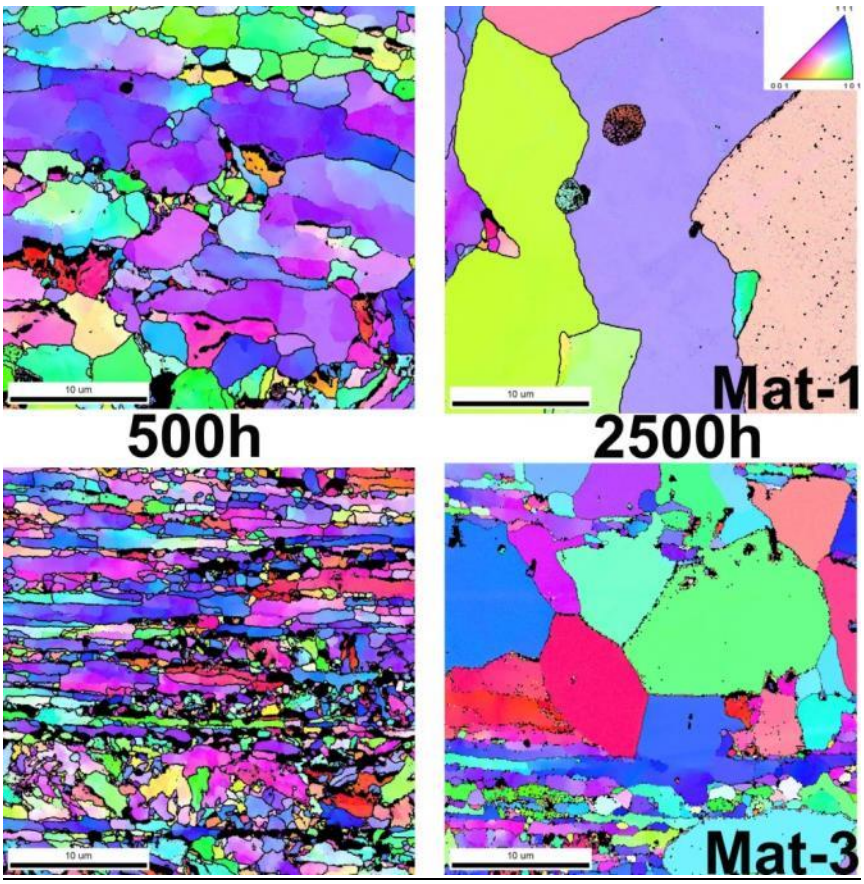

Figure 6.17: Inverse pole figure maps of the materials aged at 1100.°C.

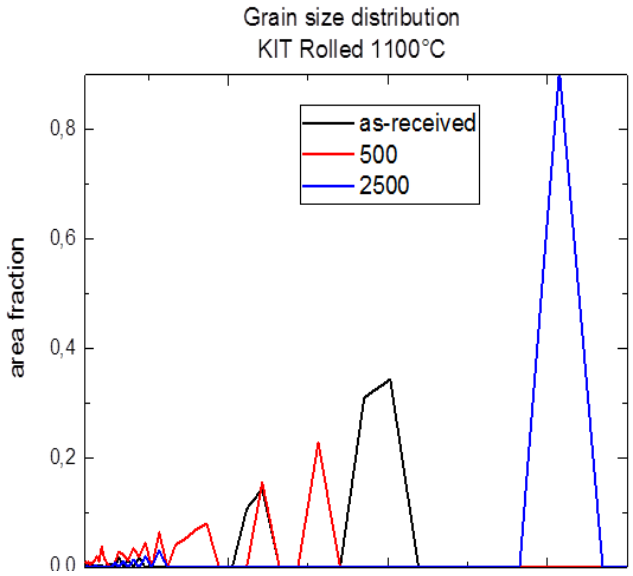

Figure 6.18: Grain size distribution after ageing at 1100 °C (MAT-1) calculated by EBSD.

Ageing of MAT-4 at 1100 °C destroyed the typical fine grained structure of 9%-Cr ODS alloys. The temperature is already in the gamma regime and causes massive grain growth. The ODS particles were not effective to pin the grain boundaries and block the grain growth. Particle size distributions were not measured, but we assume that a coarsening of the particles also took place at this temperature. Figure 6.19 shows the microstructure after 2500 h ageing. Further ageing was not performed but the grains may still growth further when treated for longer times. Since the cooling of the materials was performed within the vacuum tubes, the critical cooling speed for a martensitic transformation was not achieved for MAT-4. This resulted in a fully ferritic matrix with poor mechanical properties.

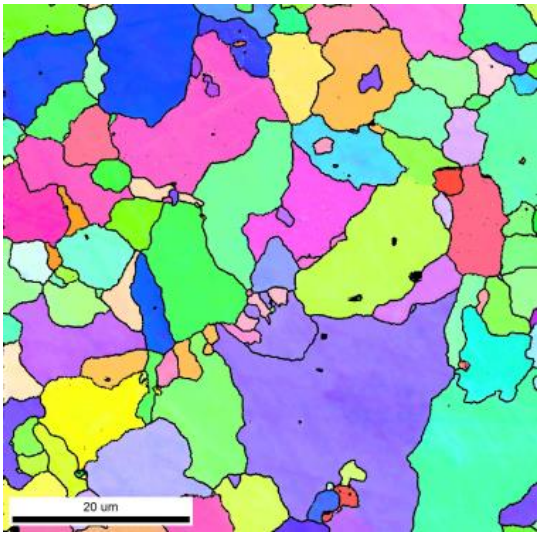

Figure 6.19: EBSD grain map of material MAT-4 aged at 1100 °C (2500 h).

7 Results on ion-irradiated materials

7.1 Nanoindentation

The results presented in this section have partly been published by the contributing project partners in Ref. [22].

7.1.1 Basic characterization of the unirradiated reference materials

ODS Fe14Cr, non-ODS Fe14Cr and ODS Fe9Cr-A (as received) exhibit a ferritic microstructure. A tempered martensitic microstructure is present in ODS Fe9Cr-B (quenched and tempered) and ODS-Eurofer due to a heat treatment involving austenization, quenching and tempering. Inverse pole figure maps of all materials obtained by EBSD are shown in Figure 7.1. The normal vector of the EBSD sample surfaces was chosen to be parallel to the extrusion/rolling direction. Grain size (d_g) was determined using a misorientation angle of 10°. A fine grain size distribution was observed in all materials. The average values of grain size are 0.59 µm (non-ODS Fe14Cr), 0.44 µm (ODS Fe14Cr), 1.20 µm (ODS Fe9Cr-A), 0.73 µm (ODS Fe9Cr-B), and 0.73 µm (ODS-Eurofer [15]), as summarized in Table 7.1. non-ODS Fe14Cr (Figure 7.1a) and ODS Fe14Cr (Figure 7.1b) exhibit smaller average grain size compared with ODS Fe9Cr and a texture with <110> direction preferentially oriented parallel to the extrusion direction. The added ODS particles contribute to forming smaller grains in ODS Fe14Cr. Compared with ODS Fe9Cr-A, which has the coarsest grains, the grains in ODS Fe9Cr-B are refined due to the quenching and martensitic trans-formation. It is well known that the grains of ODS Fe14Cr are elongated in the extrusion direction [14]. This is not taken into account in the average grain size determined from EBSD analyses performed for transverse samples. However, it is reasonable to assume that the short dimensions of the grains separated by high-angle boundaries are most relevant for grain boundary hardening as well as sink strength determination. Indeed, the sink strength is related to the inverse of the mean distance a point defect travels in the solid before becoming trapped [9].

The results of the SANS experiments of the unirradiated materials have been reported in sections 5.3. and 5.7 and in Ref. [22]. From the SANS results, the size, number density and volume fraction of the oxide nanoparticles were calculated. The results are also listed in Table 7.1. A TEM micrograph is shown in Figure 7.2 for ODS Fe9Cr-A as an example. The measured (ODS Fe9Cr-A and -B) or reported (ODS Fe14Cr [23] and ODS-Eurofer [24]) dislocation densities are given in Table 7.1. For non-ODS Fe14Cr the same dislocation density as for ODS Fe14Cr is assumed.

Table 7.1: Microstructure, indentation hardness and irradiation-induced hardness increase at reference depth of 200 nm.

Material	non-ODS Fe14Cr	ODS Fe14Cr	ODS Fe9Cr-A	ODS Fe9Cr-B	ODS-Eurofer
Grain size, d_g (µm)	0.59	0.44	1.20	0.73	0.73
Oxide particle diameter, d_p (nm)	2.3	2.3	3.5	3.5	3.8
Oxide particle density, N_p (10^{22} m^{-3})	32.0	44.0	12.3	12.3	11.5
Oxide particle volume fraction, f_p (%)	1.09	1.46	0.51	0.51	0.72
Dislocation density, ρ (10^{14} m^{-2})	5.0	5.0	0.46	3.4	7.0
H_{IT} (GPa)	4.28	4.57	3.55	4.19	4.46
ΔH_{IT} (300 ºC) (GPa)	0.58	0.69	1.22	0.96	1.02
ΔH_{IT} (500 ºC) (GPa)	0.31	0.26	1.15	0.74	0.61

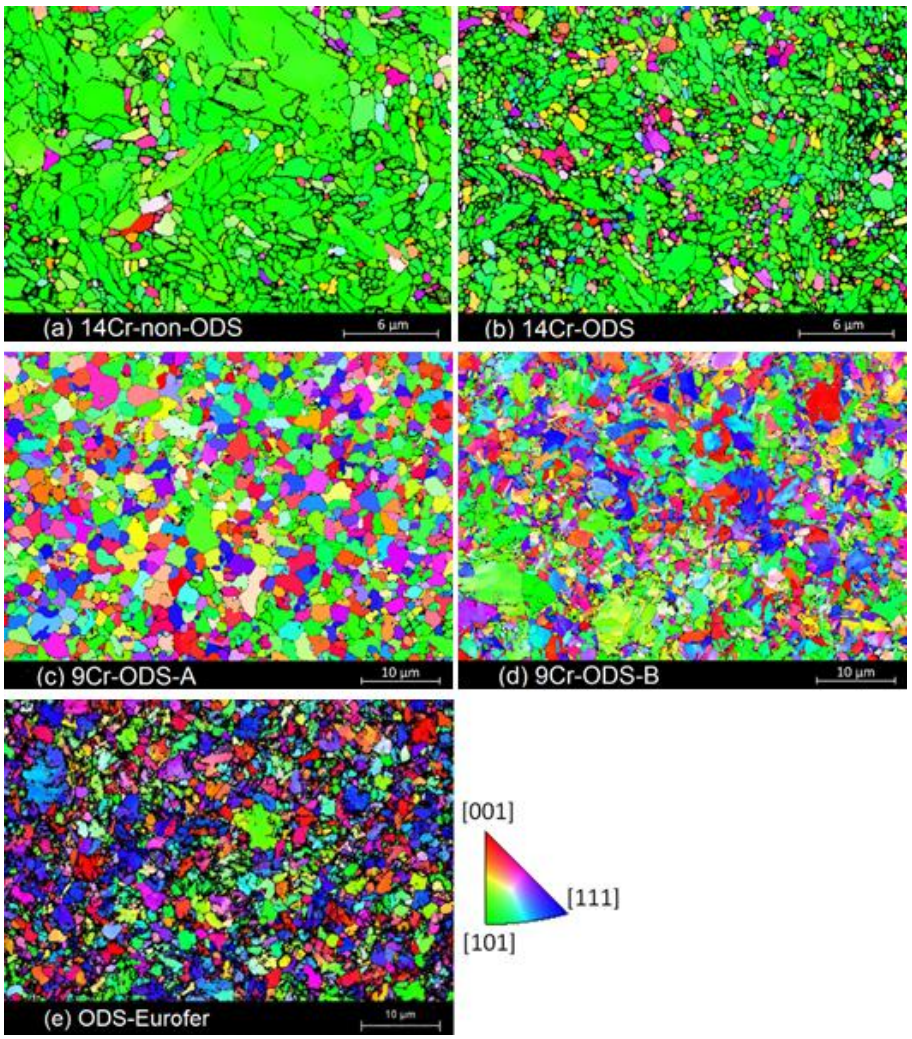

Figure 7.1: Inverse pole figure maps obtained by EBSD of non-ODS Fe14Cr (a), ODS Fe14Cr (b), ODS Fe9Cr-A (c), ODS Fe9Cr-B (d) and ODS-Eurofer (e) with the normal vector of the sample surface chosen parallel to the extrusion/rolling direction.

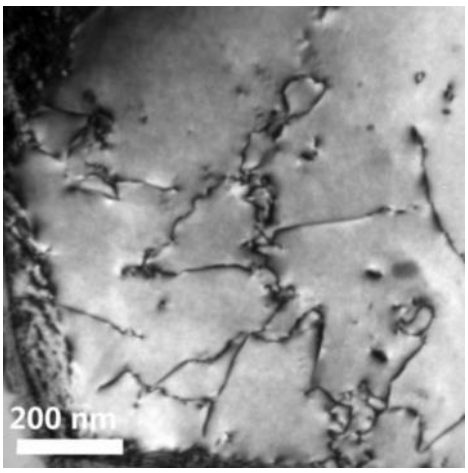

Figure 7.2: Bright field image for unirradiated ODS Fe9Cr-A.

7.1.2 Nanoindentation on unirradiated and as-irradiated materials

The results of the nanoindentation experiments performed for the unirradiated and as-irradiated conditions of the investigated ODS alloys are provided in Figure 7.3, Figure 7.4 and Table 7.1. For the irradiation conditions see section 3.2.

Figure 7.3a shows the indentation hardness measured as a function of contact depth for all unirradiated materials. The individual points represent values averaged over all indentations. The error bars represent the mean error of the average value. Figure 7.3a shows that 14Cr-ODS exhibits the largest and 9Cr-ODS-A the lowest hardness at all depths. The indentation hardness of the unirradiated materials is taken as reference to calculate the irradiation-induced hardness changes.

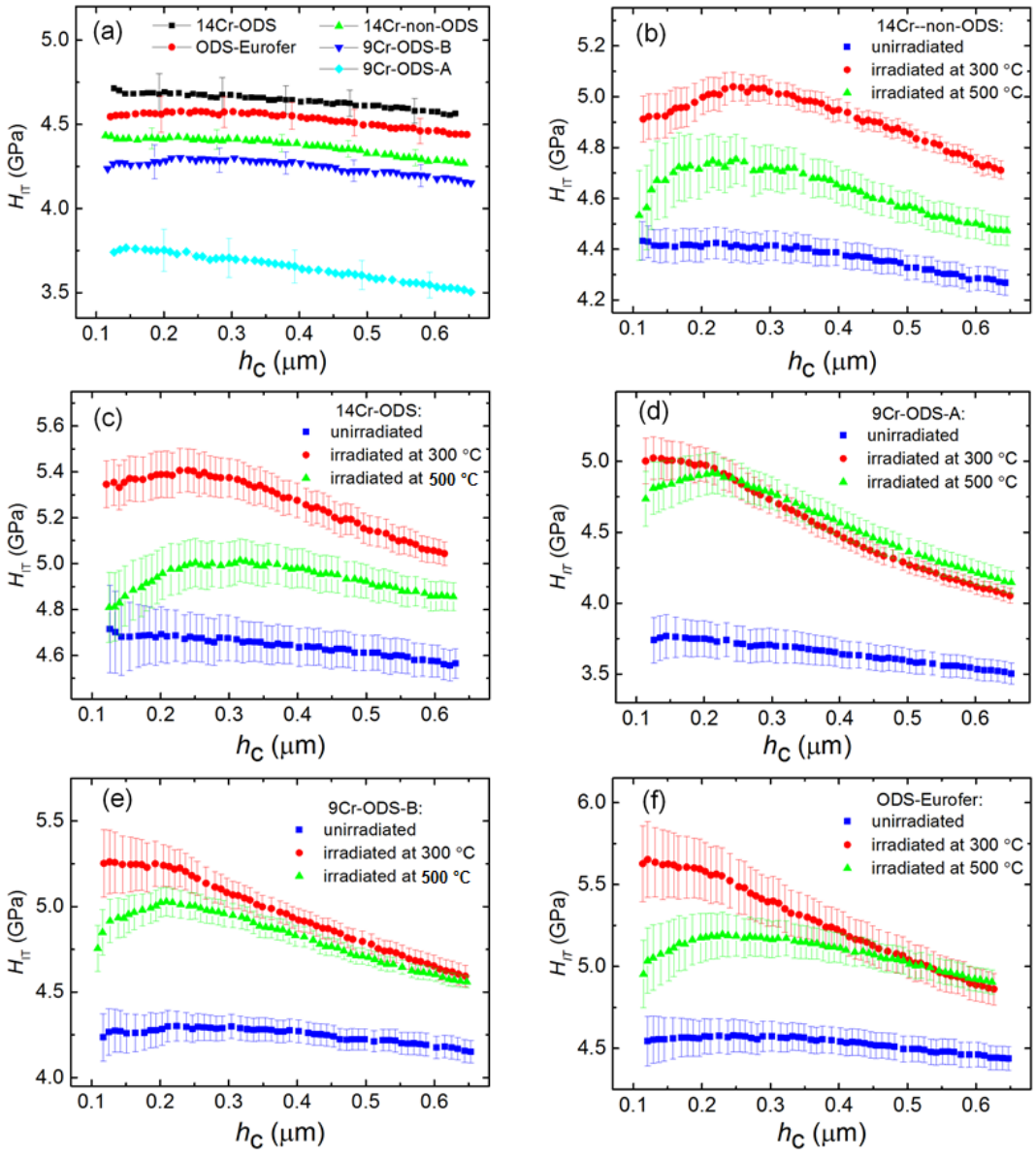

Figure 7.3: Nanoindentation hardness as a function of contact depth: (a) comparison of hardness of unirradiated materials, (b) – (f) comparison of hardness change after irradiations at 300 ºC and 500 ºC.

Figure 7.3b to f represent the indentation hardness as a function of contact depth after Fe-ion irradiation at 300 ºC and 500 ºC up to 10 dpa and for the unirradiated reference samples. Irradiation-induced hardness increase occurred at both temperatures for all materials, but is more pronounced at 300 ºC. All plotted curves for 300 ºC display an approximately flat stage and a subsequent gradual reduction. The curves measured

after irradiation at 500 ºC show lower hardness at low depth. This means that the hardening produced by irradiation was weaker in the near-surface layer. The indentation hardness values taken at the reference depth of 200 nm are graphically summarized in Figure 7.4a for all unirradiated and irradiated materials. The differences between the hardness of the irradiated and the corresponding unirradiated materials are given in Figure 7.4b.

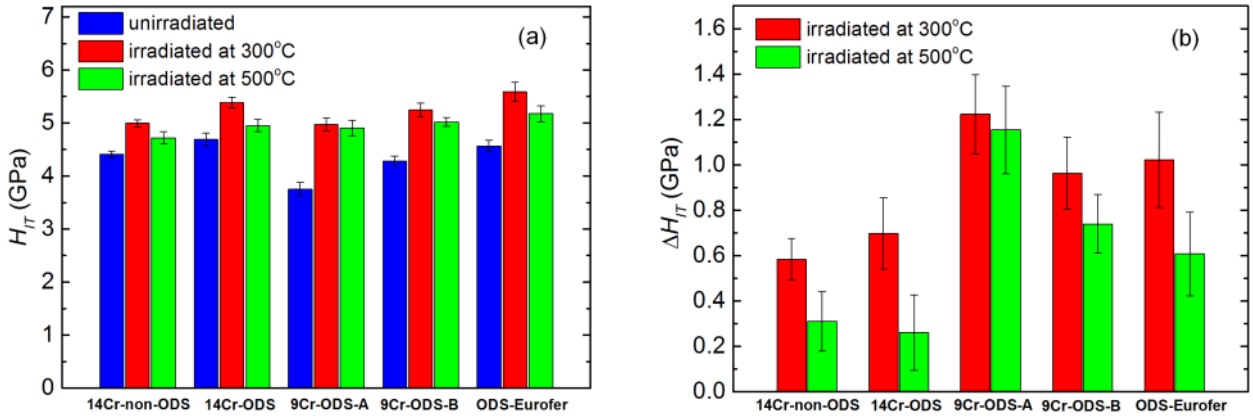

Figure 7.4: Representations of hardness value (a) and corresponding hardness increase (b) chosen at a reference depth of 200 nm.

7.2 TEM

The microstructure induced by ion irradiation in Fe-14Cr-ODS has been studied by TEM. The irradiation temperature has been 300 ºC and the dose reached has been 10 dpa. The results are presented below.

7.2.1 Preirradiated microstructure

For results obtained by means of TEM for the as-irradiated microstructures, the reader is referred to Sections 5.1 and 7.1.1.

7.2.2 Microstructure after ion irradiation at 300 ºC, 10 dpa

Figure 7.5 shows the images from one of the grains closer to the specimen surface. Individual images are stitched together in order to cover a wider region. It shows the microstructure of a cross section specimen fabricated by FIB. The in-depth microstructure is compared to the depth damage profile estimated by SRIM code in order to correlate the observed microstructure with the damage profile. As observed in this figure, the radiation induced microstructure is not homogeneous. The inhomogeneity consists in the appearance of bands which alternate regions of high and low density of dislocations and dislocation loops. The bands appear parallel to the specimen surface and the regions showing high density correspond, approximately, to the locations of the peaks of either the displacement damage or the concentration of injected interstitials. The latter is more plausible because the modulation of the displacement damage seems to be too weak to explain the pronounced modulation of the irradiation-induced microstructure. The approximate locations and major characteristics of the bands is summarized in Table 7.2. The presence of a fine dispersion of nano-oxides is also observed. They are better observed within the bands of low dislocation density, while their visibility is poorer at the bands with high density of other objects.

Table 7.2: Summary of observations, Fe-14Cr-ODS ion irradiated at 300ºC, 10 dpa.

Band label	Thickness (nm)	Comments
A	40	40 nm closer to the surface This region at the surface shows a high density of dislocations, and, possibly, other objects. It is difficult to to discern individual features. Its origin of it is not clear: it may be the ion irradiation or the final surface finishing applied to the sample.
B	100	Low dislocation density. Presence of nano-oxides and small loops.
C	110	Band of about 110 nm, centered at about 250 nm far from the surface, approximately where the peak of damage of the lower ion energy beam, 0,5 MeV, is placed according to SRIM calculations. This region shows a high density of different features: tangled dislocation lines mixed with dislocation loops and with nano-oxides.
D	240	Low dislocation density. Presence of nano-oxides and small loops.
E	250	Band of about 250 nm thick, centered at about 650 nm far from the surface, approximately where the peak of damage of the medium ion energy beam, 2 MeV, is placed according to SRIM calculations. This region shows a high density of different features: tangled dislocation lines mixed with dislocation loops and with nano-oxides.
F	350	Low dislocation density. Presence of nano-oxides and small loops.
G	350	Band of about 350 nm, centered at about 1350 nm far from the surface, approximately where the peak of damage of the higher ion energy beam, 5 MeV, is placed according to SRIM calculations. This region shows a high density of different features: tangled dislocation lines mixed with dislocation loops and with nano-oxides.

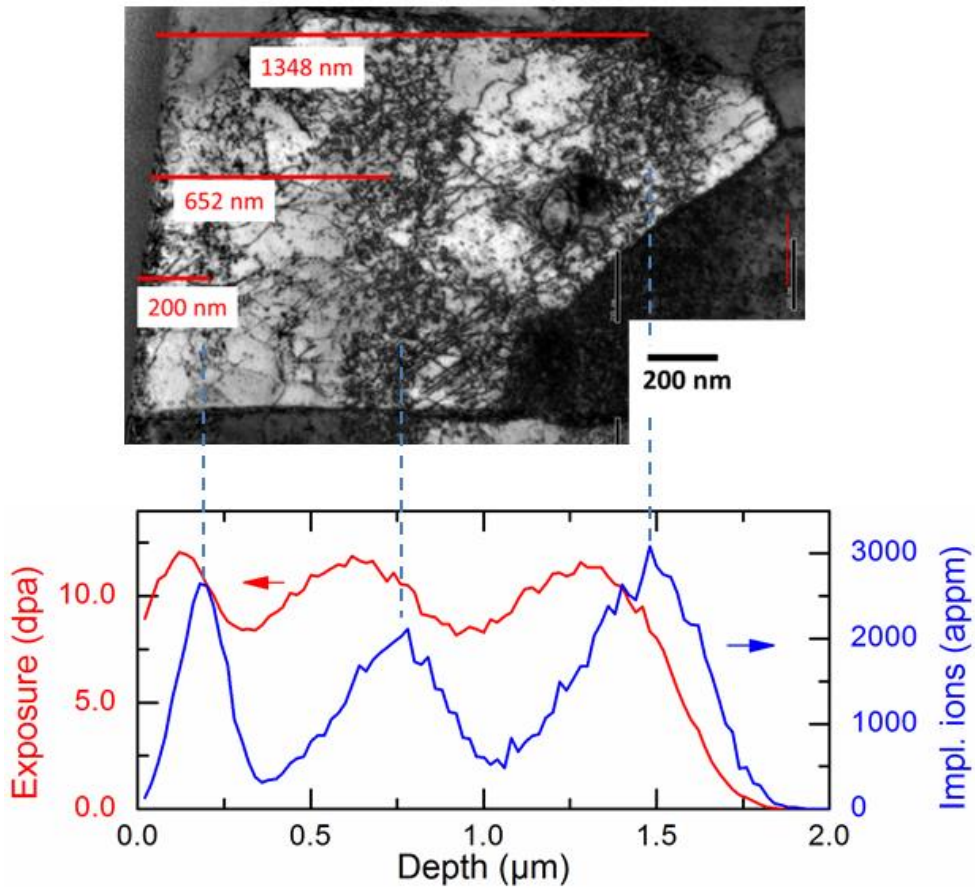

Figure 7.5: TEM images showing the microstructure of a *cross* section sample of Fe-14Cr-ODS ion irradiated at 300ºC, up to 10 dpa

8 Discussion

8.1 Microstructure of as-received and quenched+tempered ODS Fe9Cr

A variety of experimental methods including EBSD, neutron diffraction, TEM SANS and APT was applied to characterize the microstructure. As indicated in Table 5.4 to Table 5.6, the pieces of information gained from the application of these methods are partly complementary and partly overlap. The complementarity is important for both a complete description of the microstructure and a microstructure-based “prediction” of the yield stress to be obtained. Indeed, no single technique alone is capable of providing a full characterization of the microstructure. The cases of overlap can be used to cross-check and additionally substantiate the derived microstructure parameters.

The type of microstructure was derived from optical metallography, EBSD and TEM. The results confirm that as-received ODS Fe9Cr, quenched and tempered ODS Fe9Cr and ODS Fe14Cr are essentially ferritic, tempered martensitic, and ferritic, respectively. Occasional appearances of ferrite in quenched and tempered ODS Fe9Cr and of martensite in ODS Fe14Cr were found but will be ignored in the further analysis. The appearance of martensite in ODS Fe14Cr can only be explained in terms of spatial variations of the Cr content locally falling below the extension of the γ-range in the phase diagram. The information gathered from different techniques on grain size is consistent for each of the materials. EBSD is favorable in extracting the grain size, because it combines sufficient spatial resolution and sufficient statistics.

The dislocation density was derived exclusively on the basis of TEM. A considerable degree of heterogeneity was found with respect to the dislocation structure. However, rough estimates of the average dislocation density were derived from the analyses at different positions.

Information on the oxide nanoparticle distribution was derived from APT, TEM and SANS. The SANS results are distinguished by a probed volume (approximately 50 mm^3) that is many orders of magnitude larger than for TEM and APT and that allows macroscopically representative and statistically reliable size distributions to be obtained. On the other hand, SANS cannot resolve the composition of particles (in contrast to APT) nor discriminate between different types of nanoparticles of similar size. Taking into account the different sizes of the probed volumes and the observed heterogeneities of the spatial distribution of particles, the sizes and number densities of particles listed in Table 5.4 to Table 5.6 seem to be reasonably consistent. It is interesting to note that, based on SANS, quenching and tempering of ODS Fe9Cr did not change the size and number density of oxide nanoparticles. This peculiarity was utilized to separate the isolated effects of particle size distribution and microstructure (in terms of grain size and dislocation density).

8.2 Microstructure property correlation

The results presented in Table 5.4 to Table 5.7 allow a microstructure-based calculation of the yield stress of ODS alloys to be performed. The comparison of calculated and measured values of the yield stress will provide a much better understanding on the dominant hardening mechanisms, their relative contributions and their law of superposition in ODS steels. The target was not only to uncover a microstructure-yield stress correlation for the present set of project-related alloys, but also to ensure a physically sound asymptotic behavior over a wide range of microstructures. A detailed description of the procedure and results can be found in [11]. The present discussion is focused on the essentials.

The data set obtained within Task 4.1 of MatISSE was extended using data generated in the former EU project GETMAT and reported in the literature. The extended data set is given in Table 8.1. Both grain size and dislocation density of the materials from the extended data set vary over two orders of magnitude. The nanoparticle number density varies from practically zero to exceptionally high values achieved by advanced technologies of ODS steel fabrication.

Table 8.1: Data sets for Fe-Cr model alloys, Eurofer 97 and ODS Eurofer reported in literature and average material parameters selected for ODS Fe9Cr and ODS Fe14Cr steels.

Alloy	Grain size d_g (μm) [1)]	Dislocation density ρ_d (10^{14} m^{-2})	Part. mean diameter d_p (nm)	Number density N_p (10^{22} m^{-3})	Yield stress σ_y (MPa)
Fe2.5Cr	37	0.12	w/o	w/o	144
Fe5Cr	10	0.58	w/o	w/o	206
Fe9Cr	3	0.63	w/o	w/o	289
Fe12Cr	3	0.55	w/o	w/o	349
Eu97	2	2.2	w/o	w/o	550
ODS-Eu	0.5	7	3.8	11.5	1050
ODS Fe9Cr F	1	0.5	4	10	740
ODS Fe9Cr TM	0.5	3	4	10	929
ODS Fe14Cr F	0.5	5	2.4	26	1080

As a first trial, it is assumed here that the yield stress (σ_y) of the materials at room temperature can be given by a simple sum of strengthening contributions which is as follows:

$$\sigma_{\mathrm{y}} = \sigma_0 + \sigma_{\mathrm{s}} + \sigma_{\mathrm{g}} + \sigma_{\mathrm{d}} + \sigma_{\mathrm{p}} \tag{1}$$

where σ_0, σ_s, σ_g, σ_d and σ_p are the contributions from lattice friction, solid solution strengthening, grain size or Hall-Petch strengthening, dislocation forest strengthening and nanoparticles strengthening, respectively. Although pure linear summation according to Eq. (1) is an over-simplification, Eq. (1) may well serve as a road map to introduce the individual contributions separately. The lattice friction or Peierls-Nabarro stress (σ_0) is required to move a dislocation through the perfect lattice. Solid solution strengthening (σ_s) includes both the interstitial strengthening from the carbon in solid solution and the substitution strengthening from all substitutional elements. However, with respect to the present alloys, interstitial strengthening will have a negligible contribution since most of the carbon, present in appreciable amount only in ODS Fe9Cr steel, is already precipitated out in form of carbides. The strengthening effects of substitutional alloying elements in bcc iron matrix follow a simple expression as:

$$\sigma_{\mathrm{s}} = 0.00689\, k\, X^n \tag{2}$$

where X is the equilibrium concentration of substitutional elements in atomic percent, n = 0.75 for all elements, and k is the strengthening coefficient. The total substitutional strengthening effects were calculated for the extended set of alloys based on the knowledge of their composition [11]. Grain size or Hall-Petch strengthening (σ_g) expresses the influence of grain boundaries on the dislocation behavior. Indeed, dislocations are gradually stacked at grain boundaries and form pile-ups until they reach the threshold to pass to the next grain. This strengthening contribution can be estimated as:

$$\sigma_{\mathrm{g}} = \alpha_g G \sqrt{\frac{b}{d_g}} \tag{3}$$

Here $\alpha_g = 0.2$, G is the shear modulus, b is the Burgers vector and d_g is the mean grain size according to Table 8.1. Dislocation forest strengthening (σ_d) is due to the interaction between dislocations when a mobile dislocation interacts with another one which goes across its gliding plane. The contribution from dislocations strengthening can be estimated by Bailey-Hirsch relationship, which is widely accepted as:

$$\sigma_{\mathrm{d}} = \alpha_d MGb\sqrt{\rho_d} \tag{4}$$

where $\alpha_d = 1/3$ is an obstacle strength for dislocations by dislocations M is the Taylor factor and ρ_d is the dislocation density according to Table 8.1. Particle strengthening (σ_p) is due to the dispersed nano-oxide particles which act as impenetrable obstacles for dislocations glide. Several authors suggested detailed equations for calculating this contribution, which were partly based on knowledge or assumptions about the dislocation-particle interaction mechanism. For the present purpose, this degree of detail seems to be inappropriate, since different interaction mechanisms may be assumed to operate simultaneously depending upon various factors such as particle type, their degree of coherency etc. It is therefore reasonable to use the simplest scaling equation based on the dispersed barrier hardening concept with an empirical constant:

$$\sigma_{\mathrm{p}} = \alpha_p MGb\sqrt{N_p d_p} \tag{5}$$

where α_p is the obstacle strength for oxide nano-particles (which may vary between 0.1 and 0.5 depending on particle type and degree of coherency, mean value 1/3), N_{p} is the number density of nanoparticles and d_{p} is the mean diameter according to Table 8.1.

Calculation of the yield stress according to Eqs. ((1) to ((5) and comparison with the measured yield stress indicated a strong overestimation with respect to the measured values. However, literature provided evidence for a Pythagorean superposition of forest and particle strengthening. Therefore we replaced Eq. ((1) with Eq. ((6):

$$\sigma_{\mathrm{y}} = \sigma_0 + \sigma_s + \sigma_g + \sqrt{{\sigma_d}^2 + {\sigma_p}^2} \tag{6}$$

As shown in Figure 8.1a and b, Eq. (6) still gives rise to a significant overestimation of the measured values of the yield stress, in particular for the ODS alloys, and a trend of the residuals. It was then found that removal of both the friction stress and the solid-solution hardening component yield an almost perfect agreement between calculated and measured yield stress as shown in Figure 8.1c and d. This corresponds to a replacement of Eq. ((6) by Eq. ((7), which is the final result.

$$\sigma_{\mathrm{y}} = \sigma_g + \sqrt{{\sigma_d}^2 + {\sigma_p}^2} \tag{7}$$

Although there are some arguments in favor of the elimination of σ_0 and σ_s from Eq. (6) [11], the good fit does not provide sufficient evidence for Eq. ((7) to be 100% sound from the mechanistic point of view. Indeed, a similar quality of fit can probably be achieved by slightly reducing some of the factors of proportionality in Eqs. ((3) to ((5) combined with a less than 100% reduction of σ_0 and σ_s.

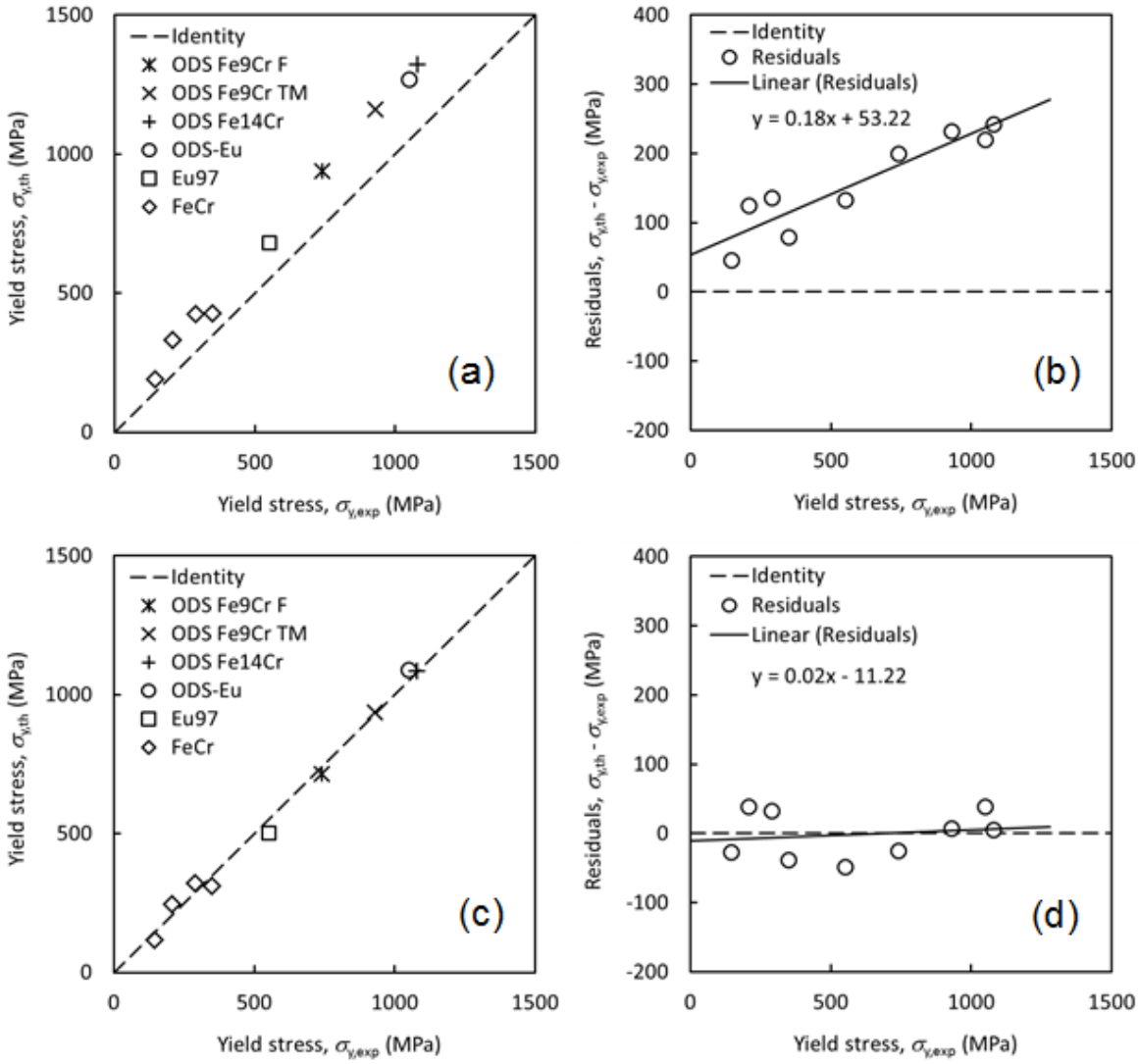

Figure 8.1: (a) Yield stress calculated according to Eq. 6 versus experimental yield stress, (b) residuals versus experimental yield stress, (c) Yield stress calculated according to Eq. 7 versus experimental yield stress, (d) residuals versus experimental yield stress for the studied alloys.

8.3 Effect of thermal ageing treatments

8.3.1 Ageing treatment at 475 °C/1000 h

The effect of the 475 ºC/1.000 h thermal ageing on the small punch parameter for the 14Cr ODS bars seems to be dependent on the specimen orientation, see Figure 8.2. For the T-oriented samples, the effect is more pronounced with an increase of load (F_m), but accompanied by and increase on small punch energy. This increase of ductility (increase of SP energy) does not correspond to the expected embrittlement phenomena associated to the decomposition into the Fe-rich α phase and the Cr-rich α' due to this thermal ageing. On the other hand for the L-oriented specimens, no effect can be observed. The fracture plane of the T-oriented specimens corresponds to the elongated grain direction, which can create more scatter and results more difficult to analyse.

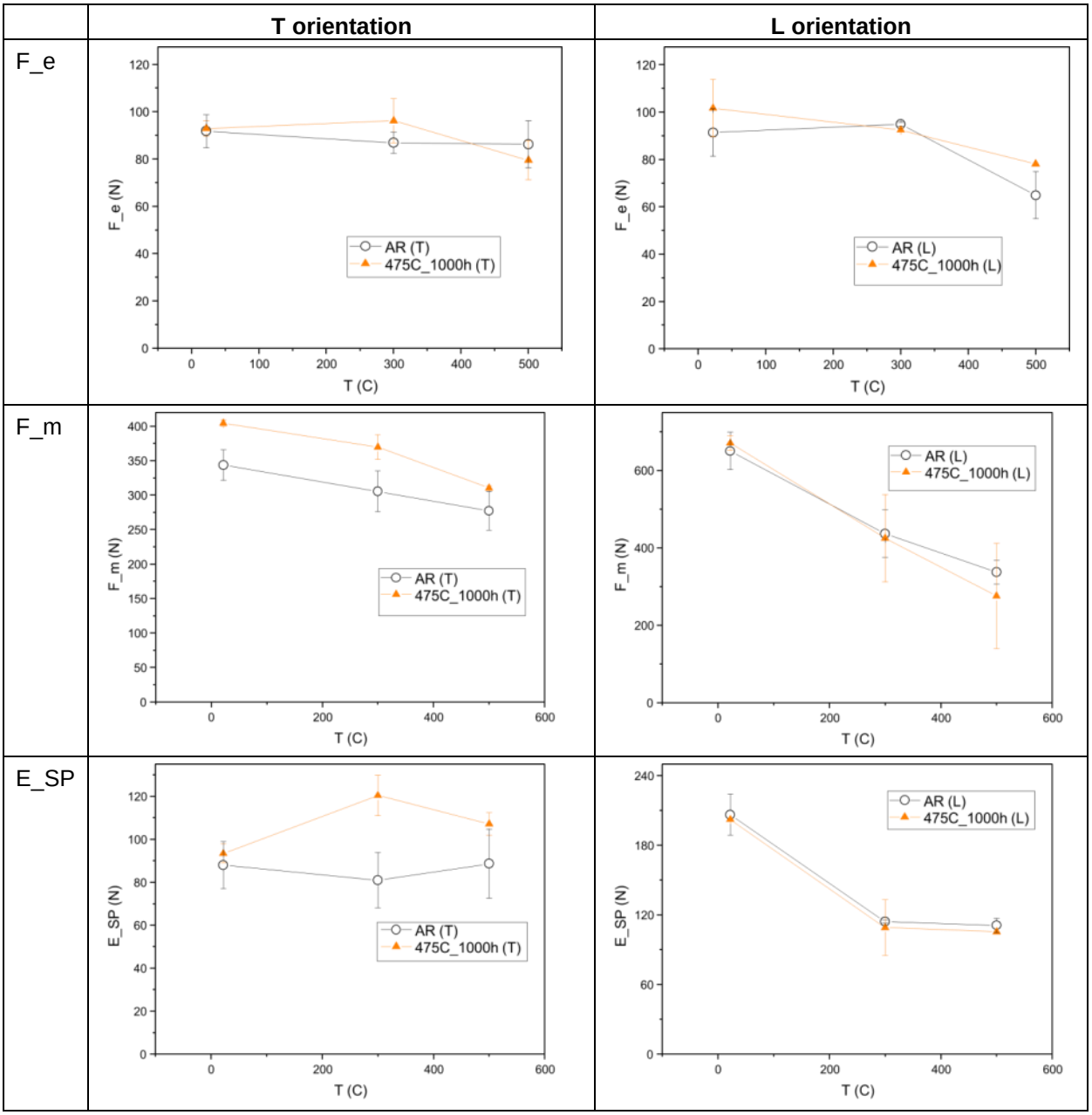

Figure 8.2: Effect of 475 °C/1.000 h thermal ageing on the 14Cr ODS bar small punch parameters.

For the 9Cr ODS bar, no effect of 475 ºC/1.000 h ageing treatment is observed, neither on the T- or L-oriented specimens, see Figure 8.3. This result was expected taking into account that the anisotropy in this bar is weak and that the Cr content is low to enhance α- α' decomposition.

A detailed consideration of the latest Fe-Cr binary equilibrium phase diagram (see Figure 1.1) shows that the minimum Cr content required for α- α' decomposition at a temperature of 475 °C is 14.9 wt%. Therefore, the phase diagram predicts that 475 °C embrittlement should not occur in ODS Fe14Cr bar containing 13.5 wt% Cr. This is what was observed in the performed small punch tests. The results are a nice confirmation of the expectation from the binary phase diagram for a complex alloy.

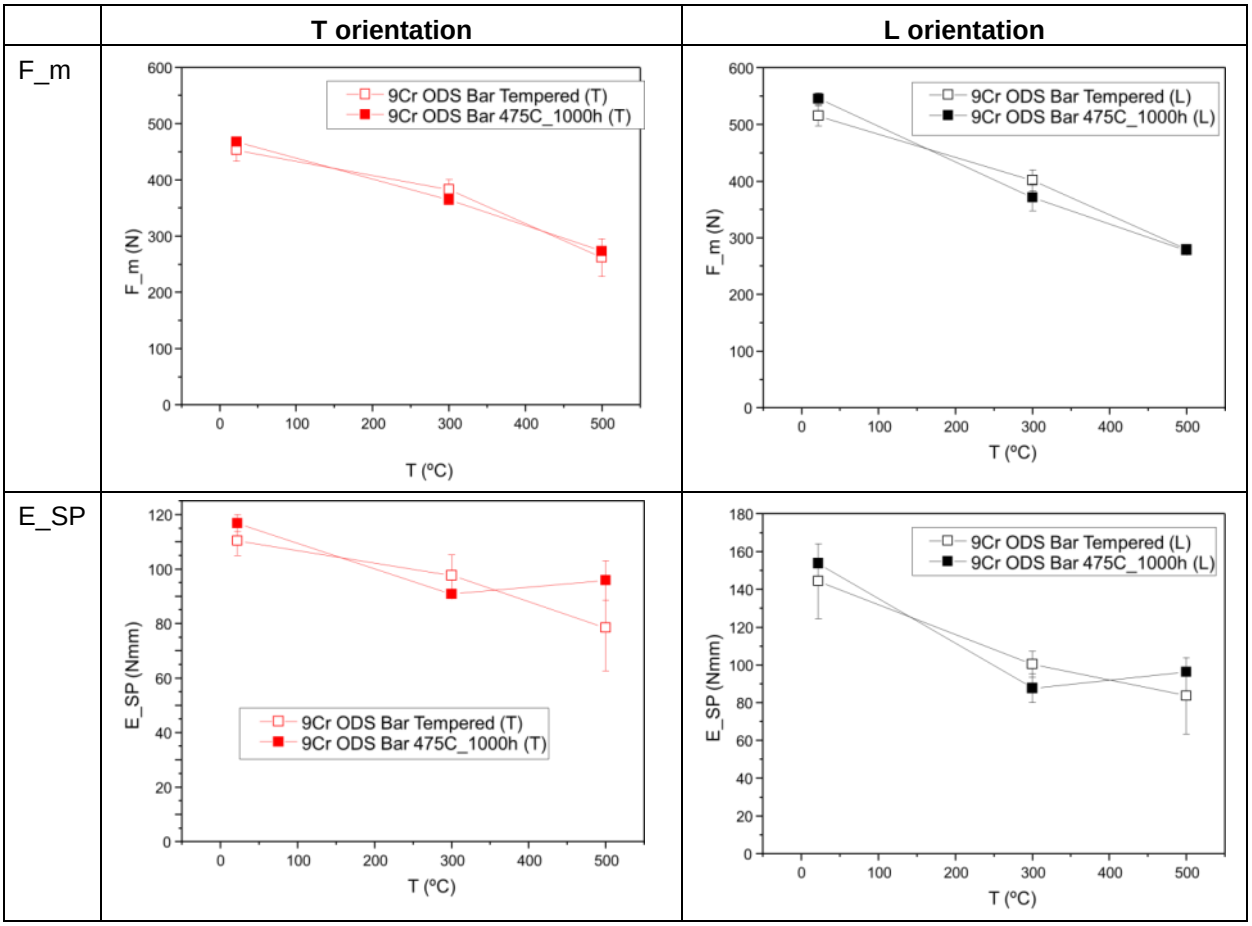

Figure 8.3: Effect of 475 °C/1.000 h thermal ageing on the 9Cr ODS bar small punch parameters.

8.3.2 Microstructure stability and softening under thermal conditions relevant for operation

Two long term ageing treatment were performed at 700 ºC/10.000 h and 800 ºC/10.000 h for both 9Cr ODS and 14Cr ODS bars. The effect of both ageing treatments on small punch parameter can be seen in Figure 8.4 for the 14Cr ODS bar and in Figure 8.5 for the 9Cr ODS bar.

For the 14Cr ODS bar, the effect is, as for the 475 ºC/1.000 h treatment, dependent on the specimen orientation. For the T-oriented specimens, the scatter is significant and the long term treatments induce a slight hardening (increase of F_m) and no effect on ductility, except for the tests at 300 ºC were both treatments induce an increase of ductility. On the other hand, for the L-oriented specimens after the long term treatment for the room temperature tests, show an decrease of strength or softening with a decrease of ductility, this results are in accordance to the tensile results of L-oriented specimens. For all the cases, the tests performed at 500 ºC do not show any evidence of the effect of long term ageing.

The effect of the long term ageing is more evident on the L-oriented specimens for the 9Cr ODS bar, showing the thermal aged specimens a decrease of strength and ductility. For the T-oriented specimens no clear effect can be seen.

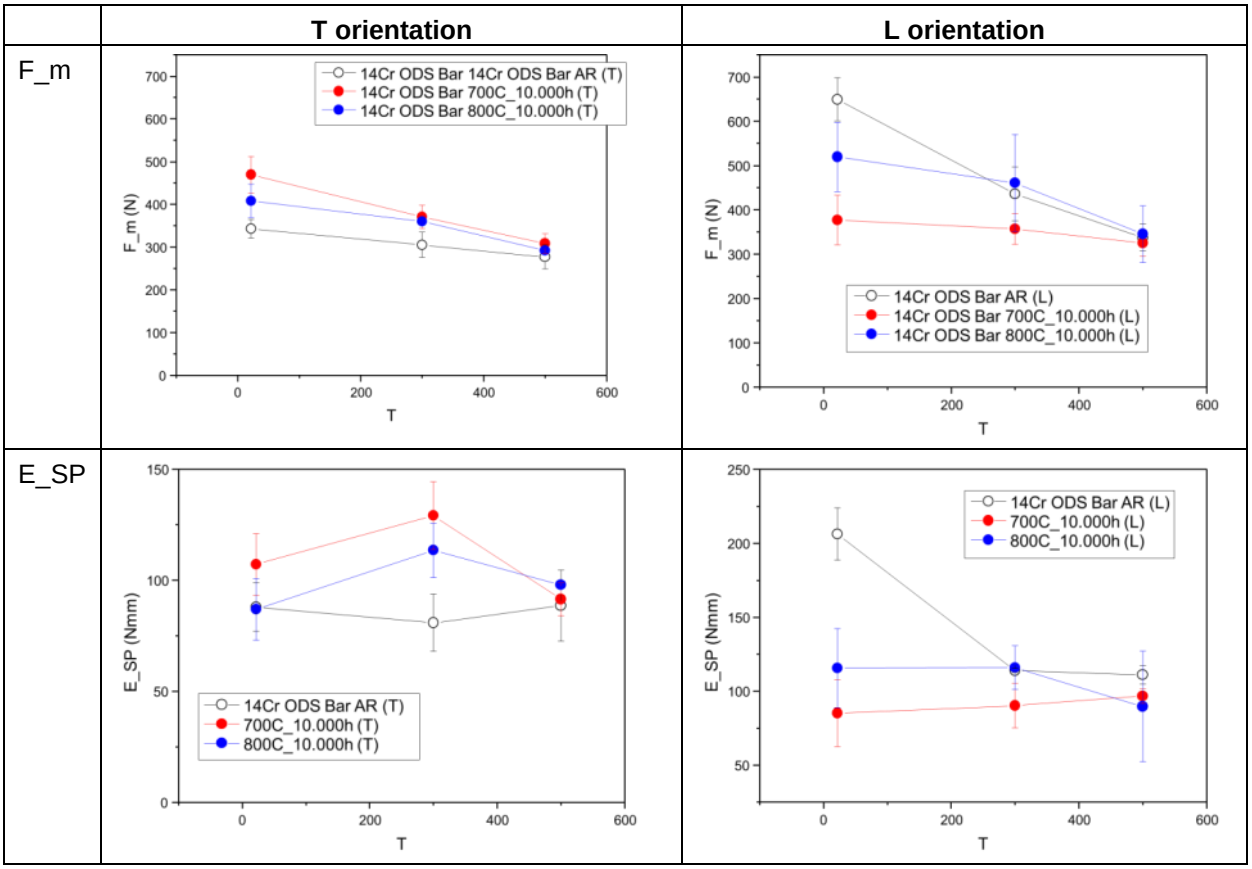

Figure 8.4: Effect of long term thermal ageing on the 14Cr ODS bar small punch parameters.

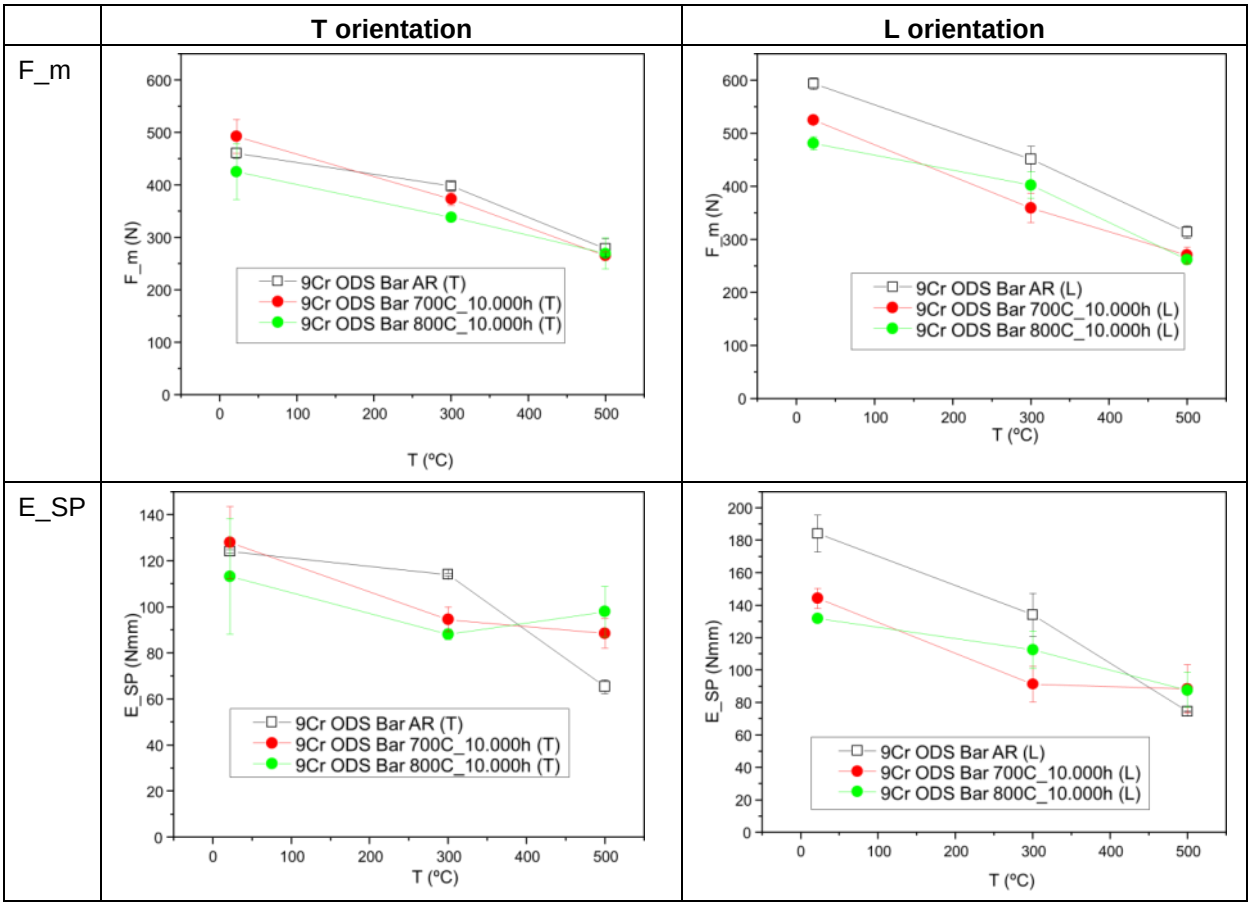

Figure 8.5: Effect of long term thermal ageing on the 9Cr ODS bar small punch parameters.

8.3.3 Microstructure stability after high-temperature short-term treatments

Materials performed differently for the ageing temperatures and times. The performance is strongly dependent on the fabrication route. While the microstructure after HIP+hot-rolling or hot-extrusion may look similar, the materials behaviour is completely different.

Although produced in different laboratories (KIT and CEA), the extruded materials (MAT-2, MAT-3) showed a similar performance. At 900 °C, the microstructure remained stable and the hardness was mostly unaffected. The grain orientation spread and grain size distribution charts also underpin this hypothesis. However, the hardness increase after 500 h at 1100 °C cannot be explained with the given data. Microstructural evidence could not be found. This would indicate that a change in the morphology and distribution of the oxide particles would have cause the drop in hardness. Additional TEM experiments may clarify this subject.

It is clear that in the case of MAT-4 the temperature of 900 °C and above was too high and caused a phase transition in the material. The ageing was performed within the gamma-regime and the material formed a ferritic structure at the end of the experiment during the cooling. Martensite was not found, because all the specimens were left to cool within the vacuum glass tubes and not quenched. The cooling rate was below the critical rate for martensite formation.

8.4 Effect of ion irradiation

8.4.1 Impact of irradiation temperature on hardening

Figure 7.3(b) to (f) show that a common feature of all materials irradiated at 500 ºC is a decrease of indentation hardness at decreasing indention depth in the near-surface region. This indicates an important role of the sample surface in the evolution of irradiation-induced defects. A possible interpretation is the operation of the surface as defect sink in combination with either point defect diffusion or glide of dislocation loops to the surface. A similar surface effect is well known from TEM observations on samples irradiated as thin foils. Another possible explanation for the decrease of indentation hardness at decreasing indention depth in the near-surface region is related to the sequence of the three-step irradiations. Indeed, it is possible that a fraction of the irradiation-induced defects introduced during steps 1 and 2 of the irradiation (see Table 3.3) will recombine during steps 2 and 3, when the whole sample is again exposed to the irradiation temperature. The healing effect on the nanohardness would presumably be more pronounced for the irradiations at 500 ºC.

At higher indentation depths, where surface effects do not play a role, obviously two kinds of behavior as a function of irradiation temperature have to be distinguished. For the 9Cr-ODS alloys, we have found equal hardening for both temperatures within experimental error indicating similar distributions of irradiation-induced nanofeatures, although a coincidental compensation of different contributions cannot be excluded. In contrast, hardening observed for the 14Cr alloys irradiated at 500 ºC is significantly less compared to 300 ºC. This difference indicates dissimilar types or distributions of irradiation-induced nanofeatures. The counterparts, 300 ºC versus 500 ºC and 9Cr versus 14Cr, imply a special role of Cr-rich α'-phase particles according to the Fe-Cr phase diagram. The remaining part of this section aims to analyze this scenario.

Irradiation-enhanced α' formation was frequently reported in the literature [25]. According to the equilibrium Fe-Cr phase diagram [1], significant amounts of α' are expected to form in Fe-14Cr alloys at 300 ºC, but much less α' can form in Fe-9Cr alloys at 300 ºC and no α' can form at 500 ºC for both Cr contents. The equilibrium volume fraction of α' as a function of Cr at 300 ºC is summarized in Table 8.2. The formation of these volume fractions of α' gives rise to additional hardening, which can be roughly estimated on the basis of the dispersed-barrier hardening model, Eq. (8):

$$\Delta H_{\mathrm{IT},\alpha'} = \frac{\alpha}{\beta} MGb\sqrt{Nd} \tag{8}$$

Here, the obstacle strength, α, for α'-phase particles is assumed to be 0.015 according to [26], the conversion factor, β, between yield stress increase and indentation hardness increase is taken to be 0.44, M = 3 is the Taylor factor, G = 84 GPa is the shear modulus, b = 0.248 nm is the Burgers vector, d = 2 nm is

the mean diameter of α'-phase particle according to [26] and *N* is the number density of particles estimated from the equilibrium volume fraction assuming a monomodal distribution of spherical α'-phase particles.

Table 8.2: Calculated equilibrium fraction of α' (vol%) as a function of Cr at 300 ºC, hardening caused by α'-phase particles calculated according to Eq. (8) and measured hardening (reference depth 400 nm, taken from Figure 7.3) at 300 ºC in excess of 500 ºC.

Material	14Cr-non-ODS	14Cr-ODS	9Cr-ODS-A	9Cr-ODS-B	ODS-Eurofer
Cr (wt.%)	13.8	13.5	9.1	9.1	8.9
Equilibrium fraction of α' at 300 ºC (vol%)	6.8	6.5	1.3	1.3	1.1
$\Delta H_{IT,\alpha'}$ according to Eq.(1) (GPa) *	0.38	0.38	0.17	0.17	0.15
$\Delta H_{IT,300°C} - \Delta H_{IT,500°C}$, measured (GPa)	0.3	0.3	<0.03	0.1	0.1

* Solubility limits of Cr in α and Fe in α' are 8 wt.% and 2 wt.%, respectively, according to the Fe-Cr phase diagram reported in [1]. wt.% of α' calculated from lever rule and converted to vol% of α'.

The theoretical hardness increase due to α'-phase particles derived from Eq. (8) and the measured excess hardness at 300 ºC (compared to 500 ºC) are shown in Table 8.2. The measured hardness difference was taken at an indentation depth of 400 nm in order to avoid interference with surface effects observed for 500 ºC. At this indentation depth, the hardness values are already reduced due to the substrate effect, because the plastic zones of the indentations extend deeper into the bulk than the ion irradiations. The comparison of the estimated hardening due to α'-phase particles and the excess hardness measured at 300 ºC shows a trend telling that the higher the equilibrium fraction of α' and the higher the resulting theoretical α'-induced hardening, the more the hardness measured at 300 ºC exceeds the hardness measured at 500 ºC, a temperature for which α' cannot form.

This is another indication that the initially presumed role of α'-phase particles might indeed be applicable. However, this indication must not be overstressed. It is not clear if the complete amount of equilibrium α' may have formed after ion irradiation up to 10 dpa. In this context, it is important to note that:

- α' formation was indeed observed in Fe-Cr alloys neutron-irradiated at 300 ºC up to 0.6 dpa. These α'-phase particles contributed essentially to the hardening for Fe-12%Cr [26].
- Less evidence on α' formation seems to be available for neutron-irradiated ODS steels.
- No α' was recently reported for an Fe-12%Cr alloy ion-irradiated at 300 ºC up to 0.5 dpa [27]. This phenomenon was interpreted as a consequence of the injected interstitials [28].

The arguments listed above show that further investigations are needed in order to clarify the possible contribution of α'-phase particles to the hardening at 300 ºC observed in this study. On the other hand, α'-phase formation is strictly excluded at 500 ºC. This situation led us to focus on the 500 ºC irradiations in section 8.4.2.

8.4.2 Impact of the initial microstructure on hardening

The discussion of the irradiation-induced hardness changes shown in Figure 7.4b is performed on the basis of the microstructural parameters collected in Table 7.1. Generally speaking, there are two different aspects of irradiation hardening, which can be cast into the following questions:

(1) How do the glide obstacles of the initial microstructure and the irradiation-induced nanofeatures of different kinds superimpose to substantiate the hardness measured for the irradiated materials? This question was tackled for the less complex case of neutron-irradiated Fe-Cr alloys [26]. As compared to [26], SANS is not applicable to the ion-irradiated thin layers of the present case; TEM is in progress within the collaborative project, but it is difficult to quantify the distribution of irradiation-induced nanofeatures such as loops in ion-irradiated technical Fe-based alloys by means of TEM; APT of the present set of ion-irradiated ODS alloys has not been included in the project, but should be envisaged as complementary study. Thus, it is a future challenge to answer question (1).

(2) How does the initial microstructure enhance or impede the evolution of the irradiation-induced microstructure and thus give rise to higher or less amounts of irradiation hardening? This question is

tackled below within the concept of sink strength. The characteristics of the irradiation-induced nanofeatures (loops, defect-solute clusters) appear as implicit variables, the values of which remain unknown.

Sinks for irradiation-induced point defects play a particular role in the microstructure evolution during irradiation, as they reduce the concentration of point defects available for irradiation-enhanced solute atom diffusion. For the present set of alloys, three types of sinks are potentially operative: dislocations, particle-matrix interfaces, and grain boundaries [29]. The specific sink strengths of dislocations, particles and grain boundaries and the total sink strength, denoted by S_d, S_p, S_g and S_{total}, respectively, can be calculated according to Eqs. (9) to (12) [29].

$$S_{\mathrm{total}} = S_{\mathrm{d}} + S_{\mathrm{p}} + S_{\mathrm{g}} \tag{9}$$

$$S_{\mathrm{d}} = Z_{\mathrm{d}}\rho \tag{10}$$

Having checked that capture of defects by dislocations is essentially diffusion-controlled [29] for the present microstructures, a value of 1.2 was estimated for the dislocation capture efficiency Z_d according to the method described in [29]. As we are not interested in swelling here, the capture of vacancies and interstitials is not distinguished.

$$S_{\mathrm{p}} = 2\pi N_{\mathrm{p}} d_{\mathrm{p}} \tag{11}$$

Eq. (11) is applied here as an approximation. It is valid for incoherent particles. We assume that both coherent and incoherent oxide nanoparticles are present in the materials investigated here. Coherent particles differ from incoherent particles with respect to the fact that they operate as point defect traps rather than sinks. Trapped point defects do not lose their identity and may recombine at a later time [29].

$$S_{\mathrm{g}} = 6\sqrt{S_{\mathrm{total}}}/d_{\mathrm{g}} \tag{12}$$

Eq. (12) is derived for the case that $(S_{total})^{1/2} d_g >> 1$ [29]. Note that the sum of Eqs. (9) to (12) constitute an implicit equation for S_{total}. The calculated values of the partial and total sink strengths are summarized in Table 8.3: Calculated sink strength and indentation hardness increase measured at a reference depth of 200 nm. As the first observation, the 14Cr alloys exhibit smaller hardening than each of the 9Cr alloys for both irradiation temperatures. On the one hand, this observation cannot be due to a possible contribution of α' to hardening (if any), because $\Delta H_{IT,\alpha'}$ is too small and follows the opposite trend, see Table 8.3. On the other hand, the observation is consistent with the larger total sink strengths calculated for the 14Cr alloys. As Table 8.3 shows, particles contribute most to the total sink strength followed by grain boundaries and dislocations. With the exception of S_d for ODS-Eurofer, the individual contributions are larger for the 14Cr alloys than for the 9Cr alloys.

Table 8.3: Calculated sink strength and indentation hardness increase measured at a reference depth of 200 nm.

Material	14Cr-non-ODS	14Cr-ODS	9Cr-ODS-A	9Cr-ODS-B	ODS-Eurofer
Sink strength of GBs, S_g (10^{14} m^{-2})	7.9	12.3	2.7	4.9	5.3
Sink strength of particles, S_p (10^{14} m^{-2})	46.2	63.6	27.0	27.0	27.5
Sink strength of dislocations, S_d (10^{14} m^{-2})	6.0	6.0	0.6	4.1	8.4
Total sink strength, S_{total} (10^{14} m^{-2})	60.1	81.9	30.3	36.1	41.1
ΔH_{IT} (300 ºC) (GPa)	0.58	0.69	1.22	0.96	1.02
ΔH_{IT} (500 ºC) (GPa)	0.31	0.26	1.15	0.74	0.61

As the second observation, 9Cr-ODS-B exhibits smaller hardening than 9Cr-ODS-A for both irradiation temperatures. The only difference between these two alloys is related to the heat treatments, which resulted in higher dislocation density and finer grains for 9Cr-ODS-B, but did not change the particle distribution. Therefore, the sink strength of particles S_p cannot be the reason of the smaller hardening of 9Cr-ODS-B. In other words, the smaller grain size and/or the higher dislocation density improve irradiation resistance, although they add only a minor part to the total sink strength.

In the above discussion, we have considered selected groups or pairs of materials in order to evaluate the effect of microstructure parameters. We have found that each of the sink types contributes to the irradiation resistance. A more detailed evaluation of the roles of the individual microstructure parameters is beyond the scope of the present study. However, it is interesting to analyze the irradiation-induced hardening as a function of total sink strength for the whole set of alloys as shown in Figure 8.6 for the irradiations at 500 ºC. The 300 ºC irradiations are placed back because of the unresolved situation for α'-phase particles. In Figure 8.6, we have introduced a power-law fit to the experimental data. The overall trend confirms the expectation that higher total sink strength gives rise to less hardening. We do not dispose of an analytical model predicting the amount of irradiation-induced hardening as a function of total sink strength. However, the fit curve represents an inverse relationship, which may serve as a rough empirical approximation for the materials and conditions of this study. Although the 300 ºC irradiations are excluded from Figure 8.6, it is interesting to note that Table 8.3 indicates a similar but weaker trend.

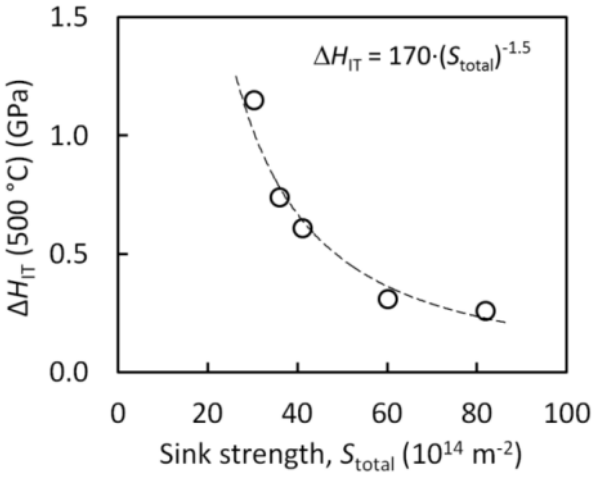

Figure 8.6: Irradiation-induced hardness change at 500 ºC as a function of total sink strength.

A similar analysis was performed in [30] on the basis of a broader range of sink strengths, namely from 10^{14} m^{-2} to 4×10^{16} m^{-2}. They observed a low-sink-strength domain, where hardening is independent of sink strength, and a high-sink-strength domain, where hardening strongly decreases. The range of sink strength investigated in the present study is close to the transition range between both domains.

8.4.3 TEM-based insight on the irradiation-induced nanofeatures

As shown in Section 7.2.2, TEM provided strong evidence of ion-irradiation-induced microstructural changes. These changes consist in the formation of irradiation-induced dislocation loops and networks of tangled dislocations, which are arranged in the form of bands. The evidence is based on the observed modulation of the microstructure as a function of the distance from the sample surface. Indeed, the bands of maximum density of loops and tangled dislocations, which are separated by regions of low densities of loops and dislocations, exhibit a pronounced correlation with the locations of the maxima of the displacement damage and the density of injected inter-stitials introduced as a result of the three-step self-ion irradiations. This correlation convincingly shows that the irradiation-induced microstructures in the bands are not just artefacts introduced as the result of the sample preparation using focussed ion beams.

The primary and secondary reasons for the observed formation of dislocation loops and tangled dislocations are tentatively concluded to be the injected interstitials and the displacement damage, respectively. The comparatively minor role of the displacement damage is indicated by the fact that the displacement damage shows a weak modulation with an amplitude of approximately 20%, whereas both loop/dislocation densities and injected interstitials are strongly modulated with amplitudes close to 100%. Moreover, it appears that the positions of maximum concentration of injected interstitials better coincide with the centre lines of the bands than the positions of maximum dpa. More work including modelling is required to derive quantitative relationships.

The presence of a fine dispersion of nano-oxides is also observed. They are better observed within the bands of low dislocation density, while their visibility is poorer at the bands with high density of other objects. It is reasonable to assume that the nano-oxides had been present in the alloys before irradiation. No indications of irradiation-induced changes of the size and number density of nano-oxides were obtained. This suggests stability of the nano-oxides against ion irradiation under the present conditions.

Finally, the TEM observations provide a rationalization of the observed irradiation-induced increase of the indentation hardness. Indeed, both dislocation loops and line dislocations represent obstacles for the glide of dislocations and, according to Section 8.2, contribute to hardening. It is important to point out that the type of performed nanoindentation experiments levels out the modulations of the microstructure. Therefore, the average densities of irradiation-induced loops and dislocations are expected to be responsible for the measured hardness increase. Future work is needed to derive quantitative relationships between irradiation-induced microstructures and hardening.

9 Summary and conclusion

A comprehensive and consistent description of the microstructures and mechanical properties of the ODS Fe9Cr and Fe14Cr alloys selected for the purposes of Task 4.1 of the MatISSE project was achieved by applying a combination of microstructure characterization techniques and mechanical testing. The collaborative study included the assessment of the initial microstructures and properties as well as the effects of different kinds of thermal treatments and ion irradiations.

The following main conclusions can be drawn from the investigation:

- A combination of microstructure characterization techniques based on EBSD, neutron diffraction, TEM, APT and SANS provided a consistent set of microstructure parameters of the initial micro-structures. This parameter set serves as reference to derive thermally induced and irradiation-induced microstructural changes and as basis to predict the mechanical properties.
- A microstructure-based equation was derived and calibrated using experimental data for an extended set of Fe-Cr-based alloys. The equation is capable of estimating the room-temperature yield stress of ODS Fe-Cr alloys including those selected within Task. 4.1.
- Small-punch tests indicated considerable anisotropy of the mechanical properties of the as-received and thermally treated ODS alloys.
- No evidence of thermally induced α-α' decomposition and possibly resulting 475°C embrittlement was obtained. This is in agreement with the latest binary Fe-Cr equilibrium phase diagram. Long-term medium temperature and short-term high-temperature thermal treatments provided additional evidence about the microstructure stability and their limits in terms of EBSD/grain size, hardness and small punch test parameters under the respective conditions. At 900 °C, the microstructure remained stable and the hardness was mostly unaffected.
- Ion-irradiation-induced changes of the microstructure and mechanical properties were observed by TEM and nanoindentation, respectively. TEM indicated a modulation of the density of loops and tangled dislocations as a function of depth from the surface, which correlates with the locations of the maxima of the displacement damage and the injected interstitials. Nanoindentation shows an inverse relationship between initial sink strength and irradiation resistance in terms of hardening.

Supplementary results obtained within Task 4.1 on the high-temperature low cycle fatigue (LCF) behavior of a tempered martensitic 9Cr-ODS steel bar and on mechanical properties derived from small punch tests are presented in Annexes.

Fully reversed strain-controlled LCF tests on tempered martensitic ODS Fe9Cr were conducted in air at 550 °C and 650 °C for different strain amplitudes. Apart from the higher cyclic stress levels, the steel manifests complex cyclic softening which is significantly lower in comparison to that observed for similar non-ODS steels. This is due to the fact that highly stable nano-oxide particles act as persistent barriers for dislocation motion which as a consequence slows down the typical microstructural evolution realized in conventional non-ODS steels. Microstructural evolution at 550 °C incudes mainly dislocations rearrangement and/or annihilation which finally result in their reduced density. At 650 °C, microstructural evolution hastens and becomes prominent mainly in nano-oxides/carbides deficient regions. Here, in addition to the reduced dislocation density, partially eliminated original sub-grain structures, grain growth, $M_{23}C_6$ carbides coarsening and occasional Cr-W enriched Laves phase precipitation were evident. The microstructural modifications, concerning dislocation density and sub-grain structures, intensify also with increase in applied strain amplitude. Nevertheless, annealing at 650 °C for similar duration has no major influence on microstructure.

References

[1] G. Bonny, D. Terentyev, L. Malerba, New Contribution to the Thermodynamics of Fe-Cr Alloys as Base for Ferritic Steels, J. Phase Equilibria Diffus. 31 (2010) 439–444. doi:10.1007/s11669-010-9782-9.

[2] M. T. Hutchings, C. G. Windsor, in K. Sköld, D. L. Price (Eds.), Methods of Experimental Physics, vol 23-c, Neutron Scattering, Academic Press, 1987.

[3] H.-G. Brokmeier, W.M. Gan, C. Randau, M. Völler, J. Rebelo-Kornmeier, M. Hofmann, Texture analysis at neutron diffractometer STRESS-SPEC, Nucl. Instrum. Methods Phys. Res. Sect. Accel. Spectrometers Detect. Assoc. Equip. 642 (2011) 87–92. doi:10.1016/j.nima.2011.04.008.

[4] H.-J. Bunge, Mathematische Methoden der Texturanalyse, Akademie-Verlag, Berlin, 1969.

[5] NN, (n.d.). http://www.mlz-garching.de/stress-spec.

[6] U. Keiderling, A. Wiedenmann, New SANS instrument at the BER II reactor in Berlin, Germany, Phys. B Condens. Matter. 213-214 (1995) 895–897. doi:10.1016/0921-4526(95)00316-2.

[7] U. Keiderling, The new “BerSANS-PC” software for reduction and treatment of small angle neutron scattering data, Appl. Phys. Mater. Sci. Process. 74 (2002) s1455–s1457. doi:10.1007/s003390201561.

[8] A. Wagner, F. Bergner, A. Ulbricht, C.D. Dewhurst, Small-angle neutron scattering of low-Cu RPV steels neutron-irradiated at 255°C and post-irradiation annealed at 290°C, J. Nucl. Mater. 441 (2013) 487–492. doi:10.1016/j.jnucmat.2013.06.032.

[9] W. Lefebvre, Atom probe tomography: put theory into practice, Elsevier, Boston, MA, 2016.

[10] C. Hatzoglou, Quantification et correction des biais inhérents à l’analyse par sonde atomique tomographique des nanoparticules d’un acier ODS : Application à l’étude de leur formation et à leur comportement sous irradiation, Université de Rouen, 2015.

[11] A. Chauhan, F. Bergner, A. Etienne, J. Aktaa, Y. de Carlan, C. Heintze, D. Litvinov, M. Hernandez-Mayoral, E. Oñorbe, B. Radiguet, A. Ulbricht, Microstructure characterization and strengthening mechanisms of oxide dispersion strengthened (ODS) Fe-9%Cr and Fe-14%Cr extruded bars, J. Nucl. Mater. 495 (2017) 6–19. doi:10.1016/j.jnucmat.2017.07.060.

[12] A. Chauhan, D. Litvinov, Y. de Carlan, J. Aktaa, Study of the deformation and damage mechanisms of a 9Cr-ODS steel: Microstructure evolution and fracture characteristics, Mater. Sci. Eng. A. 658 (2016) 123–134. doi:10.1016/j.msea.2016.01.109.

[13] M. Serrano, M. Hernández-Mayoral, A. García-Junceda, Microstructural anisotropy effect on the mechanical properties of a 14Cr ODS steel, J. Nucl. Mater. 428 (2012) 103–109. doi:10.1016/j.jnucmat.2011.08.016.

[14] A. García-Junceda, M. Hernández-Mayoral, M. Serrano, Influence of the microstructure on the tensile and impact properties of a 14Cr ODS steel bar, Mater. Sci. Eng. A. 556 (2012) 696–703. doi:10.1016/j.msea.2012.07.051.

[15] M. Serrano, A. García-Junceda, R. Hernández, M.H. Mayoral, On anisotropy of ferritic ODS alloys, Mater. Sci. Technol. 30 (2014) 1664–1668. doi:10.1179/1743284714Y.0000000552.

[16] I. Hilger, F. Bergner, A. Ulbricht, A. Wagner, T. Weißgärber, B. Kieback, C. Heintze, C.D. Dewhurst, Investigation of spark plasma sintered oxide-dispersion strengthened steels by means of small-angle neutron scattering, J. Alloys Compd. 685 (2016) 927–935. doi:10.1016/j.jallcom.2016.06.238.

[17] N. Sallez, C. Hatzoglou, F. Delabrouille, D. Sornin, L. Chaffron, M. Blat-Yrieix, B. Radiguet, P. Pareige, P. Donnadieu, Y. Bréchet, Precipitates and boundaries interaction in ferritic ODS steels, J. Nucl. Mater. 472 (2016) 118–126. doi:10.1016/j.jnucmat.2016.01.021.

[18] C. Randau, U. Garbe, H.-G. Brokmeier, *StressTextureCalculator* : a software tool to extract texture, strain and microstructure information from area-detector measurements, J. Appl. Crystallogr. 44 (2011) 641–646. doi:10.1107/S0021889811012064.

[19] Z. Oksiuta, P. Hosemann, S.C. Vogel, N. Baluc, Microstructure examination of Fe–14Cr ODS ferritic steels produced through different processing routes, J. Nucl. Mater. 451 (2014) 320–327. doi:10.1016/j.jnucmat.2014.04.004.

[20] R. Coppola, J. Rodriguez-Carvajal, M. Wang, G. Zhang, Z. Zhou, High resolution neutron diffraction crystallographic investigation of Oxide Dispersion Strengthened steels of interest for fusion technology, J. Nucl. Mater. 455 (2014) 426–430. doi:10.1016/j.jnucmat.2014.07.015.

[21] D. Litvinov, A. Chauhan, J. Aktaa, Microstructural evolution of 9Cr-ODS steel during high temperature deformation, in: Eur. Microsc. Congr. 2016 Proc., Wiley-VCH Verlag GmbH & Co. KGaA, Weinheim, Germany, 2016: pp. 850–851. doi:10.1002/9783527808465.EMC2016.6095.

[22] B. Duan, C. Heintze, F. Bergner, A. Ulbricht, S. Akhmadaliev, E. Oñorbe, Y. de Carlan, T. Wang, The effect of the initial microstructure in terms of sink strength on the ion-irradiation-induced hardening of ODS alloys studied by nanoindentation, J. Nucl. Mater. 495 (2017) 118–127. doi:10.1016/j.jnucmat.2017.08.014.

[23] M. Praud, F. Mompiou, J. Malaplate, D. Caillard, J. Garnier, A. Steckmeyer, B. Fournier, Study of the deformation mechanisms in a Fe–14% Cr ODS alloy, J. Nucl. Mater. 428 (2012) 90–97. doi:10.1016/j.jnucmat.2011.10.046.

[24] I. Kuběna, J. Polák, T.P. Plocinski, C. Hébert, V. Škorík, T. Kruml, Microstructural stability of ODS steels in cyclic loading: MICROSTRUCTURAL STABILITY OF ODS STEELS IN CYCLIC LOADING, Fatigue Fract. Eng. Mater. Struct. 38 (2015) 936–947. doi:10.1111/ffe.12284.

[25] M.. Mathon, Y. de Carlan, G. Geoffroy, X. Averty, A. Alamo, C.. de Novion, A SANS investigation of the irradiation-enhanced α–α′ phases separation in 7–12 Cr martensitic steels, J. Nucl. Mater. 312 (2003) 236–248. doi:10.1016/S0022-3115(02)01630-6.

[26] F. Bergner, C. Pareige, M. Hernandez-Mayoral, L. Malerba, C. Heintze, Application of a three-feature dispersed-barrier hardening model to neutron-irradiated Fe-Cr model alloys, J. Nucl. Mater. 448 (2014) 96–102. doi:10.1016/j.jnucmat.2014.01.024.

[27] C. Pareige, V. Kuksenko, P. Pareige, Behaviour of P, Si, Ni impurities and Cr in self ion irradiated Fe–Cr alloys – Comparison to neutron irradiation, J. Nucl. Mater. 456 (2015) 471–476. doi:10.1016/j.jnucmat.2014.10.024.

[28] O. Tissot, C. Pareige, E. Meslin, B. Decamps, J. Henry, Kinetics of α′ precipitation in an electron-irradiated Fe15Cr alloy, Scr. Mater. 122 (2016) 31–35. doi:10.1016/j.scriptamat.2016.05.021.

[29] G.S. Was, Fundamentals of radiation materials science: metals and alloys, Springer, Berlin ; New York, 2007.

[30] S.J. Zinkle, L.L. Snead, Designing Radiation Resistance in Materials for Fusion Energy, Annu. Rev. Mater. Res. 44 (2014) 241–267. doi:10.1146/annurev-matsci-070813-113627.

10 Annexes

10.1 Annex A: High-temperature LCF behavior of a tempered martensitic 9Cr-ODS steel bar

Ankur Chauhan, Jarir Aktaa
Institute for Applied Materials-Solid and Biomechanics (IAM-WBM), Karlsruhe Institute of Technology (KIT),
Hermann-von-Helmholtz-Platz 1, 76344 Eggenstein Leopoldshafen, Germany

A1. Introduction

The report presents an overview on the contribution from KIT which includes high-temperature low cycle fatigue (LCF) behavior of the 9Cr-ODS steel bar. The other investigations on this material by KIT can be found in the following Refs. [1–5].

A2. Investigated material and KIT experiments

A2.1 Material

The 9Cr-ODS steel (designated herein as 9YWT-MATISSE) was developed and produced under the supervision of CEA, France within the framework of MATISSE. The pre-alloyed metal powder, obtained from Aubert & Duval, was mechanical alloyed with 0.25 wt.% Y_2O_3 in a dry-type attrition ball mill. The milling was performed by Plansee in a hydrogen atmosphere for 24 h. Thereafter, the powder was sealed in a soft steel can and hot extruded at around 1100°C. The air cooled bars, now in a ferritic state, were semi-finished in the form of cylinders with 30 mm length and 4.2 mm diameter. These cylinders were then austenized at 1050°C for 10 min, followed by quenching with helium gas where the cooling rate was carefully chosen (6 - 7 °C/s). Then, a tempering treatment was performed at 750°C for 20 min, which was followed by cooling in air. The chemical composition of the steel is shown in Table 1.

Table 1: Chemical composition (others in wt.%) of the 9YWT-MATISSE.

Element	**Cr**	**W**	**Ti**	**Si**	**Ni**	**Mn**	**C**	**Y_2O_3**	**Fe**
Amount	9.1	1.1	0.3	0.3	0.2	0.3	0.1	0.25	Bal.

A2.2 Experiments

For fatigue testing, a computer controlled MTS 810 servo hydraulic testing machine (with MTS flex test TM 40 controller), equipped with a radiative furnace and a high-temperature extensometer (gauge length is 7 mm), was used (see, Fig. 1). Due to the limited quantity of material, miniaturized specimen geometry, with a gauge diameter of 2 mm and a gauge length of 7.6 mm was used, at an overall length of 27 mm (see Fig. 1). To avoid the influence of surface quality on cyclic lifetime, specimens were axially polished. The average surface roughness (RA) is ~ 0.26 µm. The axial strain-controlled fatigue tests (nominal strain rate of 10^{-3} s^{-1}, triangular waveform, R = -1) were conducted in air at 550°C and 650°C for different strain amplitude values ranging from ± 0.4% to ± 0.9%. The temperature was controlled to within ± 2°C with a type S Pt-Pt10Rh thermocouple attached to the bottom shoulder of the specimens. Unless otherwise indicated, all stresses correspond to the true stresses.

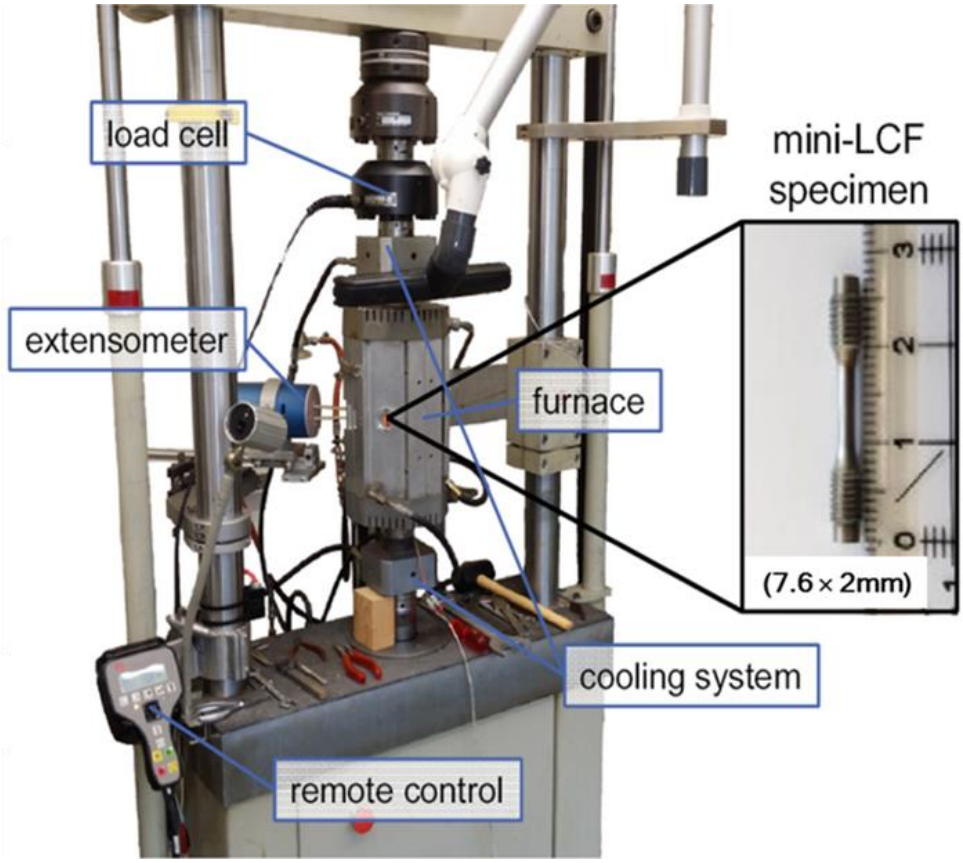

Fig. 1: MTS 810 servo hydraulic testing machine with used miniaturized LCF specimen.

Microstructural characterization was carried out in both undeformed as well as deformed state by electron backscatter diffraction (EBSD) and transmission electron microscopy (TEM). The samples from the deformed state were prepared by cutting longitudinal platelets using a Well 3242 diamond wire saw from the gauge section of the tested specimens. For EBSD, the longitudinally sectioned platelets were embedded, grinded, polished (last step: 1-micron diamond suspension) and etched using a solution consisting of 400 ml Ethanol, 50 ml HCL, 50 ml HNO3 and 6 g Picric acid. EBSD investigations were carried out using a Zeiss Merlin field-emission gun scanning electron microscope (SEM) with GEMINI II electron optics and an acceleration voltage of 20 keV. Kikuchi patterns were recorded with an EDAX Hikari high-speed EBSD camera and evaluated by the OIM Analysis 7.2.1 software. For scans, a step size of 70 nm was used. During post-processing, point with a confidence index (CI) lower than 0.1 were discarded. For the maps, a grain was defined as a region surrounded by high-angle boundaries (HABs) with misorientations higher than 15°. All maps are presented in a normal direction with respect to the sample surface.

For TEM samples, one or two discs were punched out from the remaining longitudinal platelets that were grinded to a thickness of ~ 100 µm. The discs were then thinned to electron transparency electrochemically using a Tenupol 5 Jet polisher. As an electrolyte, a mixture of sulfuric acid (20%) and absolute methanol (80%) was used at 23°C, 14–16 V and a flow rate of 38 (full scale 50). Finally, the electro-polished TEM samples were ion milled to obtain a clean surface. The TEM study was performed with a FEI TECNAI-20F (200 kV) TEM equipped with the high-angle annular dark-field (HAADF) detector for scanning TEM (STEM). The elemental analysis was performed using energy dispersive X-ray (EDX) spectroscopy.

A3. KIT results and discussion

A3.1 Low cycle fatigue (LCF) response

The stress response curves (tensile peak stress versus number of cycle curves) obtained at both temperatures under various applied strain amplitudes are shown in Fig. 2a. It is evident from the figure that at both temperatures 9YWT-MATISSE initially manifests transitional stages, i.e. cyclic hardening (increment

in peak stresses) and/or steep softening (reduction in peak stresses) corresponding to the small fraction of cyclic life, which is followed by a continuous linear cyclic softening stage that occupies the major fraction of cyclic life until failure. Except two specimens, tested at 550°C with ± 0.7% and ± 0.9% strain amplitudes which exemplify pure softening behavior, all specimens initially exhibit hardening. Here, the share of hardening is increasing with decreasing strain amplitude, but decreasing with increase in testing temperature. In addition, it is seen that the rate of subsequent linear cyclic softening in respect to number of cycles decreases with decrease in imposed strain amplitude and increase in testing temperature. For 9YWT-MATISSE, more details in respect to the measured cyclic strength, induced inelastic strains, determined inelastic strain energies, lifetime and their corresponding correlations were reported elsewhere, see Ref. [3,4] .

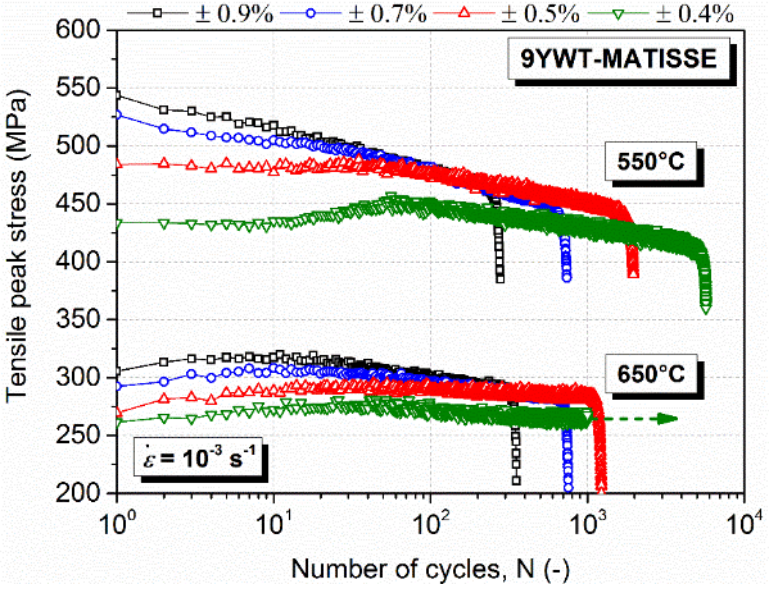

Fig. 2: Cyclic stress response curves of 9YWT-MATISSE at 550°C and 650°C under various applied strain amplitudes. Curve with arrow represent test condition where fatal crack nucleated outside probed gauge length.

Upon comparison with similar non-ODS F/M steels, e.g. EUROFER97 and P91 (Fig. 3[1]), 9YWT-MATISSE not only manifests higher cyclic strength and lower inelastic strain amplitude (half-width of the hysteresis loop at zero stress) but also exhibits significantly reduced cyclic softening [3]. Furthermore, ODS steel at 650°C manifests comparable cyclic strength and lifetime to tested non-ODS steel at 550°C (Fig. 3)

[1]Tests on the conventional non-ODS EUROFER97 [31] and non-ODS P91 [32] were performed on the same type of sample, using the same test set-up.

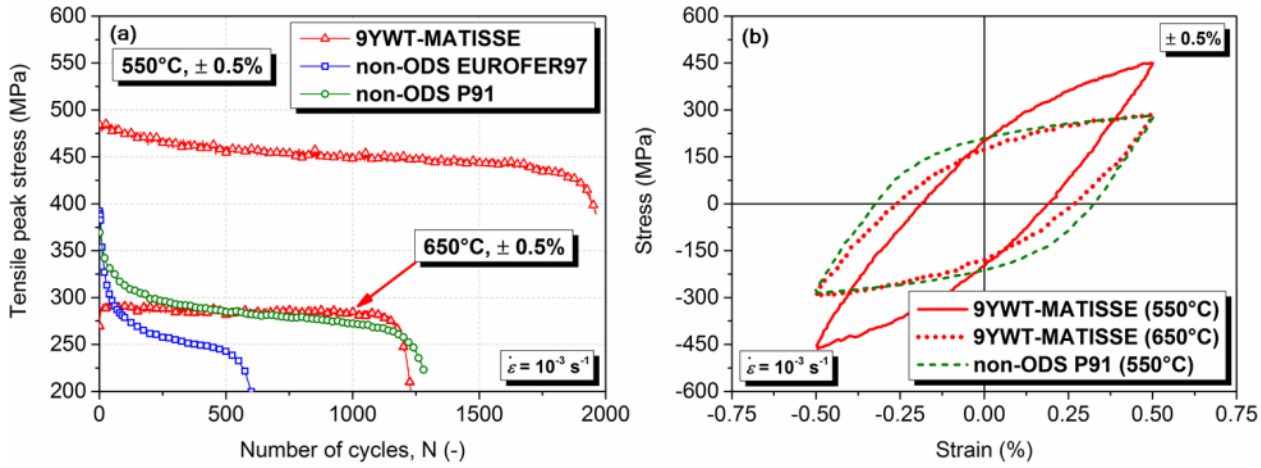

Fig. 3: (a) Comparison of the observed cyclic softening in 9YWT-MATISSE with that for non-ODS F/M steels (EUROFER97 and P91) and (b) corresponding hysteresis loops at half-life (N_f/2) under ± 0.5% strain amplitude.

A3.2 Microstructure before cycling

Owing to the composition and heat treatments, the matrix manifests a typical isotropic sub-micron tempered martensitic structure (Fig. 4a). The prior austenitic grains are subdivided into packets of laths and sub-grains having high density of dense and disordered dislocation tangles (see inset in Fig. 4a). Inverse pole figure (IPF) map (Fig. 4b) shows that the misorientation between laths and sub-grains is less than 15° (i.e. they manifest low-angle boundaries (LABs)) with dominance below 5°. The average grain size measured via EBSD is 0.58 µm. Additionally, irregular Cr-W enriched face centered cubic (FCC) $M_{23}C_6$ carbides, 103 ± 53 nm in diameter, and Ti-enriched particles, up to 200 nm in diameter, decorate different boundaries. However, majority is of the complex Y-Ti-O nanoparticles that are inhomogeneously distributed (Fig. 4c). Nevertheless, regions with homogeneous particle distribution were also observed, mostly within the grains, which have a size distribution ranging from 2 to 25 nm. High resolution TEM (HRTEM) reveals a FCC $Y_2Ti_2O_7$ crystal structure for the examined particles. One such particle lattice along with its corresponding inverted contrast fast Fourier transformation (FFT) diffractogram is shown in Fig. 4d. For more details, see Ref. [2].

A3.3 Microstructure after cycling

EBSD investigations after cycling straining at both temperatures reveal no obvious overall texture evolution, i.e. grains still manifest random orientations with no preferentiality (compare IPF maps shown in Fig. 5a-d). In addition, at 550°C, the average grain size as well as LABs and HABs fractions are only slightly altered (Fig. 6 and Table 2). Nonetheless, with an apparent trend, the evolution becomes conspicuous at 650°C. In Fig. 5c, the grains appear equiaxed with a prominent increment in their average size (Fig. 6 and Table 2); i.e. ~ 57% larger than in the undeformed state. This however appears independent of the applied strain amplitude. Futhermore, as shown in Fig. 6, the fraction of LABs decrease with a simultaneous increase in HABs fraction (Table 2). This suggests partial elimination of the original lath and sub-grain structures, since misorientation between them was measured to be less than 15°. This evolution amplifies with increase in applied strain amplitude. However, it is noteworthy that the remaining sub-grain boundaries (SGBs) or LABs are partly newly-formed due to the rearrangement (to and fro or shuttling motion) of mobile dislocations (see further).

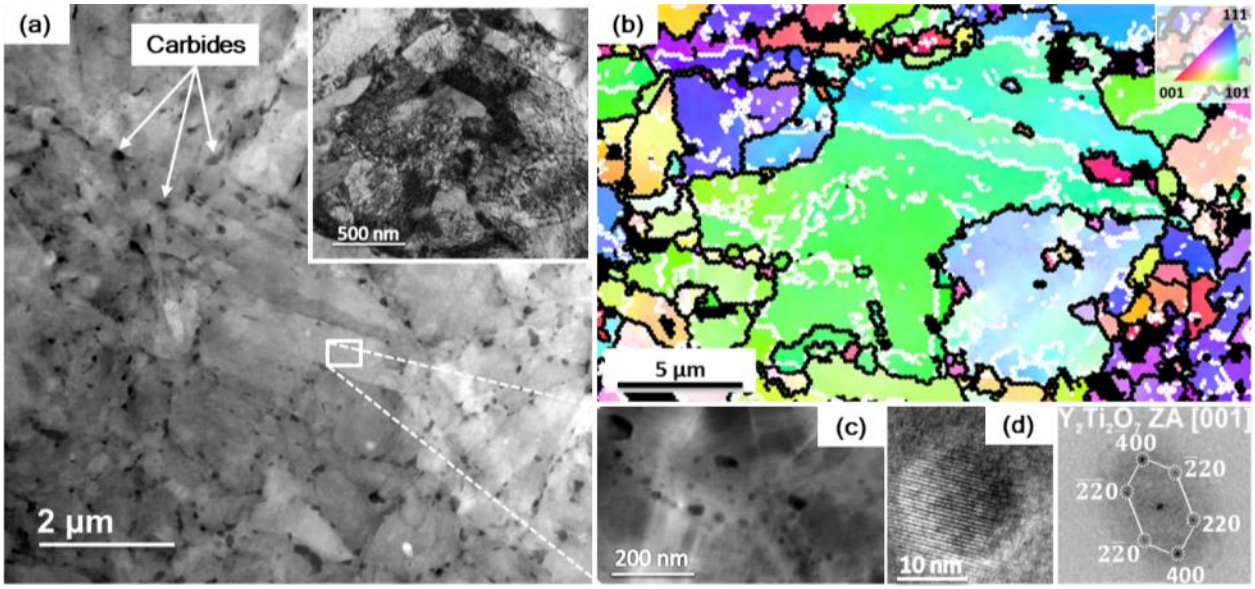

Fig. 4: Inverted contrast HAADF-STEM micrograph (a) from undeformed state reveals tempered martensitic structure with laths and sub-grains having carbides at various boundaries, inset shows dense and disordered dislocation tangles; IPF map (b) shows lath and sub-grain boundaries, LABs (<15°) in white while other HABs (>15°) in black. HAADF-STEM micrograph (c) reveals complex Y-Ti-O nanoparticles; HRTEM micrograph (d) with its inverted contrast FFT diffractogram revealing a FCC $Y_2Ti_2O_7$ lattice near to [001] zone axis.

Kernel average misorientation (KAM) and grain average misorientation (GAM) are used to visualize local misorientation changes. While KAM provides a good measure of dislocation density, GAM is a typical way of displaying orientation changes inside grains. In both cases, misorientation can be envisaged either in form of a color-coded map or as a graph. For more details about analyzing procedure, see Ref. [4]. As shown in Fig. 5e and i, both KAM and GAM maps for an undeformed state exhibit a homogeneous spread of relatively high values (Fig. 7). Here, prior one (Fig. 5e) implies a presence of high dislocation density, while later one (Fig. 5i) indicates the existence of sub-grain structures. After cycling, KAM spread reduces with a coexisting peak shift towards lower values (Fig. 7a). This can be partly seen with an appearance of blue color (depicting low misorientation values) in KAM map (Fig. 5f) indicating a reduction in dislocation density. This exaggerates even further with increase in both temperature and applied strain amplitude (Fig. 5g-h and Fig. 7a). Moreover, apart from nearly unaltered misorientation spread at 550°C, GAM shows similar trends at 650°C as observed for KAM after cyclic straining (Fig. 5j-l and Fig. 7b). Here, the fraction of grains with low misorientation values increases with increase in both temperature and applied strain amplitude. Hence, it appears that due to the conjoint effect of temperature and cyclic straining, these grains either formed after dynamic recrystallization and/or experienced original sub-grain structures elimination. However, recrystallization is not expected. Moreover, sub-grain structures elimination is also in accordance with reduction of LABs fraction (Table 2) which is also confirmed by TEM investigations (see further).

Therefore, from the local misorientation analysis, it can be concluded that cyclic straining results mainly in a reduction of dislocation density at 550°C and with additional partial sub-grain structure elimination at 650°C which intensify even further with increase in applied strain amplitude.

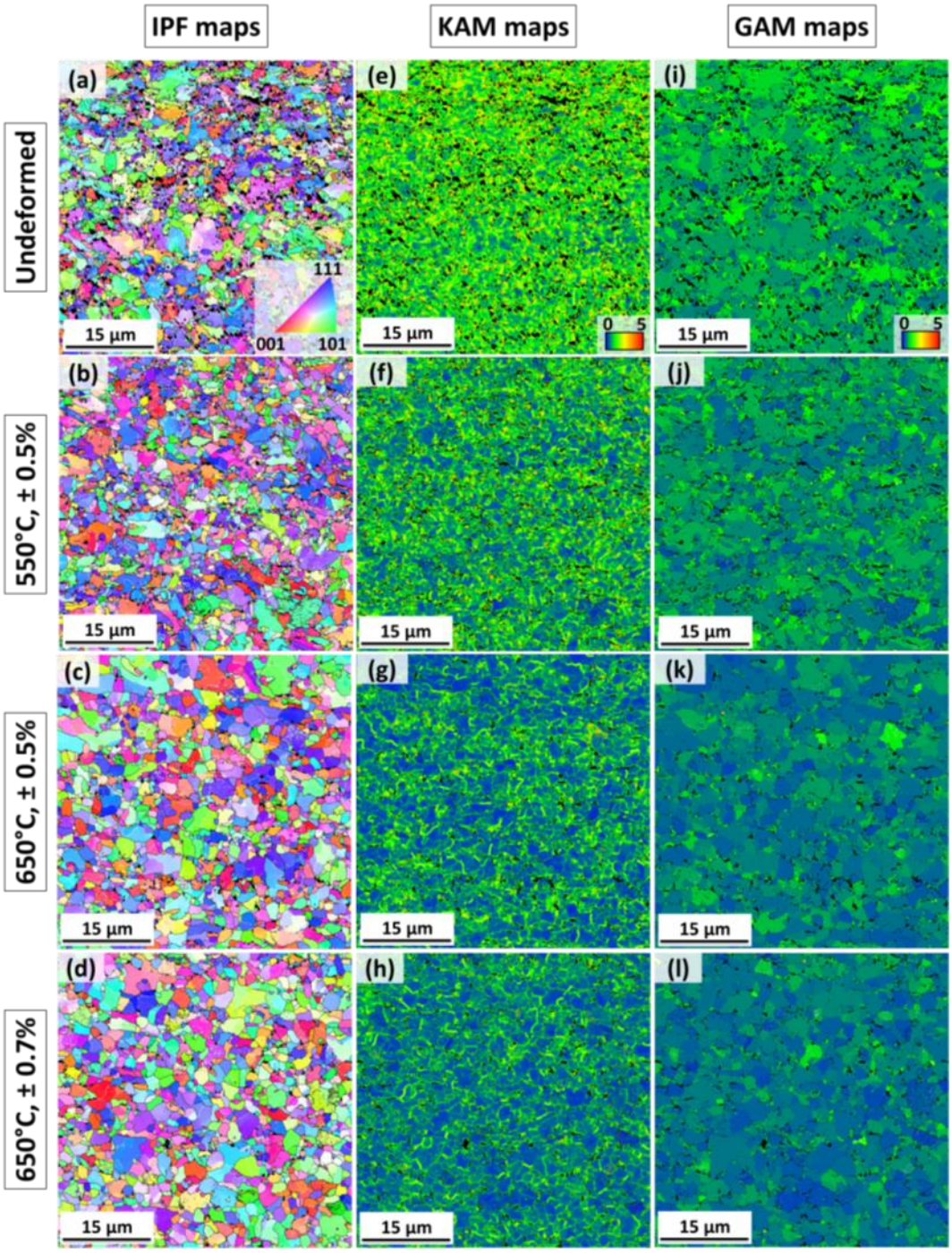

Fig. 5: IPF (a-d), KAM (e-h) and GAM (i-l) maps obtained by analyzing EBSD scans that were taken before (undeformed) and after cyclic straining (550°C, ± 0.5%; 650°C, ± 0.5% and 650°C, ± 0.7%). Color keys are provided for each type of maps.

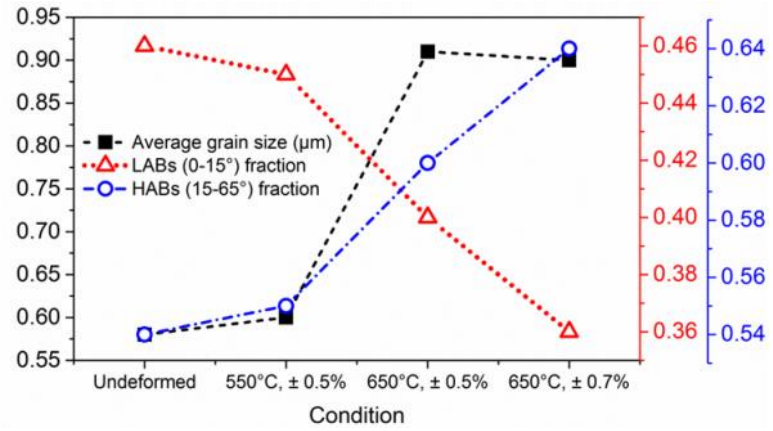

Fig. 6: Graph showing average grain size as well as LABs and HABs fractions evolution upon cycling at 550°C and 650°C for two strain amplitudes (± 0.5% and ± 0.7%) via EBSD.

Table 2: Average grain size as well as LABs and HABs fractions measured before (undeformed) and after cyclic straining (550°C, ± 0.5%; 650°C, ± 0.5% and 650°C, ± 0.7%) via EBSD.

Condition	Average grain size (μm)	LABs (0-15°) fraction	HABs (15-65°) fraction
undeformed	0.58	0.46	0.54
550°C, ± 0.5%	0.60	0.45	0.55
650°C, ± 0.5%	0.91	0.40	0.60
650°C, ± 0.7%	0.90	0.36	0.64

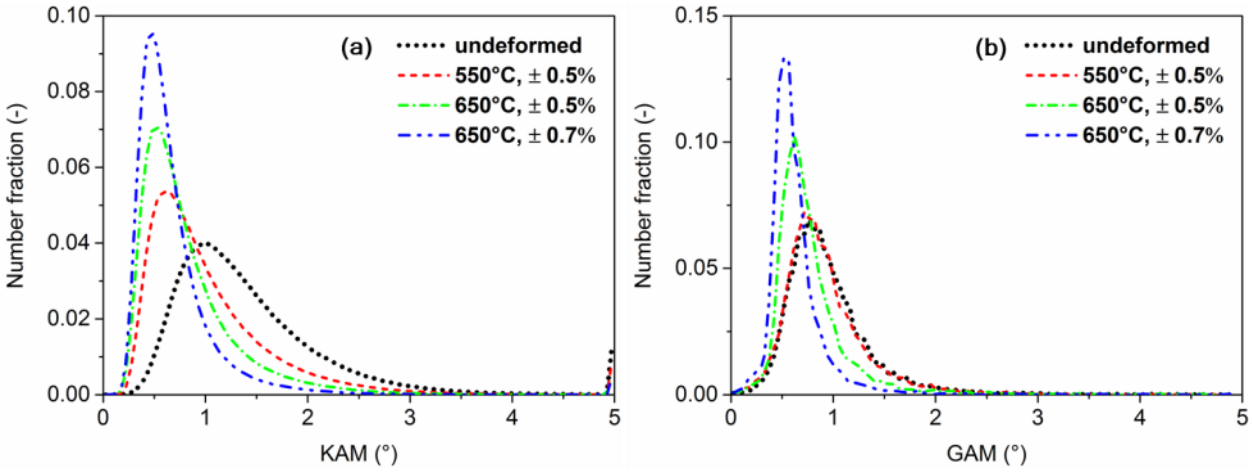

Fig. 7: KAM (a) and GAM (b) values distributions before (undeformed) and after cyclic straining (550°C, ± 0.5%; 650°C, ± 0.5% and 650°C, ± 0.7%).

In order to understand microstructure evolution at even higher resolution, TEM investigations were carried out. As detailed microstructural evolution after cyclic straining was reported elsewhere [4], only brief summary is presented here. The overall microstructures after cyclic straining under ± 0.5% strain amplitude at 550°C and 650°C are shown in Fig. 8. In general, at both temperatures, grains appear equiaxed having sub-grain structures. Even though rarely, well defined lath structures are still perceived at 550°C (see, pointed features in Fig. 8a). Nevertheless, at 650°C, grains appear comparatively coarse and no lath structures could be distinguished (Fig. 8b). In addition, at both temperatures, regions of different dislocation

densities were observed. Here, areas with lower and higher dislocation densities correspond to those with low and high KAM values, respectively. This is likely to be a question of homogeneity of oxide particles distribution, i.e. their presence or absence in particular grain or even within a single grain (discussed later).

Nevertheless, in almost all grains individual dislocations appear pinned at the nanoparticle-matrix interfaces and under the effect of stresses, most of them are bowed out (Fig. 9a). Moreover, pinning is not only realized on the arrival side of the nano-oxide particles but also on their departure sides (marked in Fig. 9b). This suggests an attractive particle-dislocation interaction, since even after overcoming particles by cross-slip or climb (depending upon the character of the dislocations and the nature of the particle-matrix interface) dislocations are being pinned on the departure side of the nano-oxide particles [4]. Hence, there exists a threshold stress to detach dislocation out of this pinning, which must be overcome for the dislocation to glide; and therefore, plastic deformation to occur [6–9]. However, once threshold stress is reached, the dislocation will detach and glide until new pinning (see Fig. 9a, where remnant slip traces, formed as a result of dislocations glide, in between nanoparticles are apparent) where the process of particle by-pass and detachment recurs. This results in a retarded dislocation's intragranular mobility. However, in between obstacles or in particles deficient region, dislocations can still annihilate with those of opposite signs, leading to their reduced density. This leads to a moderately clean microstructure, as cleaner regions are mostly free of both nanoparticles as well as dislocations [4]. And therefore, it seems that due to their obstruction free path, since there are no particles to be pinned against, dislocations glide freely across whole grain. Hence, both uniform nanoparticles distribution as well as lower inter-particle spacing is critical for suppressing the annihilation processes. Furthermore, this dislocation glide can also acts as a driving force for sub-grain boundary (SGB) elimination (Fig. 10). According to Sauzay et al. [10], mobile dislocations annihilate with those of the opposite sign in LABs leading to the elimination of the corresponding lath and sub-grain boundaries. In addition, knitting-out reactions could also cause SGBs dissolution, for more see Refs. [4,11,12].

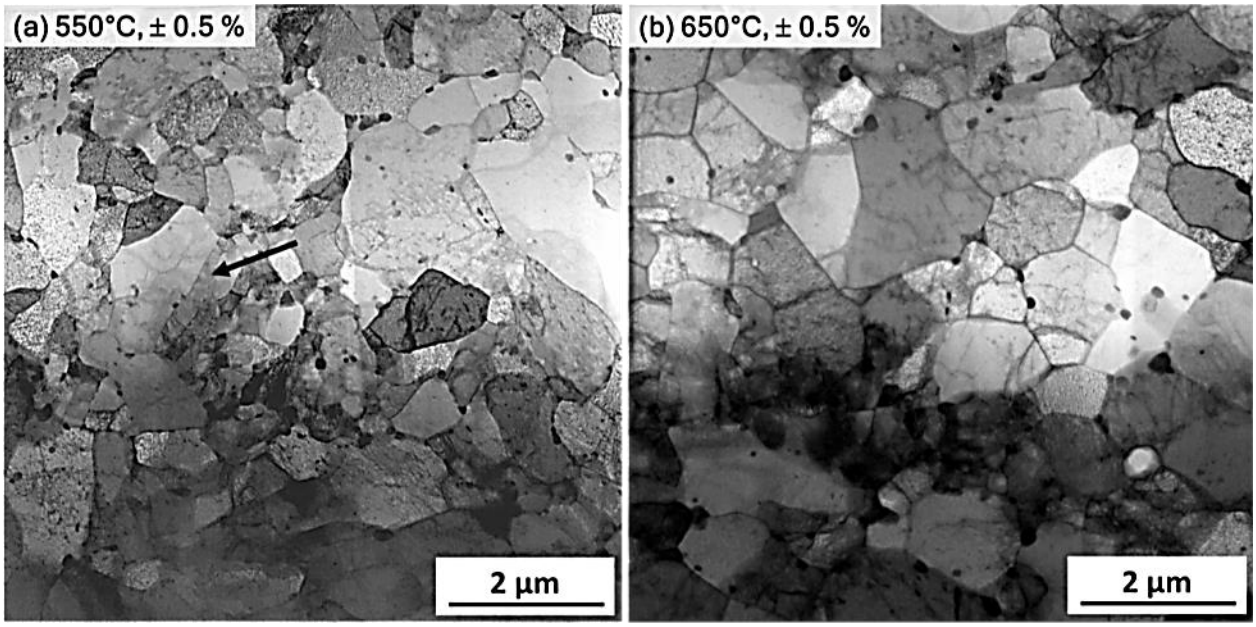

Fig. 8: Inverted contrast HAADF-STEM micrographs showing microstructures after testing under ± 0.5% strain amplitude at (a) 550°C and (b) 650°C.

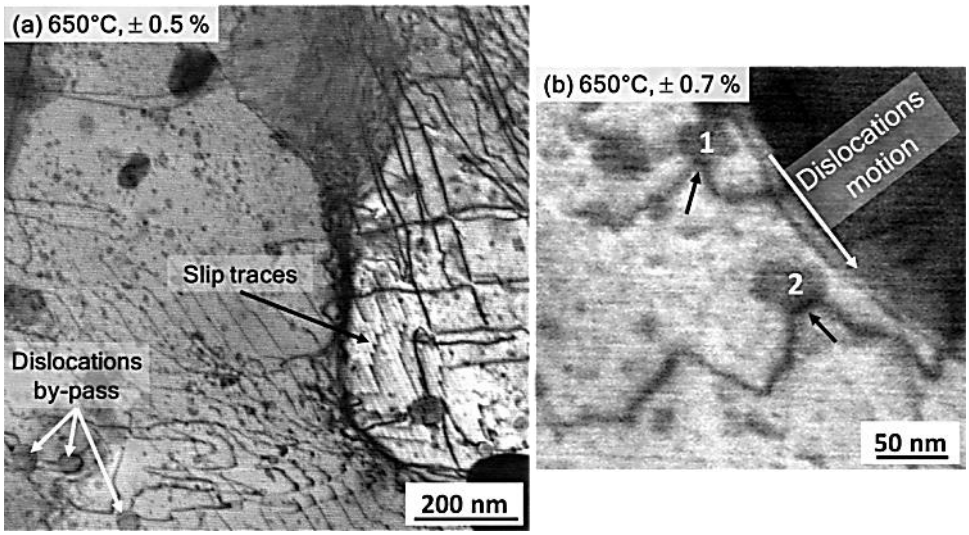

Fig. 9: Inverted contrast HAADF-STEM micrographs showing microstructures after testing at 650°C under (a) ± 0.5% and (b) ± 0.7% strain amplitudes.

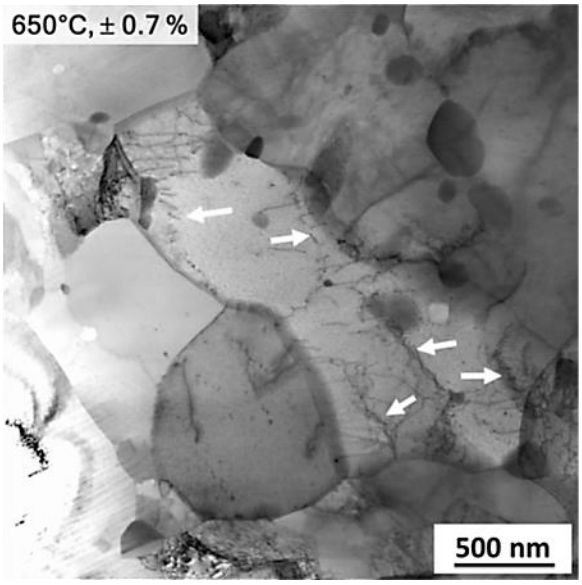

Fig. 10: Inverted contrast HAADF-STEM micrographs showing microstructures after testing at 650°C under ± 0.7% strain amplitude with marked partially eliminated sub-grain boundaries.

In respect to the present precipitates, carbides appear coarsened particularly after cycling at 650°C. This coarsening is especially seen for those which are still in contact with boundaries. The evident coarsening occurs through: (1) diffusion of alloying elements from matrix towards boundaries which additionally act as short-circuit diffusion networks; and (2) coalescence through Ostwald ripening mechanism. This coarsening altogether not only degrades one source of strength (i.e. solid solution strengthening) but can also compel carbides to lose their ability of pinning boundaries [13] which might explain observed grain coarsening that leads to equiaxed grains and also possible SGBs migration. Nonetheless, this can also be attributed to the localized pinning-sources (carbides or Y-Ti-O nanoparticles) free boundary-segments migration, which otherwise could have remained pinned, as shown in Fig. 11, due to Zener drag effect. Furthermore, EDX analysis (see [4]), reveals the presence of carbon free Cr-W enriched phase which is commonly referred to as Laves phase (WCr_2) [14,15]. Though seen seldom, the formation of Laves phase can be due to the presence of Si which reduces the solubility of W in the matrix [16] and their segregation on or near to the boundaries finally weaken the effect of solid solution strengthening [17]. However, considering the short durations of LCF tests, this effect can be neglected. As according to Klueh [18] for the short-time creep tests

(≤10,000 h), the W still contributes to the solid solution strengthening, even though Laves removes W from solution. Moreover, during early stages of such tests, the precipitation hardening by Laves phase contributes to the strength, which subsequently decreases as a result of coarsening of the Laves phase particles [14]. Besides, Y-Ti-O nanoparticles and carbides were not sheared by dislocations which otherwise could have contributed to the cyclic softening [19]. Shearing is possible only if particles are coherent with the matrix which was not observed for the dispersoids and the carbides, respectively. Finally, the Y-Ti-O nanoparticles appeared very stable without any change in shape or size.

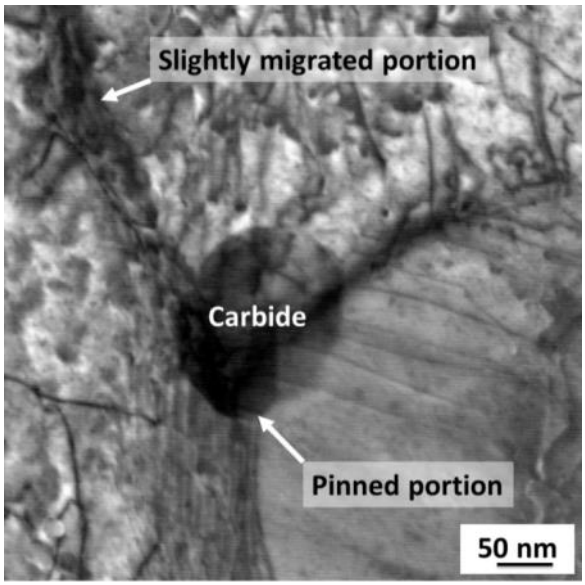

Fig. 11: Inverted contrast HAADF-STEM micrograph, taken from the specimen tested under ± 0.7% strain amplitude at 650°C, showing grain boundary portion pinned by carbide and slightly migrated portion without carbide.

Hence, from the TEM investigations it can be concluded that the minor linear cyclic softening observed in 9YWT-MATISSE is mainly due to the rearrangement and/or annihilation of dislocations at 550°C. Whereas, at 650°C, due to additional synergistic effect of partially eliminated original sub-grain structures, grain growth, and $M_{23}C_6$ carbides coarsening. It is also observed that the microstructural modifications, concerning dislocation density and sub-grain structures, intensified even further with increase in applied strain amplitude, for this see Ref. [4]. This is due to the fact that under such conditions larger inelastic strain has to be accommodated per cycle than under lower applied strain amplitude. And therefore, a higher degree of softening is observed with increase in applied strain amplitude.

A4. Conclusions

The fully reversed strain-controlled LCF tests conducted on tempered martensitic Fe-9%Cr-based ODS steel in air at 550°C and 650°C under different strain amplitude values led to the following conclusions:

1. Besides higher peak stresses and thus lower inelastic strain amplitudes, oxides dispersion assists in mitigating the undesirable cyclic softening observed in conventional F/M steels. This is due to fact that highly stable nano-sized oxide particles act as persistent barriers for dislocation motion which consequently reduce/slows-down the typical microstructural degradation. However, cyclic straining assisted by thermal activation as well as inhomogeneous nanoparticles distribution result in similar microstructural changes as those observed in non-ODS matrix steels, but to a lesser extent.
2. The studied ODS steel at 650°C manifests comparable cyclic strength and lifetime to tested non-ODS F/M steels at 550°C. Hence, concerning LCF, oxide dispersion raises the limited operating temperature of conventional non-ODS F/M steels by at least 100°C.
3. EBSD complemented by TEM investigations were performed to delineate microstructural evolution after cyclic straining. At 550°C, microstructure appears similar to that of the undeformed state. However, the main differences are in respect to the dislocations rearrangement and/or annihilation

which finally results in their reduced density. At 650°C, microstructural evolution hastens and becomes prominent mainly in nano-oxides/carbides deficient region. Here, in addition to the reduced dislocation density, partially eliminated original sub-grain structures, grain growth, $M_{23}C_6$ carbides coarsening and Cr-W enriched Laves phase precipitation were also evident. The microstructural modifications, concerning dislocation density and sub-grain structures, intensify even further with increase in applied strain amplitude. Nevertheless, annealing at 650°C for comparable testing duration causes no noticeable microstructural changes [4]. Since modest cyclic softening persists at both investigated temperatures, out of all microstructural changes the dislocations rearrangement and/or their mutual annihilation are assumed to be the main cause for the loss of cyclic strength.

A5. Acknowledgements

This work was carried out under the financial support of European atomic energy community (Euratom) 7th Framework Programme FP7-Fission-2013 for Research and Technological Development under the grant agreement no. 604862 (MatISSE project) and in the framework of the EERA (European Energy Research Alliance) Joint Programme on Nuclear Materials. Authors would like to gratefully acknowledge Dr. Dimitri Litvinov and Dr. Jan Hoffmann for their assistance in handling TEM and acquiring EBSD scans, respectively.

A6. References

[1] A. Chauhan, D. Litvinov, Y. de Carlan, J. Aktaa, Study of the deformation and damage mechanisms of a 9Cr-ODS steel: Microstructure evolution and fracture characteristics, Mater. Sci. Eng. A. 658 (2016) 123–134. doi:10.1016/j.msea.2016.01.109.

[2] A. Chauhan, F. Bergner, A. Etienne, J. Aktaa, Y. de Carlan, C. Heintze, et al., Microstructure characterization and strengthening mechanisms of oxide dispersion strengthened (ODS) Fe-9%Cr and Fe-14%Cr extruded bars, Submitt. to J. Nucl. Mater. (2017).

[3] A. Chauhan, M. Walter, J. Aktaa, Towards improved ODS steels: A comparative high-temperature low-cycle fatigue study, Fatigue Fract. Eng. Mater. Struct. (2017). doi:10.1111/ffe.12639.

[4] A. Chauhan, J. Hoffmann, D. Litvinov, J. Aktaa, High-temperature low-cycle fatigue behavior of a 9Cr-ODS steel: Part 1 - Pure fatigue, microstructure evolution and damage characteristics, Submitt. to Mater. Sci. Eng. A. (2017).

[5] A. Chauhan, J. Aktaa, High-temperature low-cycle fatigue behavior of a 9Cr-ODS steel: Part 2 - Hold time influence, microstructural evolution and damage characteristics, Submitt. to Mater. Sci. Eng. A. (2017).

[6] V.C. Nardone, J.K. Tien, Pinning of dislocations on the departure side of strengthening dispersoids, Scr. Metall. 17 (1983) 467–470.

[7] J.K. Tien, V.C. Nardone, D.E. Matejczyk, The threshold stress and departure side pinning of dislocations by dispersoids, Acta Metall. 32 (1984) 1509–1517.

[8] B. Reppich, On the attractive particle–dislocation interaction in dispersion-strengthened material, Acta Mater. 46 (1998) 61–67. doi:10.1016/S1359-6454(97)00234-6.

[9] E. Arzt, D.S. Wilkinson, Threshold stresses for dislocation climb over hard particles: The effect of an attractive interaction, Acta Metall. 34 (1986) 1893–1898. doi:10.1016/0001-6160(86)90247-6.

[10] M. Sauzay, H. Brillet, I. Monnet, M. Mottot, F. Barcelo, B. Fournier, et al., Cyclically induced softening due to low-angle boundary annihilation in a martensitic steel, Mater. Sci. Eng. A. 400–401 (2005) 241–244. doi:10.1016/j.msea.2005.02.092.

[11] W. Blum, Dislocation models of plastic deformation of metals at elevated temperatures, Zeitschrift Fuer Met. Res. Adv. Tech. 68 (1977) 482–492.

[12] G. Eggeler, The effect of long-term creep on particle coarsening in tempered martensite ferritic steels, Acta Metall. 37 (1989) 3225–3234. doi:10.1016/0001-6160(89)90194-6.

[13] A.F. Armas, C. Petersen, R. Schmitt, M. Avalos, I. Alvarez-Armas, Mechanical and microstructural behaviour of isothermally and thermally fatigued ferritic/martensitic steels, J. Nucl. Mater. 307–311 (2002) 509–513. doi:10.1016/S0022-3115(02)01086-3.

[14] R.L. Klueh, D.R. Harries, High-Chromium Ferritic and Martensitic Steels for Nuclear Applications, ASTM International, 100 Barr Harbor Drive, PO Box C700, West Conshohocken, PA 19428-2959, 2001. doi:10.1520/MONO3-EB.

[15] A. Chauhan, L. Straßberger, U. Führer, D. Litvinov, J. Aktaa, Creep-fatigue interaction in a bimodal 12Cr-ODS steel, Int. J. Fatigue. 102 (2017) 92–111. doi:10.1016/j.ijfatigue.2017.05.003.

[16] A. Chauhan, D. Litvinov, J. Aktaa, Deformation and damage mechanisms of a bimodal 12Cr-ODS steel under high-temperature cyclic loading, Int. J. Fatigue. 93 (2016) 1–17. doi:10.1016/j.ijfatigue.2016.08.003.

[17] M. Sauzay, Mechanical behavior of structural materials for Generation IV reactors, in: Struct. Mater. Gener. IV Nucl. React., Elsevier, 2017: pp. 191–252. doi:10.1016/B978-0-08-100906-2.00006-9.

[18] R.L. Klueh, Elevated temperature ferritic and martensitic steels and their application to future nuclear reactors, Int. Mater. Rev. 50 (2005) 287–310. doi:10.1179/174328005X41140.

[19] S. Suresh, Fatigue of Materials, Cambridge University Press, 1998.

[20] M. Walter, Private communication, 2017.

10.2 Annex B: Small punch and tensile test results on ODS-9Cr and ODS-14Cr

E. Altstadt and M. Houska
Helmholtz-Zentrum Dresden-Rossendorf

B1 Introduction

Within Task 4.1 of the FP7-MATISSE project, HZDR performed small punch tests on two ODS materials with 9 and 14 wt% Cr. In addition, mini tensile tests from room temperature up to 700 °C were performed on the 9Cr-ODS material.

B2 Experimental

B2.1 Material

The Fe-9Cr ODS bar is an extruded bar in the ferritic state. The chemical composition in (wt%) is: 9.1 Cr, 0.19 Y, 0.2 Ti, 0.29 Mn, 0.2 Ni, 0.23 Si, 1.05 W[2]. The tests were done on the as received condition and after a heat treatment at the HZDR lab. The heat treatment included a homogenisation at 1050 °C / 30 min with a subsequent quenching in oil. The cooling rate was sufficiently high (> 10 K/s) in order to obtain a martensitic structure. Finally, a tempering at 750 °C / 1 h was performed. In this report, the as received material is denoted as 9Cr-ODS-A and the heat treated material as 9Cr-ODS-B. The microstructures are shown in Figure 1. The average hardness is HV10 = 271 for 9Cr-ODS-A and HV10 = 302 for 9Cr-ODS-B.

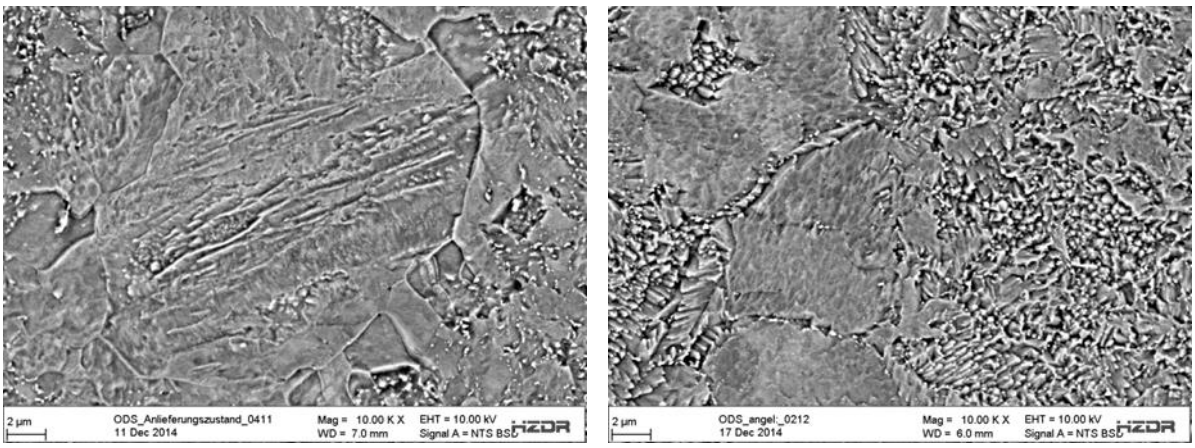

Figure 1: Microstructure of 9Cr-ODS-A (left) and 9Cr-ODS-B (right)

The 14Cr ODS bar was supplied by CEA within the GETMAT project (the code for this material was J27-M2). The consolidation of the pre-alloyed powder was carried out by hot extrusion at 1100 °C. Finally, the manufactured bars were annealed at 1050 °C for 1.5h. The average chemical composition obtained on the final material was (in wt%) 13.5 Cr, 0.22 Y, 0.9 W, 0.4 Ti, 0.27 Mn and 0.32 Si. The microstructure of the 14Cr ODS bar shows an elongated-grain structure parallel to the extrusion direction. In the longitudinal plane, the material exhibits a bimodal grain size distribution, in which the smallest grains have a distribution ranging from 0.1 to 3.0 microns, whereas the largest and more elongated grains have sizes between 3.0 and 9.0 µm. In the transverse plane a more uniform distribution of grain size is observed, with a mean length of 432 ± 55 nm [1]. The Vickers hardness is HV10 ≈ 380 [2]. In this report, the material is denoted as 14Cr-ODS.

[2] Personal communication Y. de Carlan - C. Heintze

B2.2 Small punch tests and tensile tests

The SP sample geometry is 10 x 10 x 0.5 mm³ for the 14Cr-ODS bar and 9 x 9 x 0.5 mm³ for the 9Cr-ODS bar. The areal dimension is not important as the samples are fully clamped during the test. The SPT specimens were cut from the bars by EDM with a thickness of 0.54 mm and ground to the final thickness of 0.5 ± 0.005 mm with grit 1200. The diameter of the receiving hole is 4.0 mm with an edge radius of 0.5 mm and the diameter of the hemispherical puncher is 2.5 mm. The cutting schemes are shown in Figure 2 and Figure 3. All samples are L-oriented, i.e. the normal of the disc coincides with the extrusion direction. This orientation represents the properties in the RC plane (R - radial, C – circumferential direction), cf. [3].

Small punch tests were performed in the temperature range from -193 °C up to +22 °C for both materials. The loading rate was 0.5 mm/min (puncher displacement).

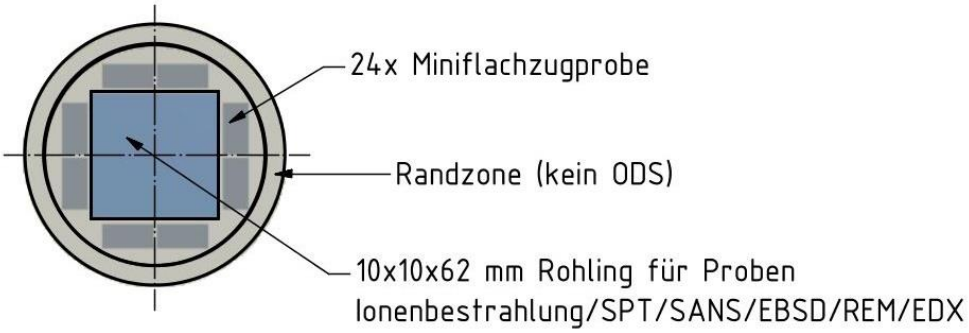

Figure 2: Cutting scheme for SP and tensile samples from the 9Cr-ODS bar

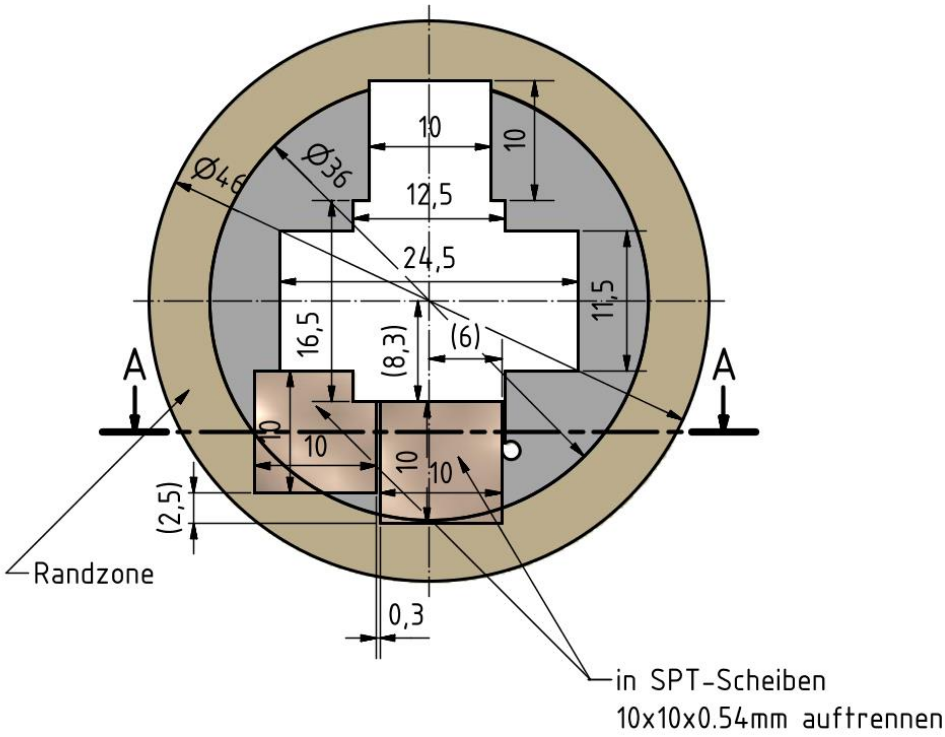

Figure 3: Cutting scheme for SP samples from the 14Cr-ODS bar

Tensile tests were performed for the as received condition and the heat treated condition of the 9Cr-ODS. The test temperatures are 22, 300, 400, 500, 600 and 700 °C. The strain rate was ~10^{-4}/s. At least 3 tests

per temperature and condition were performed. The geometry of the tensile specimens is shown in Figure 4. The specimens are L-oriented, i.e. along extrusion direction. The engineering stress-strain curves were corrected in such a way that the linear-elastic slope agrees with the expected elasticity modulus. The underlying equation is:

$$\bar{\varepsilon}_{corr} = \bar{\varepsilon}_{meas} - \left(\frac{1}{E_{meas}} - \frac{1}{E(T)} \right) \cdot \bar{\sigma}_{meas} \qquad \text{Eq 1}$$

where the overbar indicates nominal stress and strain. E_{meas} is the linear-elastic slope of the measured data (obtained by linear regression) and E(T) is the target elasticity module at the test temperature. The following E(T) values for the P91 steel (Table 1) were taken as basis [4,5].

Table 1: Elasticity module of P91

T (°C)	-180	-150	-100	-50	20	100	200	300	400	500	600	700
E (GPa)	221	220	218	216	210	203	194	186	178	165	151	127

The geometry of tensile specimens exhibits a proportional gauge length, i.e. the slimness ratio (gauge length over square root of cross section) is $L_0 / \sqrt{S_0} = 5.65$. Thus a conversion of the elongation according to EN ISO 2566-1 is not applicable.

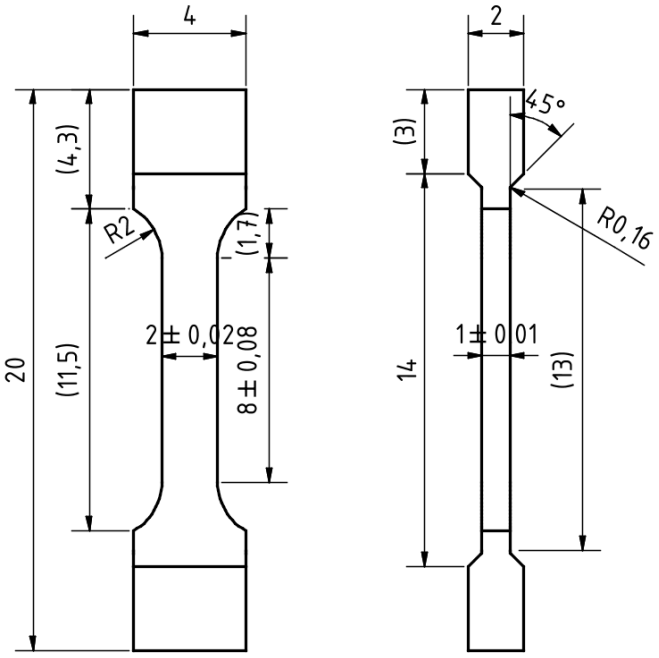

Figure 4: Geometry of the mini tensile specimens

The tensile properties of the 14Cr-ODS are reported in [1].

B3 Results

B3.1 SP test results

Averaged load-displacement curves for 9Cr-ODS are shown in Figure 5. The averaging procedure is explained in the appendix. Each averaged curve was obtained from three single tests. At room temperature (RT), the heat treatment causes a significant reduction of the displacement at maximum load u_m., while the maximum load F_m is only slightly affected. In contrast to this, a significant reduction of u_m and F_m is observed at 350 °C.

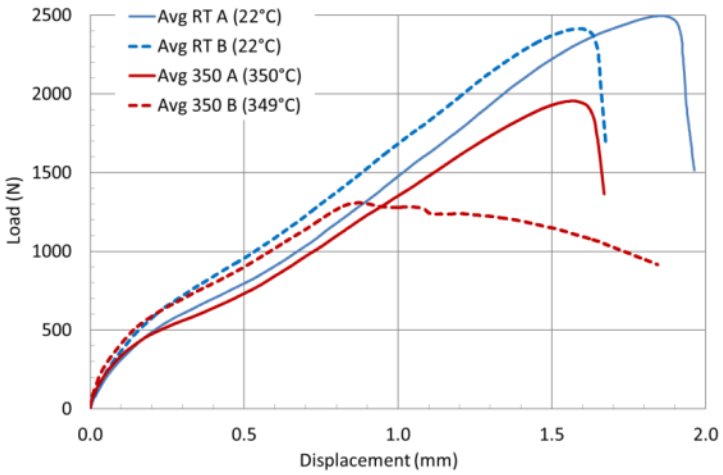

Figure 5: Averaged load-displacement curves for 9Cr-ODS for RT and 350 °C in the as received (A) and the heat treated (B) condition

The ductile-to-brittle transition temperature (DBTT) of the SP test, T_{SP}, is evaluated from the temperature dependence of the small punch energy. The energies were calculated from the load-displacement curves up to displacement at maximum load (u_m). A two curve fitting procedure was applied, one curve for the brittle (transition) range and one curve for the ductile range [6]. The results for all materials are shown in Figure 6 to Figure 8. The following SP DBTTs were obtained: T_{SP} = -138 °C for 9Cr-ODS-A, T_{SP} = -100 °C for 9Cr-ODS-B, and T_{SP} = -113 °C for 14Cr-ODS.

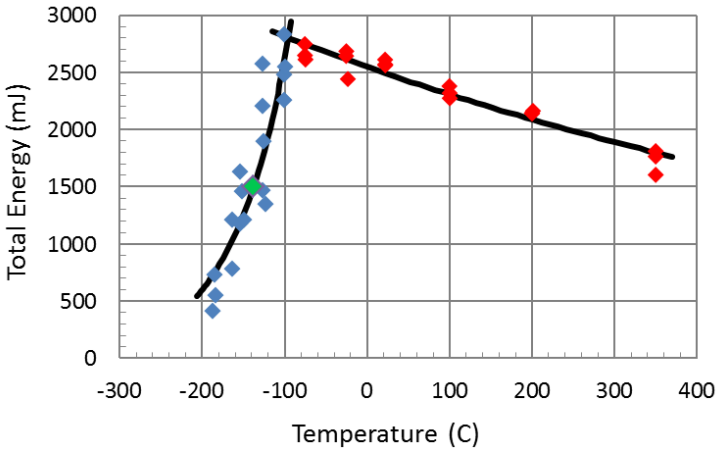

Figure 6: Determination of the ductile to brittle transition temperature T_{SP} for the as received condition of the 9Cr-ODS

T_{SP} = -138 °C

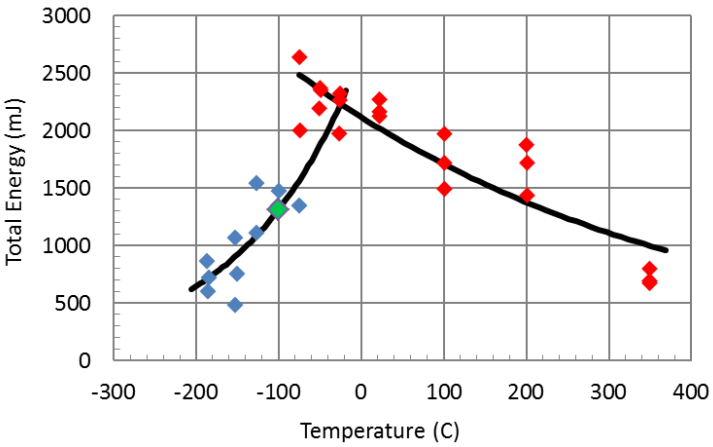

Figure 7: Determination of the ductile to brittle transition temperature TSP for the as heat treated condition of the 9Cr-ODS

T_{SP} = -100 °C

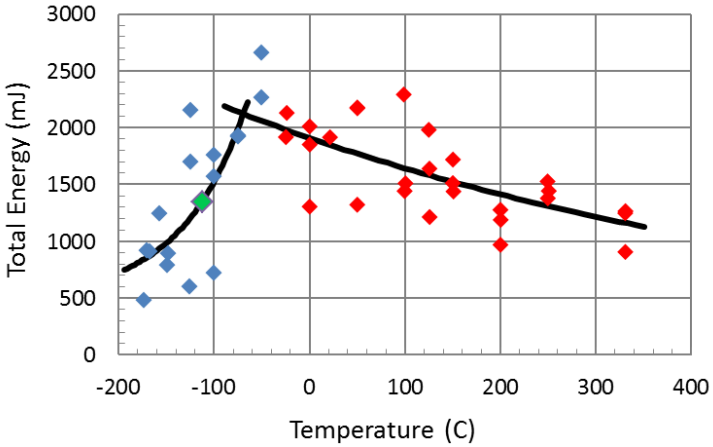

Figure 8: Determination of the ductile to brittle transition temperature TSP for the 14Cr-ODS

T_{SP} = -113 °C

The yield stresses are estimated by means of the empirical correlation $R_{p02} = \beta_{YS} \cdot F_e / h^2$ for each SP test. The transition load F_e is determined by a bilinear fit procedure [6]. We used u_B = 0.5 mm as upper fitting displacement. The factor β_{YS} = 0.49 was taken over from a study on T91 steel [6]; h is the initial specimen thickness. The results are shown in Figure 9 to Figure 11.

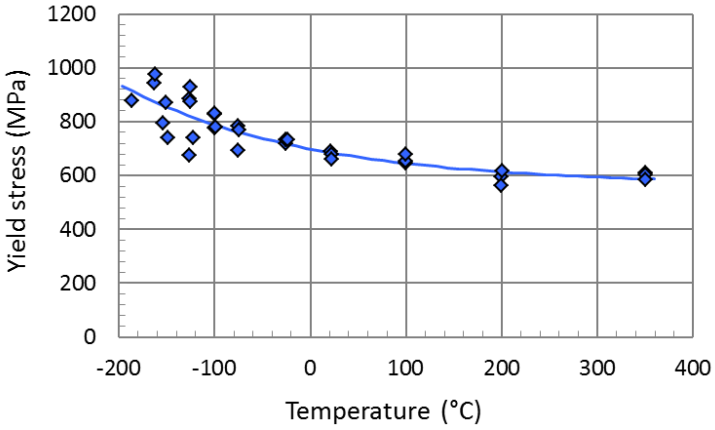

Figure 9: Yield stress vs. temperature obtained from SP tests on 9Cr-ODS, as received condition, with fitting curve:

R_{p02}(MPa) = 566+545·exp[-0.0051·T(K)]

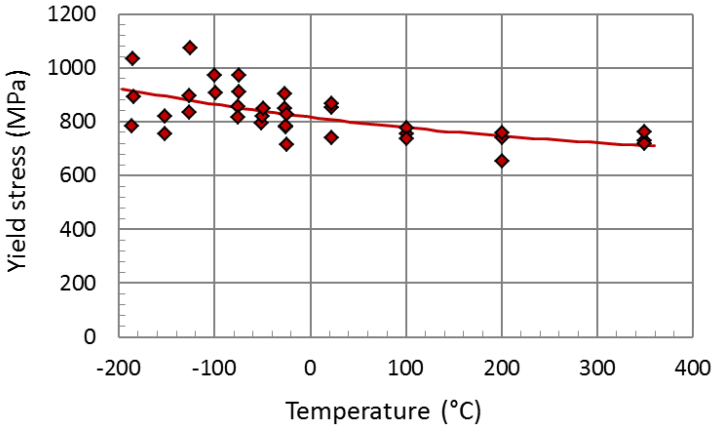

Figure 10: Yield stress vs. temperature obtained from SP tests on 9Cr-ODS, heat treated condition, with fitting curve:

R_{p02}(MPa) = 621+358·exp[-0.0022·T(K)]

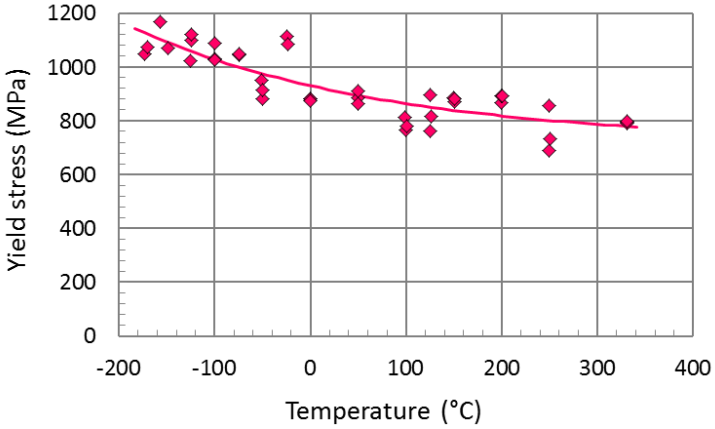

Figure 11: Yield stress vs. temperature obtained from SP tests on 14Cr-ODS with fitting curve:

R_{p02}(MPa) = 719+596·exp[-0.0038·T(K)]

B3.2 Tensile properties for 9Cr-ODS from tensile tests

The results of the tensile tests are summarized in Figure 12. The tensile properties are listed in Table 2. In the as received condition (9Cr-ODS-A), a Lüders strain is observed for temperatures up to 400 °C. This is not the case for the heat treated condition (9Cr-ODS-B). The total elongation exhibits a minimum at 400 °C in both conditions.

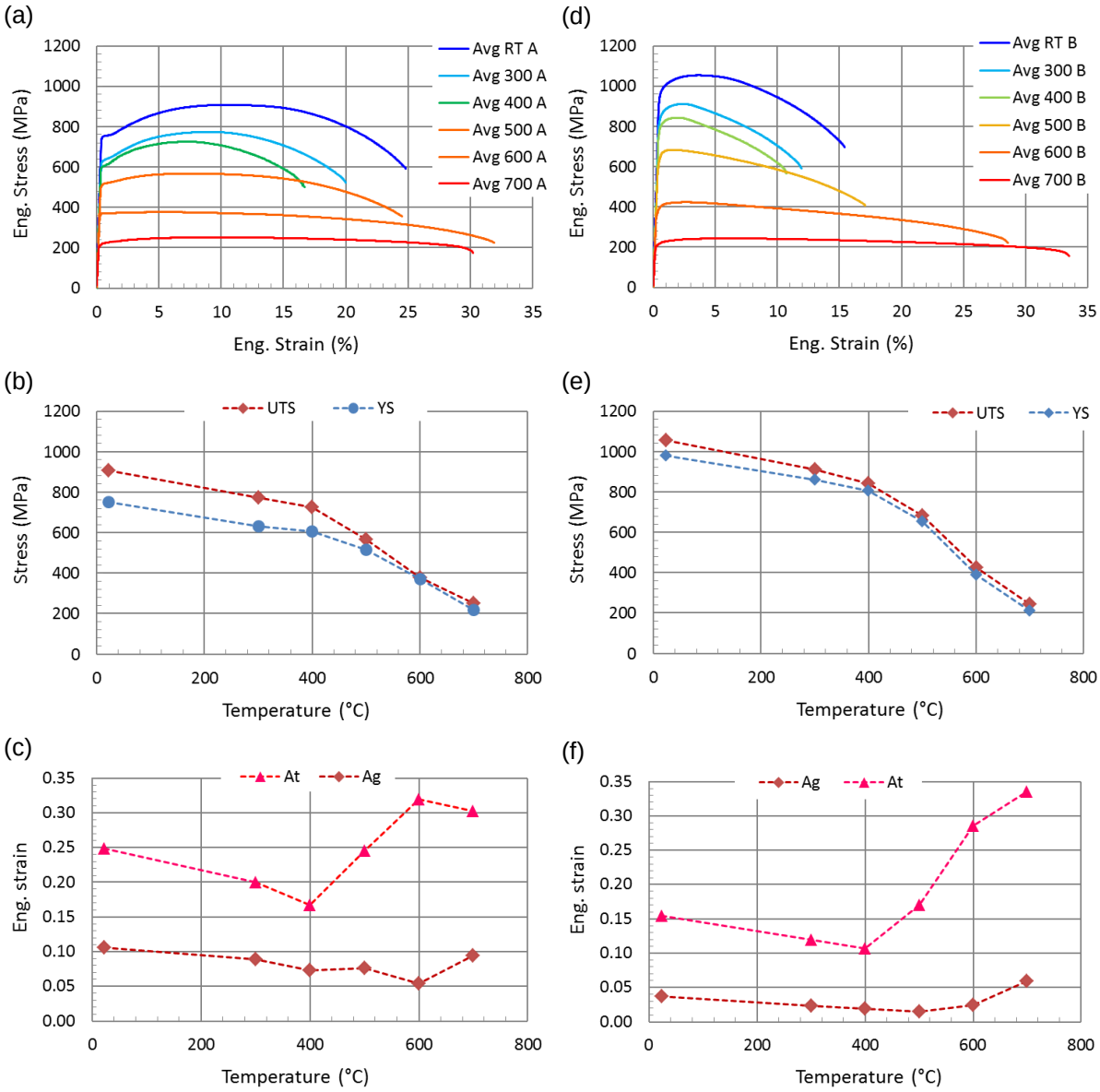

Figure 12: Tensile results for the 9Cr-ODS in the as received (a-c) and the heat treated condition (d-f); averaged stress-strain curves for different temperature (a, d); dependence of $R_{p0.2}$ and R_m on temperature (b, e); dependence of A_g and A_t on temperature (c, f)

Table 2: Tensile properties measured by mini tensile specimens

	9Cr-ODS as received				9Cr-ODS heat treated			
T (°C)	$R_{p0.2}$ (MPa)	R_m (MPa)	A_g (%)	A_t (%)	$R_{p0.2}$ (MPa)	R_m (MPa)	A_g (%)	A_t (%)
RT	752	908	10.6	24.8	978	1054	0.037	15.4
300	633	774	8.9	20.0	859	912	0.023	11.9
400	604	725	7.3	16.7	806	843	0.019	10.7
500	515	567	7.6	24.5	655	684	0.015	17.1
600	371	377	5.4	31.9	390	423	0.025	28.6
700	217	252	9.4	30.2	213	243	0.060	33.5

B4 Discussion

The comparison of the yield stresses of all materials obtained from the SP tests in the temperature range from -193 … +350 °C is shown in Figure 13. The tensile properties obtained from tensile tests in the temperature range from RT up to 700 °C are shown in Figure 14 to Figure 16. The results for 14Cr-ODS were taken from [1].

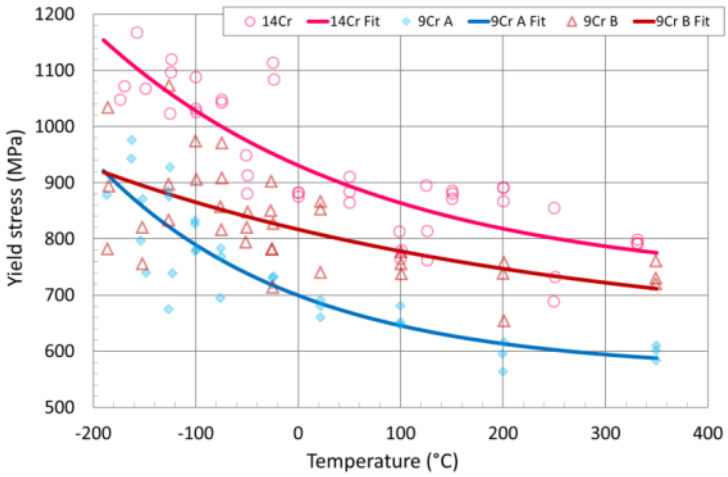

Figure 13: Comparison of yield stress dependence on temperature based on SP test results.

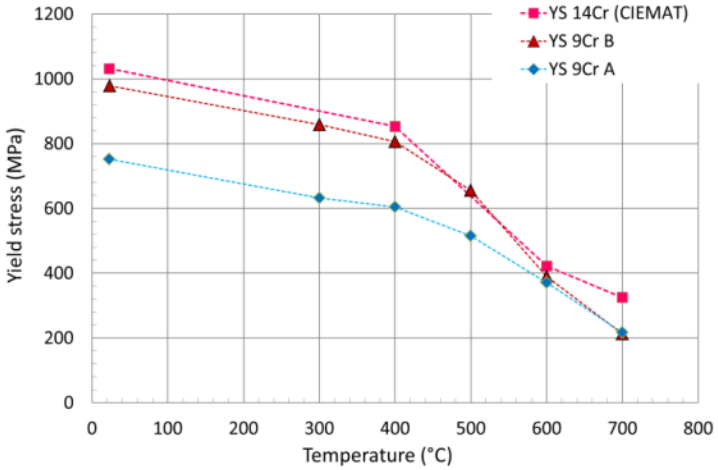

Figure 14: Comparison of yield stress dependence on temperature based on tensile test results.

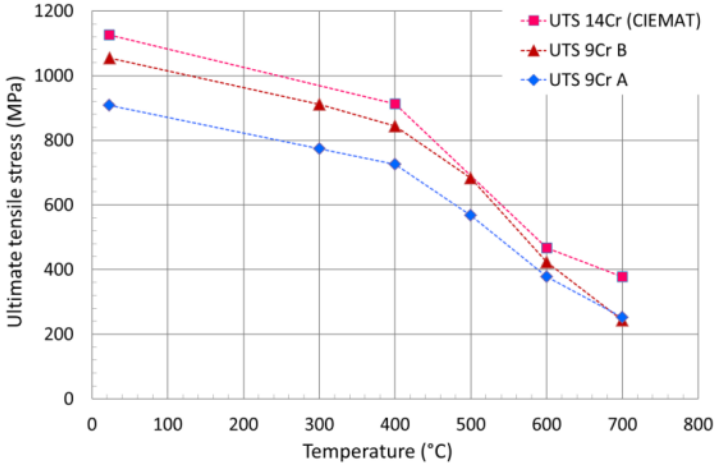

Figure 15: Comparison of UTS dependence on temperature based on tensile test results.

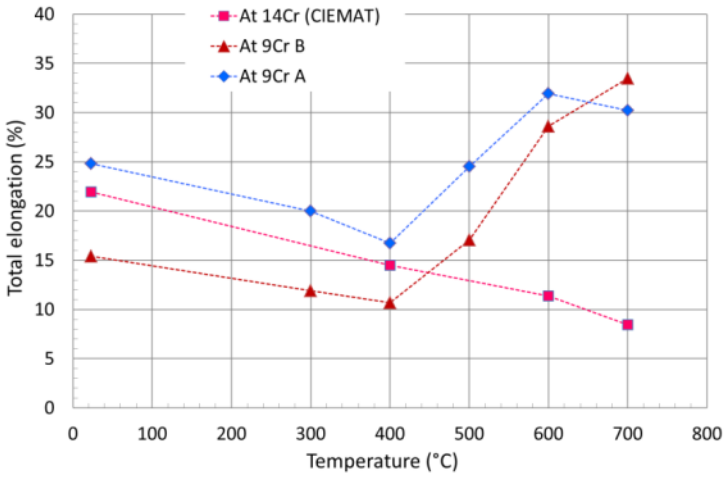

Figure 16: Comparison of total elongation dependence on temperature based on tensile test results.

The SP based yield stresses are reasonable estimations in the sense that the hardening of 9Cr-ODS due to the heat treatment is clearly visible and that the order of materials with respect to increasing YS (9Cr-ODS-A, 9Cr-ODS-B, 14Cr-ODS) is the same as in the tensile test based results. However, the absolute YS values from the SP tests are systematically lower compared to the tensile test values in the overlapping temperature range. Obviously the empirical correlation factor (β_{YS} = 0.49), obtained for T91 steel [6], is not the optimum for the ODS alloys in this work.

As for the ductility of the ODS alloys, a minimum of the total elongation was observed at 400 °C for 9Cr-ODS in both conditions while the a steady decrease up to 700 °C was observed for 14Cr-ODS [1], cf. Figure 16.

The DBTTs obtained from SP tests can be converted into Charpy transition temperatures [7]. The conversions factor for our test set-up (α = 0.42) was obtained based on results for a T91 steels [6]. The DBTTs are listed in Table 3. For the 9Cr-ODS, the heat treatment leads to a significant increase of the DBTT. The DBTT of the 14Cr-ODS is in between those of 9Cr-ODS-A and 9Cr-ODS-B. This coincides with the order of total elongation from the tensile test in the temperature range up to 400 °C (Figure 16), i.e. the higher the total elongation the lower the DBTT.

Table 3: Transition temperatures obtained from the SP test

	9Cr-ODS as received	9Cr-ODS heat treated	14Cr-ODS
T_{SP} (°C)	-138	-100	-113
T_{CVN} (°C) *	+50	+138	+109

* Recalculated from $T_{SP}[K]=0.42*T_{CVN}[K]$

For the 14Cr-ODS, KLST impact test results are available [2]: the DBTT is T_{KLST} = -20 °C for the orientation LR and T_{KLST} = +100 °C for orientation RL. This corresponds to Charpy DBTTs of T_{CVN} = +45 °C and T_{CVN} = +165 °C [8]. Thus, the SP based DBTT (L-oriented specimens) is slightly lower than the KLST based DBTT in the crack divider configuration (orientation RL) and significantly higher than the KLST based DBTT in the crack arrester configuration (orientation LR), cf. [3,9].

B5 Conclusions

For the 9Cr-ODS, the heat treatment leads to an increase of the DBTT and of the yield stress. The total elongation exhibits a minimum at 400 °C for 9Cr-ODS in both conditions while a steady decrease up to 700 °C was observed for 14Cr-ODS. Even though the 14Cr-ODS has a higher yield stress than the 9Cr-ODS-B, the DBTT of the 14Cr-ODS is slightly lower than the one of 9Cr-ODS-B.

B6 References

[1] M. Serrano, M. Hernández-Mayoral, A. García-Junceda, Microstructural anisotropy effect on the mechanical properties of a 14Cr ODS steel, J. Nucl. Mater. 428 (2012) 103–109. doi:10.1016/j.jnucmat.2011.08.016.

[2] Y. de Carlan, Basic characterisation of 14Cr1WYTi Ferritic ODS, Getmat Deliverable D1.2b, CEA, 2012.

[3] E. Altstadt, M. Serrano, M. Houska, A. García-Junceda, Effect of anisotropic microstructure of a 12Cr-ODS steel on the fracture behaviour in the small punch test, Mater. Sci. Eng. A. 654 (2016) 309–316. doi:10.1016/j.msea.2015.12.055.

[4] ThyssenKrupp, Werkstoffdatenblatt P91/T91 (1.4903), ThyssenKrupp Materials International GmbH, 2011.

[5] J. Warreing, A review of the mechanical and physical properties of modified 9CrMoNbV (Grade 91) steel, CEA/SRMA, 1994.

[6] E. Altstadt, H.E. Ge, V. Kuksenko, M. Serrano, M. Houska, M. Lasan, M. Bruchhausen, J.-M. Lapetite, Y. Dai, Critical evaluation of the small punch test as a screening procedure for mechanical properties, J. Nucl. Mater. 472 (2016) 186–195. doi:10.1016/j.jnucmat.2015.07.029.

[7] J. Kameda, A kinetic model for ductile-brittle fracture mode transition behavior, Acta Metall. 34 (1986) 2391–2398. doi:10.1016/0001-6160(86)90142-2.

[8] E.N. Klausnitzer, Micro-Specimens for Mechanical Testing, Materialprüfung. 33 (1991) 132–134.

[9] Y. Kimura, T. Inoue, F. Yin, K. Tsuzaki, Delamination Toughening of Ultrafine Grain Structure Steels Processed through Tempforming at Elevated Temperatures, ISIJ Int. 50 (2010) 152–161. doi:10.2355/isijinternational.50.152.